Measurement of asymmetries in associated DVCS using the HERMES Recoil detector

Messung von Asymmetrien in der assoziierten tief-virtuellen Compton-Streuung mit dem HERMES-Rückstoßdetektor

Master-Thesis

im Studiengang M.Sc. Physik

Erik Etzelmüller

II. Physikalisches Institut

Justus-Liebig-Universität Gießen

AG Düren

13. Mai 2013

Zusammenfassung

Die vorliegende Arbeit beinhaltet Messungen von *Beam-Spin-* und *Beam-Charge*-Asymmetrien in der assoziierten tief-virtuellen Compton-Streuung (ADVCS) $ep \to e\gamma\Delta^+$. Tief-virtuelle Compton Streuung erlaubt den theoretisch einfachsten Zugang zu Generalisierten Parton Verteilungen (GPDs). Experimentell wurden longitudinal polarisierte Elektronen und Positronen des HERA-Leptonenstrahls auf das unpolarisiertes Wasserstoff-Target des HERMES - Experiments geschossen. Der Endzustand ist dabei nicht vom assoziierten Bethe-Heitler-Prozess (ABH) unterscheidbar, weswegen die Asymmetrieamplituden auf einer Interferenz beider Prozesse beruhen. Darüber hinaus sorgen verwandte, nicht resonante Prozesse für einen erheblichen Untergrund. Die Amplituden wurden separat für beide Zerfallskanäle der Δ^+-Resonanz ($ep \to e\gamma p\pi^0$ und $ep \to e\gamma n\pi^+$) sowie deren Kombination gemessen.
Die Messung wurde erst durch die Installation eines Rückstoßdetektors möglich, der in der Lage war, geladene Teilchen mit niedrigen Impulsen unter großen Winkeln zu detektieren. Die im Rahmen dieser Analyse verwendete Spurrekonstruktion innerhalb des Rückstoßdetektors beruht dabei ausschließlich auf dem *Scintillating Fibre Tracker* (SFT) und beinhaltet keine Teilchenidentifikation. Die Selektion der ADVCS/BH-Ereignisse basiert dabei auf kinematischen Fits aller geladenen Teilchen des Endzustands. Neben der eigentlichen Extraktion der Asymmetrien wurde eine detaillierte Monte-Carlo Analyse sowie Studien zur Qualität der verwendeten Daten durchgeführt.
Die Messungen der ADVCS-*Beam-Charge*-Asymmetrien wurden hierbei erstmals mit HERMES -Daten durchgeführt. Vielversprechende Resultate wurden vor allem für die Kanäle $ep \to e\gamma\Delta^+$ (kombiniert) und $ep \to e\gamma n\pi^+$ erzielt. Der relative Untergrund konnte dabei auf 34 % reduziert werden. Im Fall des kombinierten Kanals weist $\cos(3\phi)$ eine positive Amplitude auf. Für $ep \to e\gamma n\pi^+$ sind alle Amplituden innerhalb ihrer statistischen Fehler mit 0 verträglich. Lediglich $\cos(\phi)$ weist eine leichte positive Abweichung auf.

Abstract

Beam spin and beam charge asymmetries in associated electroproduction of real photons $ep \to e\gamma\Delta^+$ are measured at HERMES using the longitudinally polarized HERA lepton beam and an unpolarized hydrogen target. The asymmetries arise from associated deeply virtual Compton scattering (ADVCS) and its interference with the associated Bethe-Heitler (ABH) process as well as their elastic counterparts where the struck proton remains in the ground state. These processes provide the theoretically cleanest access to Generalized Parton Distributions. The amplitudes are extracted separately for both decay channels of the Δ^+, $ep \to e\gamma p\pi^0$ and $ep \to e\gamma n\pi^+$ as well as for their combination. The track reconstruction of the recoiling particle is done using the scintillating fibre tracker of the HERMES Recoil detector only. The selection involves kinematic fitting of all charged final-state particles. A detailed Monte-Carlo study and additional data-quality checks are carried out in order to estimate the feasibility.

The measurement of beam charge asymmetries for associated DVCS/BH at HERMES is carried out for the first time. Solid results are obtained for the channels $ep \to e\gamma\Delta^+$ (combined) and $ep \to e\gamma n\pi^+$ with a background contamination of 34 %. For the latter one all but one amplitude are consistent with zero within their statistical uncertainties and a weak indication for a positive amplitude for $\cos(\phi)$ are observed.

Table of Contents

1. Motivation **1**

2. Generalized Parton Distributions (GPDs) **4**

2.1. Theory . . . 4

2.1.1. Introduction . . . 4

2.1.2. Properties of GPDs . . . 6

2.1.3. Expansion to the case of associated DVCS . . . 7

2.2. Experimental access to GPDs . . . 11

2.2.1. Deeply virtual Compton scattering (DVCS) . . . 11

2.2.2. Extraction of asymmetry amplitudes . . . 12

2.2.3. The extended maximum likelihood method . . . 15

2.3. Kinematic variables . . . 17

3. The HERMES experiment **19**

3.1. HERA at DESY . . . 19

3.2. The HERMES forward spectrometer . . . 20

3.3. The HERMES Recoil detector . . . 23

3.4. Track reconstruction with the HERMES Recoil detector . . . 25

4. Event selection **27**

4.1. Selection in the HERMES forward spectrometer . . . 27

4.1.1. General selection . . . 27

4.1.2. Selection of deep inelastic scattering (DIS) . . . 28

4.1.3. Selection of deeply virtual Compton scattering (DVCS) . . . 28

4.2. Selection with the HERMES Recoil detector . . . 29

4.2.1. Recoil cuts . . . 29

4.2.2. Kinematic fitting . . . 29

4.2.3. Exclusion of events in the second Recoil quadrant . . . 31

4.2.4. Track multiplicities for method 3 . . . 32

4.2.5. Final selection . . . 33

4.2.5.1. Elastic sample ($ep \to e\gamma p$) . . . 33

4.2.5.2. Associated sample ($ep \to e\gamma\Delta^+$) . . . 33

4.2.5.3. Associated sample ($ep \to e\gamma p\pi^0$) . . . 34

4.2.5.4. Associated sample ($ep \to e\gamma n\pi^+$) . . . 34

4.2.6. Comment on particle identification with the Recoil detector . . . 34

5. Data quality studies **36**

5.1. Previous results . . . 36

5.2. Additional studies 37

6. Monte-Carlo studies **40**

6.1. Summary of previous studies to select elastic events 40

6.2. Optimization of kinematic fitting 42

6.3. Study of the selection of resonant events 45

6.3.1. Associated events $ep \to e\gamma\Delta^+$ (combined) 45

6.3.2. Associated events $ep \to e\gamma p\pi^0$ 47

6.3.3. Associated events $ep \to e\gamma n\pi^+$ 51

7. Extraction of BSA amplitudes **56**

7.1. Elastic channel 57

7.2. Associated channel $ep \to e\gamma\Delta^+$ (combined) 57

7.3. Associated channel $e^+p \to e^+\gamma p\pi^0$ 57

7.4. Associated channel $e^+p \to e^+\gamma n\pi^+$ 58

8. Extraction of BCA amplitudes **61**

8.1. Associated channel $ep \to e\gamma\Delta^+$ (combined) 61

8.2. Associated channel $ep \to e\gamma p\pi^0$ 62

8.3. Associated channel $ep \to e\gamma n\pi^+$ 62

9. Summary and conclusion **65**

Bibliography **67**

List of figures **73**

List of tables **74**

A. Appendix **75**

1. Motivation

Starting with the discovery of the atomic nucleus by Geiger and Marsden under direction of Rutherford in 1909, for more than a hundred years scattering experiments have enlightened our understanding of matter. In order to get a deeper insight many experiments and theories have been developed over the years. Pioneering experiments, particularly at SLAC during the 70's, CERN during the 80's and DESY until 2007 have opened access to the substructure of nucleons via deep inelastic scattering.
Related to the form factors in case of nuclei and nucleons the dynamics of deep inelastic scattering are described in terms of the structure functions W_1 and W_2. These were found to be mostly independent of the momentum transfer Q^2, which proved the existence of subparticles called partons. Charged partons were later identified as quarks. The underlying quark model allows the formulation of predictive sum rules, which can be verified by experimental measurements. Besides the valence quarks which give rise to the quantum numbers of the nucleon, virtual quark-antiquark pairs exist.

An important result was the measurement of the momentum of a nucleon carried by the quarks which was found to be only about 50% [1]. The missing momentum is carried by the gauge bosons of the strong force, called gluons which do not carry electromagnetic but color charge and where first observed in 3-jet-events. Gluons are explained in the framework of quantum chromo dynamics (QCD) which describes unique features such as confinement and asymptotic freedom.
Nowadays the momentum distributions of quarks and gluons is known with relatively high precision.
By contrast the spin structure of the nucleon still remains a quest. In the framework of Dirac theory quarks are spin-1/2 particles. This was experimentally verified by measurements of the Callan-Gross relation which is based on the before mentioned structure functions [2]. With two quarks being parallel and one being anti-parallel orientated this naively sums up to the proton spin of 1/2.

The first one who discussed the spin structure in the context of deep inelastic scattering was James Bjorken. In 1966 he introduced a fundamentally important sum rule based on current algebra, scaling behavior of the structure functions in deep inelastic scattering and isospin symmetry in the nucleon. It comprised a fundamental relationship between the spin-dependent structure functions (g_1^p, g_1^n) and the ratio of nucleon vector and axial vector couplings ($|g_V/g_A|$) [3]:

$$I_p - I_n = \int_0^1 (g_1^p - g_1^n)\mathrm{d}x = \frac{1}{6}\left|\frac{g_A}{g_V}\right|. \tag{1.1}$$

Another closely related sum rule was introduced by Ellis and Jaffe in 1973 [4]:

$$I_p = \int_0^1 g_1^p(x)\mathrm{d}x = \frac{1}{12}\left|\frac{g_A}{g_V}\right|[1 + 5/3(3F - D)/(F + D)], \tag{1.2}$$

$$I_n = \int_0^1 g_1^n(x)\mathrm{d}x = \frac{1}{12}\left|\frac{g_A}{g_V}\right|[-1 + 5/3(3F - D)/(F + D)]. \tag{1.3}$$

In comparison to the Bjorken sum rule, the Ellis-Jaffe sum rule is less fundamental since it uses SU(3) symmetry arguments appearing through the parameters F and D.
At first measurements were consistent with the predictions made by Ellis and Jaffe. However in 1988 the European Muon Collaboration (EMC) published results for the spin-dependent structure function of the proton which in combination with the earlier measurements at SLAC resulted in a value of I_p being about three times lower than expected. As a result the fractional contribution of the total quark spin to the proton was only $\Delta q = 0.19 \pm 0.17$ with a large opposite strange sea quark contribution of $\Delta s = -0.13 \pm 0.06$ [5].
These results marked the beginning of the "spin crisis" and stimulated further experimental work. Just one year after the discovery by the EMC, the HERMES experiment was born in order to solve the so called "spin puzzle". HERMES was able to confirm the invalidity of Ellis-Jaffe sum rule but it measurements were in agreement with the Bjorken sum rule. The latter one being of unique importance as a test of QCD.
In recent years a major effort was put into the detailed investigation of the nucleon's spin S_z and its composition:

$$\frac{1}{2} = S_z = \frac{1}{2}\cdot\Delta\Sigma + \Delta G + L_z^q + L_z^G. \tag{1.4}$$

Here $\Delta\Sigma$ is the spin contribution of valence and sea quarks, ΔG the spin contribution of the gluons and L_z^q and L_z^G the contributions of quark and gluon orbital momenta (see, e.g., [5],[6],[7] and references therein).

ΔG can be accessed via next-to-leading order perturbative QCD (pQCD) fits to g_1. However results have very large experimental and theoretical uncertainties and yield to a rather small contribution [8],[9],[10].
The quark orbital momentum L_z^q itself has been difficult to measure [11]. However a promising theoretical framework for this task is provided by generalized particle distributions (GPDs), which combine the above mentioned form factors and the parton distributions. According to a finding of Ji [12], GPDs allow access to the total angular momentum of the quarks, which through the relation

$$J^q = \frac{1}{2}\cdot\Delta\Sigma + L_z^q \tag{1.5}$$

also determines the orbital quark momentum.

The thesis is organized as follows. Chapter 2 gives a brief introduction to the formalism of GPDs and their extension to the case of the first nucleon excitation. The theoretically cleanest access to GPDs is deeply virtual Compton scattering, whichis introduced together with the experimental measurement techniques. The HERMES experiment itself is described in chapter 3 with a focus on the Recoil detector in section 3.3. The selection of the different event samples which are investigated is explained in chapter 4. Chapter 5 contains some comments on the data quality of the selected samples and additional information on the data taking period for the electron beam. A detailed Monte-Carlo study concerning the feasibility of the analysis and to estimate background contributions has been carried out and is described in chapter 6. The results of beam spin and beam charge asymmetry extraction are discussed in chapter 7 and 8 respectively. A summary is given in chapter 9 , followed by the bibliography and an appendix containing additional plots and tables.

2. Generalized Parton Distributions (GPDs)

2.1. Theory

2.1.1. Introduction

In quantum mechanics the simultaneous determination of position and momentum of a particle is not possible. Nevertheless the first quantum mechanical phase-space distribution was introduced by Eugene Paul Wigner in 1932 [13]:

$$W(x,p) = \int \mathrm{d}\eta\, e^{ip\eta}\psi^*(x-\eta/2)\psi(x+\eta/2). \tag{2.1}$$

Integration over x results in the positive-definite momentum density $|\psi(p)|^2$ and integrating over p results in the positive-definite coordinate space density $|\psi(x)|^2$. It is important to notice that for arbitrary values of p and x the Wigner distribution is not positive-definite and has no interpretation of a probability. In order to describe relativistic quarks and gluons in the nucleon the phase-space distribution can be generalized by the introduction of a Wigner Operator:

$$\hat{\mathcal{W}}_\Gamma(\vec{r},k) = \int \mathrm{d}^4\eta\, e^{ik\cdot\eta}\bar{\Psi}(\vec{r}-\eta/2)\Gamma\Psi(\vec{r}+\eta/2). \tag{2.2}$$

Here $\vec{r}$ is the quark phase-space position and k the phase-space four-momentum conjugated to the space-time separation η. Γ is a matrix of Dirac type which describes the distribution of quarks as relativistic spin-1/2 particles.

For a non-relativistic system the phase-space distribution can be defined by taking the expectation value of the Wigner operator in the center-of-mass state. In case of the proton this cannot be done and a rest-frame matrix element needs to be constructed, followed by averaging over all possible three-momentum transfers. The resulting quantum phase-space quark distribution depends on seven independent variables and its measurement is beyond the scope of current methods. Nevertheless a promising tool to deal with highly relativistic particles in the strong coupling regime has emerged with the light-cone quantization [14]. Experimental probes have shown that the only way of making the quark field Ψ gauge-invariant is by adding a gauge link to the space-time infinity along the light-cone vector $n^\mu = (1,0,0,-1)$. According to the Kogut-Soper convention "time-" and "space-like" coordinates in the light-cone quantization are parameterized by [15]:

$$\begin{pmatrix} x^+ \\ x^- \end{pmatrix} = \frac{1}{\sqrt{2}} \begin{pmatrix} 1 & 1 \\ 1 & -1 \end{pmatrix} \begin{pmatrix} x^0 \\ x^3 \end{pmatrix}. \tag{2.3}$$

By integrating out the light-cone energy $k^- = (k^0 - k^3)/\sqrt{2}$ one gets a six-dimensional reduced Wigner distribution:

$$W_\Gamma(\vec{r},\vec{k}) = \frac{1}{2}\int \frac{\mathrm{d}k^-\mathrm{d}^3\vec{q}}{(2\pi)^5}\langle \vec{q}/2|\hat{\mathcal{W}}_\Gamma(\vec{r},k)|-\vec{q}/2\rangle = \int \frac{\mathrm{d}k^-}{(2\pi)^2} W_\Gamma(\vec{r},k). \tag{2.4}$$

Integration over $\vec{r}$ leads to Transverse-Momentum-Dependent parton distributions (TMDs). They are a generalization of Feynman parton distributions [16] with additional information about the transverse momentum of partons. Alternatively $W_\Gamma(\vec{r},\vec{k})$ can be further reduced by integrating over the quark's transverse momentum $\vec{k}_\perp$ which leads to

$$\begin{aligned} \tilde{f}_\Gamma(\vec{r},\vec{k}^+) = \int \frac{\mathrm{d}^2\vec{k}_\perp}{(2\pi)^2} W_\Gamma(\vec{r},\vec{k}) = \frac{1}{2}\int \frac{\mathrm{d}^3\vec{q}}{(2\pi)^3} e^{i\vec{q}\cdot\vec{r}} \int \frac{\mathrm{d}\vec{\eta}_\perp^-}{2\pi} e^{i\eta^- k^+} \\ \times \langle \vec{q}/2|\overline{\Psi}(-\eta^-/2)\Gamma\Psi(\eta^-/2)|-\vec{q}/2\rangle. \end{aligned} \tag{2.5}$$

Hereby the matrix element $\Gamma \in \{\mathbb{1}, \gamma^\mu, \gamma^\mu\gamma_5, i\gamma_5, i\sigma^{\mu\nu}\gamma_5\}$ separates the various GPDs. By replacing $k^+ = xp^+$ and $\eta^- = \lambda/p^+$ with $p^+ = E_q/\sqrt{2}$ and E_q being the proton energy $\sqrt{M^2+\vec{q}/4}$ equation 2.5 can be rewritten as:

$$f_\Gamma(\vec{r},x) = \int \frac{\mathrm{d}^3\vec{q}}{(2\pi)^3} e^{-i\vec{q}\cdot\vec{r}} F_\Gamma(x,\xi,\Delta^2), \tag{2.6}$$

with $\xi = q_z/(2E_q)$, $\Delta = p' - p$ and

$$F_\Gamma(x,\xi,\Delta^2) = \frac{1}{2p^+}\int \frac{\mathrm{d}\lambda}{2\pi} e^{-i\lambda x}\langle \vec{q}/2|\overline{\Psi}(-\lambda n/2)\Gamma\Psi(\lambda n/2)|-\vec{q}/2\rangle. \tag{2.7}$$

For different choices of Γ leading-twist GPDs for each quark flavor are generated.
Taking $\Gamma = \gamma^+$ one gets

$$\begin{aligned} F_{\gamma^+}(x,\xi,\Delta^2) &= \frac{1}{2p^+}\int \frac{\mathrm{d}\lambda}{2\pi} e^{i\lambda x}\langle \vec{q}/2|\overline{\Psi}(-\lambda n/2)\gamma^+\Psi(\lambda n/2)|-\vec{q}/2\rangle \\ &= \frac{1}{2p^+}\overline{U}(\vec{q}/2)\left[H(x,\xi,\Delta^2)\gamma^+ + E(x,\xi,\Delta^2)\frac{i\sigma^{+i}q_i}{2M}\right]U(-\vec{q}/2), \end{aligned} \tag{2.8}$$

where $H(x,\xi,\Delta^2)$ and $E(x,\xi,\Delta^2)$ are two GPDs where the quark helicities are summed over. Another set of GPDs, $\tilde{H}(x,\xi,\Delta^2)$ and $\tilde{E}(x,\xi,\Delta^2)$, can be defined by choosing $\Gamma = \gamma^+\gamma_5$

$$\begin{aligned} F_{\gamma^+\gamma^5}(x,\xi,\Delta^2) &= \frac{1}{2p^+}\int \frac{\mathrm{d}\lambda}{2\pi} e^{i\lambda x}\langle \vec{q}/2|\overline{\Psi}(-\lambda n/2)\gamma^+\gamma_5\Psi(\lambda n/2)|-\vec{q}/2\rangle \\ &= \frac{1}{2p^+}\overline{U}(\vec{q}/2)\left[\tilde{H}(x,\xi,\Delta^2)\gamma^+ + \tilde{E}(x,\xi,\Delta^2)\frac{i\sigma^{+i}q_i}{2M}\right]U(-\vec{q}/2), \end{aligned} \tag{2.9}$$

These are responsible for the differences between right- and left-handed quarks.
Four more GPDs can be defined by setting $\Gamma = \sigma^{+\perp}\gamma_5$ with $\sigma^{+\perp} = \frac{1}{4}(\gamma^+\gamma^\perp - \gamma^\perp\gamma^+)$, which will not be discussed in this context.
The quantum phase-space distribution $f_\Gamma(\vec{r},x)$ allows the construction of three-dimensional images of quarks for selected Feynman momenta x in the rest frame of the proton [17].

2.1.2. Properties of GPDs

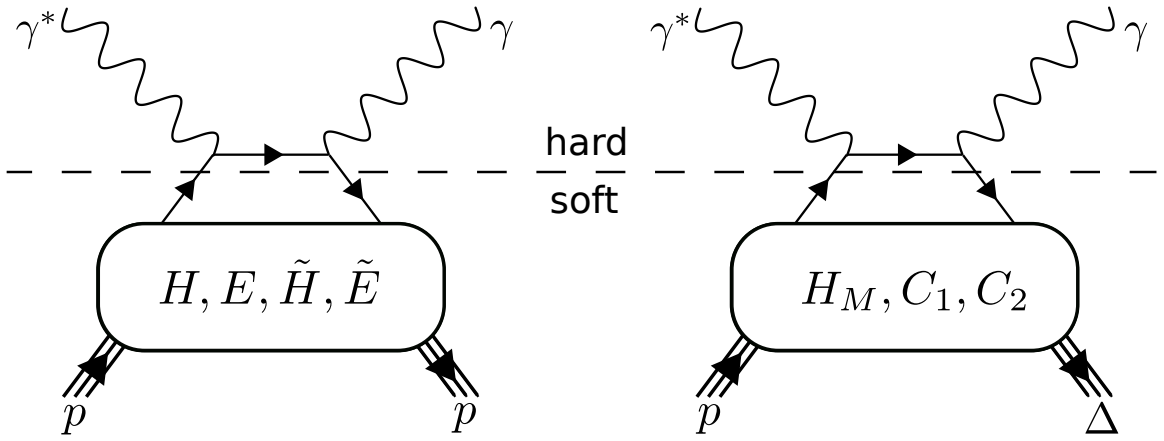

Figure 2.1.: Handbag diagrams with the corresponding GPDs for the elastic (left) and associated process (right). In the Bjorken limit the factorization theorem separates the hard scattering part (top) from the soft one (bottom) which is indicated by the dashed line.

The four quark GPDs appearing in equations 2.8 and 2.9 contribute to the simplest hard exclusive process: deeply virtual Compton scattering (DVCS). In contrast to ordinary parton distributions which represent the probability of finding a parton with a longitudinal momentum fraction x in the fast moving hadron and therefore integrating over all possible partonic configurations, GPDs represent the interference of two different wave functions. These wave functions describe a parton having a momentum fraction of $x + \xi$ and $x - \xi$, with ξ being the skewedness parameter. They additionally depend on a third independent variable $\Delta^2 = (p' - p)^2$, the momentum transfer between the initial (p) and final (p') nucleon state, which is equal to the Mandelstam variable t.
Generalized parton distribution fulfill both the ordinary parton distributions as well as the nucleon form factors. In the limit of $\Delta^2 \to 0$ and $\xi \to 0$ one gets

$$H^q(x,0,0) = q(x), \tag{2.10}$$

$$\tilde{H}^q(x,0,0) = \Delta q(x), \tag{2.11}$$

with $q(x)$ and $\Delta q(x)$ being the ordinary quark number density and quark helicity distributions respectively. Additionally the GPDs' first moments must satisfy the following relations:

$$\int_{-1}^{1} \mathrm{d}x\, H^q(x,\xi,\Delta^2) = F_1(\Delta^2), \tag{2.12}$$

$$\int_{-1}^{1} \mathrm{d}x\, E^q(x,\xi,\Delta^2) = F_2(\Delta^2), \tag{2.13}$$

$$\int_{-1}^{1} \mathrm{d}x\, \tilde{H}^q(x,\xi,\Delta^2) = g_A(\Delta^2), \tag{2.14}$$

$$\int_{-1}^{1} \mathrm{d}x\, \tilde{E}^q(x,\xi,\Delta^2) = h_A(\Delta^2). \tag{2.15}$$

Hereby $F_1(\Delta^2)$ and $F_2(\Delta^2)$ are the Dirac and Pauli form factors and $g_A(\Delta^2)$ and $h_A(\Delta^2)$ are the axial-vector and pseudo-scalar form factors. Negative values of x correspond to anti-quark distributions according to:

$$q(-x) = -\overline{q}(x), \tag{2.16}$$

$$\Delta q(-x) = \Delta\overline{q}(x). \tag{2.17}$$

If $|x| > \xi$ then GPDs are a generalization of the ordinary parton distributions whereas if $|x| > \xi$ they behave like meson distribution amplitudes.
Our interest for GPDs arises from Ji's finding that the second moments of the unpolarized GPDs at $\Delta^2 = 0$ give direct access to the quark's total angular momentum [12]:

$$J_q = \frac{1}{2}\int_{-1}^{+1} \mathrm{d}x \, \left[H^q(x,\xi,\Delta^2=0) + E^q(x,\xi,\Delta^2=0)\right]. \tag{2.18}$$

With the quark spin contribution $\Delta\Sigma/2$ and the quarks orbital angular momentum contribution L_q, J_q can be written as

$$J_q = \frac{1}{2}\Delta\Sigma + L_q \tag{2.19}$$

and therefore would allow a model-independent way to determine the contribution of the quark's angular momentum to the nucleon spin.
In order to parameterize GPDs different calculations exist. The bag model [18] and the chiral quark soliton model [19] differ from each other by the way the skewedness parameter ξ is treated. The former one has a weak dependence on ξ whereas the latter one shows a strong dependence on it. Because of the high photon virtuality in DVCS it is possible to exploit the factorization theorem and separate the hard part which can be computed in perturbation theory from the soft part depending on the long distance structure of the hadron. A common approach is to consider only the leading term of the hard part and to use a physically motivated guess which satisfies the general constraints known from theory such as equations 2.10 and 2.12. An alternative and very popular model to introduce a dependence on ξ is the double distributions formalism (DD), which uses the ordinary quark distribution $q(x)$ and a so-called profile function [20],[21]. In a simple approach the GPDs can be assumed to be independent of ξ [22],[23],[24].

2.1.3. Expansion to the case of associated DVCS

For more than a decade the description of resonant processes such as associated DVCS (abbreviated ADVCS or ΔVCS) has attracted theorists' attention. This was mainly motivated due to their background contribution to the measurements of "elastic" DVCS, where the proton remains in the ground state. Nevertheless this field hasn't had much progress since a direct measurement and the theoretical description of associated processes are very challenging. This section tries to summarize the main aspects and steps of Ref. [25] by Guichon,

Mossé and Vanderhaeghen, which comprises a very good coverage of the topic.
In order to estimate the cross section for the resonant reaction

$$\gamma^* + p \to \gamma + N + \pi, \tag{2.20}$$

pions are treated in the soft pion limit where the pion momentum k_π is taken as 0. In a relative sense this allows a model independent evaluation using the same GPDs as in the elastic case. However this approach is only valid in a region up to an excitation energy of 300 MeV where the first Δ resonance can be found. To increase the range of validity a model dependent estimate of the associated DVCS

$$\gamma^* + p \to \gamma + \Delta \tag{2.21}$$

was proposed. In this connection $N \to \Delta$ transition GPDs are introduced, which are in principle different from the nucleon ones. At first the corresponding matrix element is calculated on-shell and later it is modified due to the $\Delta \to N\pi$ strong decay. Three vector and four axial vector GPDs are introduced (the fourth vector GPD has a vanishing first moment and is therefore neglected). The vector GPDs are defined as [23]

$$\begin{aligned}
&\int \frac{\mathrm{d}\lambda}{2\pi} e^{i\lambda x} \langle \Delta(p') | \overline{\Psi}(-\lambda n/2) \not{n} \tau_3 \Psi(\lambda n/2) | - N(p) \rangle \\
&= \sqrt{\frac{2}{3}} \overline{\Psi}^\beta(p') \Big[H_M(x,\xi,\Delta^2) \mathcal{K}^M_{\beta\mu} n^\mu + H_E(x,\xi,\Delta^2) \mathcal{K}^E_{\beta\mu} n^\mu \\
&\qquad + H_C(x,\xi,\Delta^2) \mathcal{K}^C_{\beta\mu} n^\mu \Big] N(p),
\end{aligned} \tag{2.22}$$

where $\Psi^\beta(p')$ is the Rarita-Schwinger spinor for the Δ field, $N(p)$ the Dirac spinor for the nucleon and τ_3 the isospin $1/2 \to 2/3$ transition operator. The magnetic dipole- ($\mathcal{K}^M_{\beta\mu}$), the electric quadrupol- ($\mathcal{K}^E_{\beta\mu}$) and the Coulomb quadrupole covariants ($\mathcal{K}^C_{\beta\mu}$) are defined as [26]

$$\mathcal{K}^M_{\beta\mu} = -i \frac{3(m_\Delta + m)}{2m[(m_\Delta + m)^2 - \Delta^2]} \varepsilon_{\beta\mu\lambda\sigma} P^\lambda \Delta^\sigma, \tag{2.23}$$

$$\mathcal{K}^E_{\beta\mu} = -\mathcal{K}^M_{\beta\mu} - \frac{6(m_\Delta + m)}{mZ(\Delta^2)} \varepsilon_{\beta\mu\lambda\sigma} P^\lambda \Delta^\rho \varepsilon^\sigma_{\mu\kappa\delta} P^\kappa \Delta^\delta \gamma^5, \tag{2.24}$$

$$\mathcal{K}^C_{\beta\mu} = -i \frac{3(m_\Delta + m)}{3m[mZ(\Delta^2)]} \varepsilon_{\beta\mu\lambda\sigma} \Delta_\beta (\Delta P_\mu - \Delta \cdot P \Delta_\mu) \gamma^5, \tag{2.25}$$

where

$$Z(\Delta^2) = \left[(m_\Delta + M)^2 - \Delta^2\right] \left[(m_\Delta - M)^2 - \Delta^2\right]. \tag{2.26}$$

and $P = (p_\Delta + p)/2$, $p_\Delta^2 = m_\Delta^2$ with $m_\Delta = 1232$ MeV.
The GPDs defined in 2.22 H_M, H_E and H_C are linked with the three $N \to \Delta$ vector current transition form factors G^*_M, G^*_E and G^*_C through the sum rule

$$\int_{-1}^{1} = \mathrm{d}x \; H_{M,E,C}(x,\xi,\Delta^2) = 2G^*_{M,E,C}(\Delta^2). \tag{2.27}$$

Analogously to equation 2.22 four quark helicity dependent axial vector GPDs are defined [23]

$$\begin{aligned}\int \frac{d\lambda}{2\pi} e^{i\lambda x} \langle \Delta(p')|\overline{\Psi}(-\lambda n/2)\not{n}\gamma^5\tau_3\Psi(\lambda n/2)| - N(p)\rangle \\ = \overline{\Psi}^{\beta}(p')\left[C_1(x,\xi,\Delta^2)n_\beta, C_2(x,\xi,\Delta^2)\frac{\Delta_\beta(n\cdot\Delta)}{m_N^2} + C_3(x,\xi,\Delta^2)\frac{1}{m_N}\{n_\beta \not{\Delta} - \Delta_\beta \not{n}\}\right. \\ \left. + C_4(x,\xi,\Delta^2)\frac{1}{m_N^2}\{P\cdot\Delta n_\beta - 2\Delta_\beta\}\right] N(p).\end{aligned} \tag{2.28}$$

The GPDs C_1, C_2, C_3 and C_4 are linked to the four $N \to \Delta$ axial vector current transition form factors $C_5^A(\Delta^2)$, $C_6^A(\Delta^2)$, $C_3^A(\Delta^2)$ and $C_4^A(\Delta^2)$ through the sum rules [27]

$$\int_{-1}^{1} dx\, C_1(x,\xi,\Delta^2) = 2C_5^A(\Delta^2), \tag{2.29}$$

$$\int_{-1}^{1} dx\, C_2(x,\xi,\Delta^2) = 2C_6^A(\Delta^2), \tag{2.30}$$

$$\int_{-1}^{1} dx\, C_3(x,\xi,\Delta^2) = 2C_3^A(\Delta^2), \tag{2.31}$$

$$\int_{-1}^{1} dx\, C_4(x,\xi,\Delta^2) = 2C_4^A(\Delta^2). \tag{2.32}$$

$N \to \Delta$ vector transitions at small and intermediate momentum transfer are largely dominated by the $N \to \Delta$ magnetic dipole excitation $G_M^*(\Delta^2)$. Its value for vanishing Δ^2 ($G_M^*(0) = 3.02$) has been extracted from pion photoproduction experiments, while its Δ^2 dependence is a result of a phenomenological parametrization from a fit to pion electroproduction data [28]. In contrast electric and Coulomb quadrupole $N \to \Delta$ transitions are small and thus the GPDs H_E and H_C will be neglected.

For $N \to \Delta$ the partially conserved axial current formulation [29] leads to a dominance of the form factors C_5^A and C_6^A at low momentum transfer by what GPDs C_3 and C_4 will be neglected as well.

In the large N_C limit the remaining $N \to \Delta$ GPDs from equations 2.22 and 2.28 can be connected to the $N \to N$ isovector GPDs $E^u - E^d$, $\tilde{H}^u - \tilde{H}^d$ and $\tilde{E}^u - \tilde{E}^d$ according to

$$H_M(x,\xi,\Delta^2) = \frac{2}{\sqrt{3}}\left[E^u(x,\xi,\Delta^2) - E^d(x,\xi,\Delta^2)\right], \tag{2.33}$$

$$C_1(x,\xi,\Delta^2) = \sqrt{3}\left[\tilde{H}^u(x,\xi,\Delta^2) - \tilde{H}^d(x,\xi,\Delta^2)\right], \tag{2.34}$$

$$C_2(x,\xi,\Delta^2) = \frac{\sqrt{3}}{4}\left[\tilde{E}^u(x,\xi,\Delta^2) - \tilde{E}^d(x,\xi,\Delta^2)\right]. \tag{2.35}$$

This nicely shows how measurements of the associated DVCS process also comprises access to the nucleon GPDs. Through DVCS the general combination $\frac{4}{9}\tilde{H}^u + \frac{1}{9}\tilde{H}^d$ can be accessed, whereas $\tilde{H}^u - \tilde{H}^d$ yields the isovector part and therefore helps to carry out flavor decomposition of the nucleon GPDs [30].

The final step is the modification of the matrix elements for associated DVCS due to the

$\Delta \to N\pi$ decay. This is done by modifying the equations of vector and axial vector transitions in equations 2.22 and 2.28 to a final state $N\pi$ instead of Δ [25].

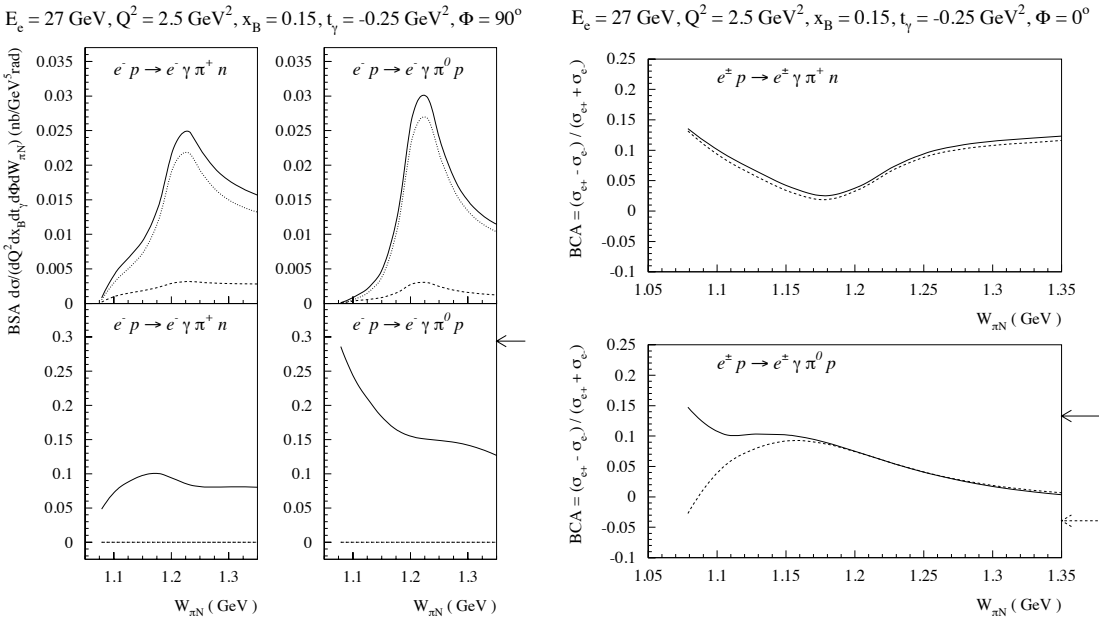

Figure 2.2.: The two upper panels on the left show the estimated cross section at HERMES kinematics. The corresponding lower panels show the estimated beam spin asymmetries. In case of $e^-p \to e^-\gamma\pi^0 p$ the arrow indicates the position of the asymmetry in the elastic case. The dashed curves indicate the contribution by associated DVCS whereas the dotted curves correspond the associated BH. The plots on the right show the estimated beam charge asymmetries. Again the arrow indicates the asymmetry in the elastic case (the dashed arrow and curve correspond to calculations without the D-term) [25].

In practice the final state is contributed by associated Bethe-Heitler (ABH, see also figure 2.2 upper left panels) which in addition to the elastic Bethe-Heitler (BH) can be calculated using the well known elastic form factors of the proton. When a pion is produced, the corresponding ABH amplitude is also involving the pion electro-production amplitude. Because the initial or final nucleon state is only an intermediate state and thus cannot be on-shell, the parametrization for the elastic case needs to be slightly generalized. Hereby the energy non-conservation is of the order of the pion mass itself. Figure 2.2 also shows the theoretically predicted values for the leading beam spin and beam charge asymmetries. The values for the processes $e^-p \to e^-\gamma p\pi^0$ and $e^-p \to e^-\gamma n\pi^+$ differ. The asymmetry for the $e^-p \to e^-\gamma p\pi^0$ process starts to grow when reaching the $N\pi$ threshold where it converges against the amplitude of the elastic process. This can be understood in the framework of the soft pion theorem, where the $e^-p \to e^-\gamma p\pi^0$ is obtained from the elastic $e^-p \to e^-\gamma p$ process by attaching a soft pion to the initial and final protons. The plots on the right side in figure 2.2

show the estimates of the leading beam charge asymmetry amplitudes. Approaching the $N\pi$ threshold both processes reach the same value as for the elastic DVCS. Additionally one can see that since the D-term (which restores the correct polynomiality for GPDs in the form of double distributions [22]) contributes only to the Born terms (which sums over all flavors and hence is sensitive to valence and sea quarks) it mainly manifests itself in the neutral pion production channel around threshold.

2.2. Experimental access to GPDs

2.2.1. Deeply virtual Compton scattering (DVCS)

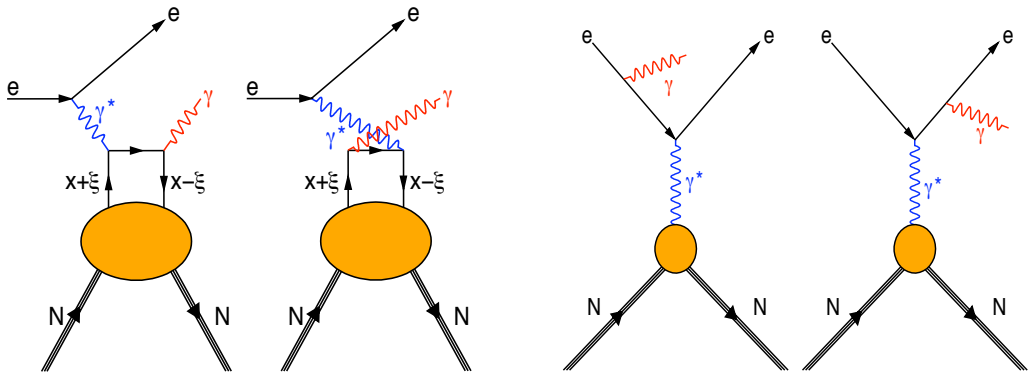

Figure 2.3.: On the left one sees the Feynman diagrams for deeply virtual Compton scattering (DVCS). Feynman diagrams on the right correspond to the Bethe-Heitler process (BH), which is dominant at HERMES kinematics.

GPDs appear in amplitudes of exclusive reactions such as:

$$\gamma^* + N \to M + N', \tag{2.36}$$

with a highly virtual photon γ^*, a real final state photon or meson M and a hadronic state N. There are in principle two reactions which satisfy this prerequisite: deeply virtual Compton scattering (DVCS) and hard exclusive meson production (HEMP, also known as deeply virtual meson production DVMP). DVCS is the theoretically cleanest access because the meson form factors needed for HEMP are not precisely known. However this advantage of DVCS is to some extend counterbalanced by the experimental difficulty to measure it.
DVCS can be described according to the Feynman diagram in figure 2.3, where an incoming lepton interacts with a quark inside the hadron via a virtual photon. The change in momentum of the quark is thereby expressed by the skewedness parameter ξ. However the

quark stays within the nucleon and a real photon is emitted. The four fould cross section for electroproduction of photons off an unpolarized nucleon target can be written as [31]

$$\frac{\mathrm{d}^4\sigma}{\mathrm{d}Q^2\mathrm{d}x_B\mathrm{d}t\mathrm{d}\phi} = \frac{x_B e^6}{32(2\pi)^4 Q^2\sqrt{1+\epsilon^2}}\,|\tau_{total}|^2, \tag{2.37}$$

where the square of the scattering amplitude τ_{total} is given by

$$|\tau_{\mathrm{total}}|^2 = |\tau_{\mathrm{BH}}|^2 + |\tau_{\mathrm{DVCS}}|^2 + \mathcal{I}, \tag{2.38}$$

and

$$\mathcal{I} = \tau_{\mathrm{BH}}\tau^*_{\mathrm{DVCS}} + \tau_{\mathrm{DVCS}}\tau^*_{\mathrm{BH}}, \tag{2.39}$$

with the Bjorken scaling variable x_B, the Mandelstam variable t (formally expressed as Δ^2), the photon virtuality Q^2, $\epsilon = 2x_B\frac{M_N}{Q}$ with the nucleon mass M_N, the elementary charge e and the angle ϕ (see equation 2.87). In the limit of perturbative QCD the skewedness parameter ξ can be related to the Bjorken variable x_B via

$$\xi = \frac{x_B/2}{1 - x_B/2}. \tag{2.40}$$

At HERMES kinematics the BH process is the dominating process and with a cross section of about one hundred times higher than the cross section of DVCS (see also figure 2.4). However the cross section of the BH process is well known and in case of the interference term $\mathcal{I}$ also amplifying the suppressed DVCS amplitude. Therefore the interference term is the main reason why measurement of DVCS at HERMES was possible.

2.2.2. Extraction of asymmetry amplitudes

The contribution of the amplitudes of τ_{BH}, τ_{DVCS} and the interference term $\mathcal{I}$ for an unpolarized target can be Fourier expanded in ϕ:

$$|\tau_{BH}|^2 = \frac{K_{BH}}{P_1(\phi)\mathcal{P}_2(\phi)}\left(c_0^{BH} + \sum_{n=1}^{2} c_n^{BH}\cos(n\phi)\right), \tag{2.41}$$

$$|\tau_{DVCS}|^2 = K_{DVCS}\left(c_0^{DVCS} + \sum_{n=1}^{2}\cos(n\phi) + \lambda s_1^{DVCS}\sin(\phi)\right), \tag{2.42}$$

$$\mathcal{I} = \frac{-\eta K_{\mathcal{I}}}{\mathcal{P}_1(\phi)\mathcal{P}_2(\phi)}\left(c_0^{\mathcal{I}} + \sum_{n=1}^{3} c_n^{\mathcal{I}}\cos(n\phi) + \lambda\sum_{n=1}^{2} s_n^{\mathcal{I}}\sin(n\phi)\right), \tag{2.43}$$

where η is the charge of the incoming beam lepton (±1), λ is the beam polarization and the lepton propagators $\mathcal{P}_1$ and $\mathcal{P}_2$ are defined as

$$Q^2\mathcal{P}_1 \equiv (k - q')^2, \tag{2.44}$$

$$Q^2\mathcal{P}_2 \equiv [k - (p' - p))]^2. \tag{2.45}$$

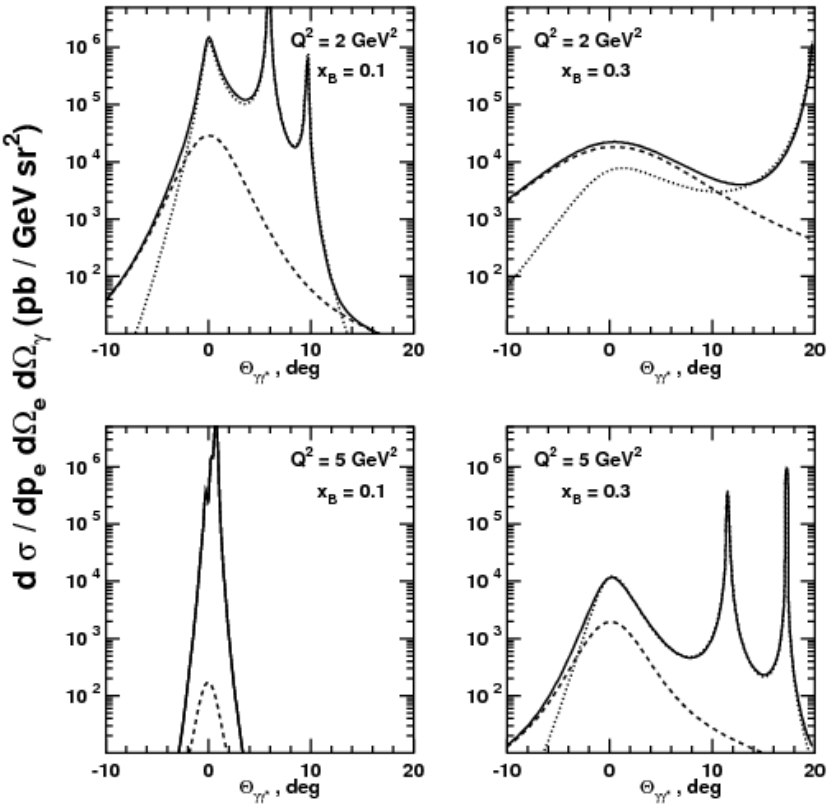

Figure 2.4.: Illustration of the behaviour of the differential in-plane cross section as a function of the polar angle (see equation 2.86) between the virtual and the real photon for DVCS (dashed lines), Bethe-Heitler (dotted lines) and total γ production (solid lines) in e^+p interactions at a HERMES energy of $E_e = 27.5$ GeV. Different panels are for different values of x_B and Q^2. The three-pole structure of the BH cross section is due to the propagators of the virtual electrons and the virtual photon [32].

The kinematic factors used in equations 2.41-2.43 are defined as

$$K_{BH} = \frac{8(2\pi)^2\alpha^3 Q^2}{x_B^2 y t e^3 (1+\epsilon^2)^2}, \tag{2.46}$$

$$K_{DVCS} = \frac{8(2\pi)^2\alpha^3}{y e^3}, \tag{2.47}$$

$$K_{\mathcal{I}} = \frac{8(2\pi)^2\alpha^3 Q^2}{x_B y^2 t e^3}. \tag{2.48}$$

The cross section which is independent of beam polarization and charge can be expressed as (the first (second) letter of the subscript stands for the polarization of the beam (target) which is either U for unpolarized or L for longitudinally polarized; the upper index stands

for the beam charge)

$$\begin{aligned}\sigma^0_{\mathrm{UU}}(\phi) = \frac{x_B e^6}{32(2\pi)^4 Q^4\sqrt{1+\epsilon^2}} \Bigg[&\frac{K_{BH}}{\mathcal{P}_1(\phi)\mathcal{P}_2(\phi)} \left(c_0^{BH} + \sum_{n=1}^{2} c_n^{BH}\cos(n\phi) \right) \\ &+ K_{DVCS} \left(c_0^{DVCS} + \sum_{n=1}^{2} c_n^{DVCS}\cos(n\phi) \right) \Bigg],\end{aligned} \tag{2.49}$$

and can be extended to the case of a certain beam charge η

$$\begin{aligned}\sigma^\eta_{\mathrm{UU}}(\phi,\eta) = \sigma^0_{\mathrm{UU}}(\phi) \\ + \frac{x_B e^6}{32(2\pi)^4 Q^4\sqrt{1+\epsilon^2}} \left[\frac{-\eta K_{\mathcal{I}}}{\mathcal{P}_1(\phi)\mathcal{P}_2(\phi)} \left(c_0^{\mathcal{I}} + \sum_{n=1}^{3} c_n^{\mathcal{I}}\cos(n\phi) \right) \right].\end{aligned} \tag{2.50}$$

Beam spin asymmetry

Using the previous equations the cross section in 2.37 can be rewritten as

$$\sigma^\eta_{LU}(\phi,\lambda) = \sigma^\eta_{UU}[1 + \lambda A^\eta_{LU}(\phi)] \tag{2.51}$$

with the beam spin asymmetry

$$\begin{aligned}A^\eta_{\mathrm{LU}}(\phi,\eta) &= \frac{\sigma^\eta_{\mathrm{LU}}(\phi,\lambda=+1) - \sigma^\eta_{\mathrm{LU}}(\phi,\lambda=-1)}{\sigma^\eta_{\mathrm{LU}}(\phi,\lambda=+1) + \sigma^\eta_{\mathrm{LU}}(\phi,\lambda=-1)} \\ &= \frac{1}{\sigma^\eta_{\mathrm{UU}}(\phi,\eta)} \left[K_{DVCS}\, s_1^{DVCS}\sin\phi - \frac{\eta K_{\mathcal{I}}}{\mathcal{P}_1(\phi)\mathcal{P}_2(\phi)} \sum_{n=1}^{2} s_n^{\mathcal{I}}\sin(n\phi) \right].\end{aligned} \tag{2.52}$$

From the last term in equation 2.52 one can see that the amplitudes s^{DVCS} and $s^{\mathcal{I}}$ cannot be disentangled if only one beam charge is available. This is the case for the present analysis since for the electron beam no Recoil measurement with positive beam helicity is available ($\eta = +1$ only, please refer to chapter 5 for further details). However the s^{DVCS} amplitude is highly suppressed why it can be neglected (see figure 2.4).

Beam charge asymmetry

The beam charge asymmetry can be extracted using equation 2.50 and the cross section

$$\sigma^\eta_{UU}(\phi,\eta) = \sigma^0_{UU}[1 + \eta A_C(\phi)], \tag{2.53}$$

with

$$\begin{aligned}A_C(\phi) &= \frac{\sigma^\eta_{\mathrm{UU}}(\phi,\eta=+1) - \sigma^\eta_{\mathrm{UU}}(\phi,\eta=-1)}{\sigma^\eta_{\mathrm{UU}}(\phi,\eta=+1) + \sigma^\eta_{\mathrm{UU}}(\phi,\eta=-1)} \\ &= \frac{1}{\sigma^0_{\mathrm{UU}}(\phi)} \left[-K_{\mathcal{I}} \sum_{n=0}^{3} c_n^{\mathcal{I}}\cos(n\phi) \right].\end{aligned} \tag{2.54}$$

In the case of HERMES this is only an approximation since the data was taken using a longitudinally polarized beam.

Connection to Compton form factors and GPDs

Due to the dominance of the leading twist (twist-2) amplitudes of the interference term in equations 2.52 and 2.54, these equations can be reduced and linked to the Compton form factors (CFFs) $\mathcal{H}$, $\tilde{\mathcal{H}}$ and $\mathcal{E}$ by

$$A_{LU}^{\eta} \approx \eta \frac{s_1^{\mathcal{I}}}{c_0^{BH}} \sin(\phi) \propto \mathrm{Im}\left\{ F_1\mathcal{H}_1 + \frac{x_B}{2-x_B}(F_1+F_2)\tilde{\mathcal{H}}_1 - \frac{Q^2}{4M^2}F_2\mathcal{E}_1 \right\}, \tag{2.55}$$

$$A_{C}^{\eta} \approx \frac{c_1^{\mathcal{I}}}{c_0^{BH}} \cos(\phi) \propto \mathrm{Re}\left\{ F_1\mathcal{H}_1 + \frac{x_B}{2-x_B}(F_1+F_2)\tilde{\mathcal{H}}_1 - \frac{Q^2}{4M^2}F_2\mathcal{E}_1 \right\}. \tag{2.56}$$

The Compton form factors are convolutions of the GPDs and are related according to

$$\mathrm{Re}\mathcal{H}_1 = \sum_q e_q^2 \left[P\int_{-1}^{1} \mathrm{d}x H(x,\xi,\Delta^2)\left(\frac{1}{x-\xi}+\frac{1}{x+\xi}\right)\right], \tag{2.57}$$

$$\mathrm{Re}\tilde{\mathcal{H}}_1 = \sum_q e_q^2 \left[P\int_{-1}^{1} \mathrm{d}x \tilde{H}(x,\xi,\Delta^2)\left(\frac{1}{x-\xi}-\frac{1}{x+\xi}\right)\right], \tag{2.58}$$

$$\mathrm{Im}\mathcal{H}_1 = -\pi \sum_q e_q^2 \left(H(x,\xi,\Delta^2) - H(-x,\xi,\Delta^2)\right), \tag{2.59}$$

$$\mathrm{Im}\tilde{\mathcal{H}}_1 = -\pi \sum_q e_q^2 \left(\tilde{H}(x,\xi,\Delta^2) - \tilde{H}(-x,\xi,\Delta^2)\right) \tag{2.60}$$

where P denotes Cauchy's principle value and q stands for the quark flavors u, d and s. The CFFs $\mathcal{E}_1$ and $\tilde{\mathcal{E}}_1$ can be expressed through E and $\tilde{E}$ analogously.
Due to low values of x_B and $|t|$ at HERMES kinematics equations 2.55 and 2.56 to first approximation only depend on the CFF $\mathcal{H}$ and hence GPD H [31], [32].

2.2.3. The extended maximum likelihood method

In order to extract the asymmetries in principal two methods are available. The least squares method is easier to implement and mainly serves as a crosscheck. The final analysis is using an extended maximum likelihood method.
Therefore n independently measured azimuthal angles ϕ_i (see also equation 2.87) are used. They are belonging to a probability density function according to

$$\int p(\phi;\vec{\theta})\mathrm{d}\phi = 1, \tag{2.61}$$

where $\vec{\theta}$ is a set of m unknown parameters which can be identified with coefficients in 2.52 and 2.54. This set of parameters can be estimated by maximizing the likelihood function $\mathscr{L}(\vec{\theta})$. The standard maximum likelihood method (SML) is defined as

$$\mathscr{L}(\vec{\theta}) = \prod_i^n p(\phi_i;\vec{\theta}) \tag{2.62}$$

The number of observed events has a Poisson fluctuation about its expected value $\mathcal{N}(\vec{\theta})$, which in our case also depends on the parameters. Therefore the standard maximum likelihood is extended to include the Poisson probability density function and becomes the extended maximum likelihood function (EML)

$$\mathscr{L}(\vec{\theta}) = \frac{[\mathcal{N}(\vec{\theta})]^n e^{-\mathcal{N}(\vec{\theta})}}{n!} \prod_i^n p(\phi_i;\vec{\theta}). \tag{2.63}$$

Hereby $\mathcal{N}$ can also be interpreted as the normalization of the extended probability density function $\mathscr{P}(\phi_i;\vec{\theta}) \equiv p(\phi_i;\vec{\theta})\mathcal{N}(\vec{\theta})$

$$\mathcal{N}(\vec{\theta}) = \int \mathscr{P}(\phi_i;\vec{\theta})\mathrm{d}\phi \tag{2.64}$$

The resulting negative log-likelihood function to be minimized then reads

$$-\ln \mathscr{L}_{EML}(\vec{\theta}) = -\sum_i^n \ln \mathscr{P}(\phi_i;\vec{\theta}) + \mathcal{N}(\vec{\theta}). \tag{2.65}$$

In case of the beam spin asymmetry the function to be minimized is

$$-\ln \mathscr{L}_{EML}(\vec{\theta}) = -\sum_i^n \ln[1 + \lambda_i A_{LU}(\phi_i;\vec{\theta})] + \mathcal{N}(\vec{\theta}), \tag{2.66}$$

with

$$A_{LU}(\phi_i;\vec{\theta}) = c_0 + s_1 \sin(\phi) + s_2 \sin(\phi), \tag{2.67}$$

which is an approximation of equation 2.51, in which c_0 has to be zero and can therefore be seen as a test for correct normalization given by

$$\mathcal{N} = \frac{DIS^+}{\overrightarrow{DIS^+}} \frac{\sum_i^{\overrightarrow{n}} [1 + \langle\lambda\rangle A_{LU}(\phi_i;\vec{\theta})]}{\left[1 - \frac{\langle\overrightarrow{\lambda}\rangle}{\langle\overleftarrow{\lambda}\rangle}\right]} + \frac{DIS^+}{\overleftarrow{DIS^+}} \frac{\sum_i^{\overleftarrow{n}} [1 + \langle\lambda\rangle A_{LU}(\phi_i;\vec{\theta})]}{\left[1 - \frac{\langle\overleftarrow{\lambda}\rangle}{\langle\overrightarrow{\lambda}\rangle}\right]}, \tag{2.68}$$

with the average beam polarization $\langle\lambda\rangle$, also for positive ($\rightarrow$) and negative ($\leftarrow$) beam helicity.
In case of the beam charge asymmetry the function to be minimized reads

$$-\ln \mathscr{L}_{EML}(\vec{\theta}) = -\sum_i^n \ln[1 + \eta_i A_C(\phi_i;\vec{\theta})] + \mathcal{N}(\vec{\theta}), \tag{2.69}$$

with

$$A_C(\phi_i;\vec{\theta}) = c_0 + c_1 \cos(\phi) + c_2 \cos(2\phi) + c_3 \cos(3\phi), \tag{2.70}$$

which is an approximation of equation 2.53 with $\vec{\theta} = \{c_0, c_1, c_2, c_3\}$. The normalization is calculated according to

$$\mathcal{N} = \frac{DIS}{2\,DIS^+} \sum_i^{n^+} [1 + \langle\eta\rangle A_{LU}(\phi_i;\vec{\theta})] + \frac{DIS}{2\,DIS^-} \sum_i^{n^-} [1 + \langle\eta\rangle A_{LU}(\phi_i;\vec{\theta})] \tag{2.71}$$

with the average beam charge $\langle\eta\rangle$ (+ for positive and − for a negative beam charge).
In both cases the number of measured DIS events N_{DIS} is used instead of the measured luminosities. This is valid in good approximation and also takes into account detector efficiencies [33].

2.3. Kinematic variables

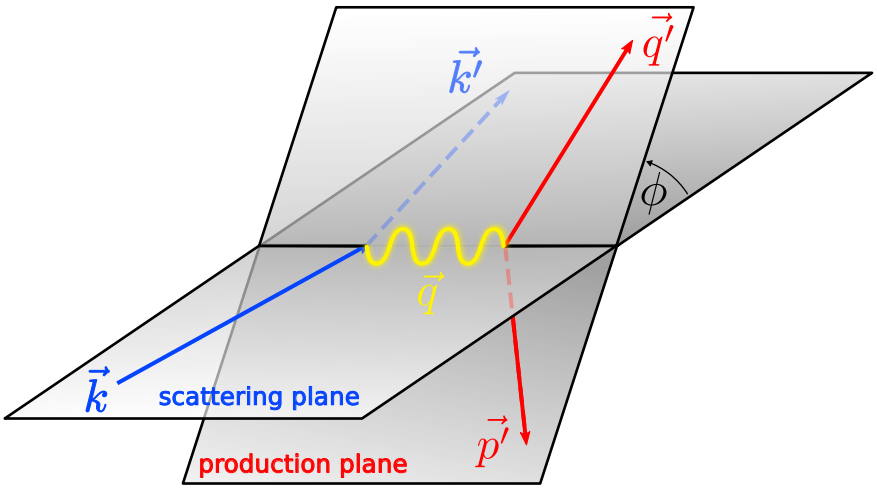

Figure 2.5.: Diagram to illustrate DVCS kinematics according to equation 2.72 with ϕ being the angle between the lepton scattering plan and the photon production plane (see eq. 2.87).

Exclusive leptoproduction of a real photon on nucleon target N is denoted as

$$l(k) + N(p) \to l(k') + \gamma(q') + N'(p'), \tag{2.72}$$

which is illustrated in figure 2.5. The kinematics are also valid for the associated case, where the neutral final state particle (which is not shown in equation 2.72) cannot be measured and N' can either be a proton or a π^+.
Below one can find the definitions of the kinematic variables used in this thesis.
Using the beam energy E_B, the four-momenta of the incoming (k) and scattered lepton (k') are

$$k \overset{\text{lab}}{=} (E_B, \vec{k}) \tag{2.73}$$

$$k' \overset{\text{lab}}{=} (E', \vec{k'}), \tag{2.74}$$

which determine the four-momentum and energy of the virtual photon

$$q = k - k' \overset{\text{lab}}{=} (E_B - E', \vec{k} - \vec{k'}), \tag{2.75}$$

$$\nu = \frac{Pq}{m_p} \overset{\text{lab}}{=} (E_B - E'), \tag{2.76}$$

the fractional energy of the virtual photon

$$y = \frac{Pq}{Pk} = \frac{\nu}{E_B}, \tag{2.77}$$

and the negative squared four-momentum transfer from the lepton to the virtual photon

$$Q^2 \equiv -q^2 := -(k-k')^2 \overset{\text{lab}}{\approx} 4E_B E' \sin^2(\theta_e/2). \tag{2.78}$$

The real photon's energy E_γ can be measured in the electromagnet calorimeter of the forward spectrometer. Its three-momentum vector can be calculated from the vector pointing from the scattered lepton beam vertex to the location where the photon hit the calorimeter ($\vec{r}_\gamma$):

$$\vec{P}_\gamma = E_\gamma \cdot \frac{\vec{r}_\gamma}{|\vec{r}_\gamma|}. \tag{2.79}$$

Other important variables with respect to the kinematic dependence of the GPDs are the Bjorken scaling variable

$$x_B = \frac{Q^2}{2Pq} = \frac{Q^2}{2M/\nu}, \tag{2.80}$$

the Mandelstam invariant

$$t \equiv (P - P_0), \tag{2.81}$$

which can be calculated using the photon energy via

$$t = -Q^2 - 2E_\gamma \left(\nu - \sqrt{\nu^2+Q^2}\cos\theta_{\gamma\gamma^*}\right), \tag{2.82}$$

or independent of the photon energy but constrained on the proton mass

$$t_c^{DVCS} = \frac{-Q^2 - 2\nu\left(\nu - \sqrt{\nu^2+Q^2}\cos\theta_{\gamma\gamma^*}\right)}{1+\frac{1}{m_p}\left(\nu - \sqrt{\nu^2+Q^2}\cos\theta_{\gamma\gamma^*}\right)}, \tag{2.83}$$

or the mass of the Δ resonance

$$t_c^{\Delta} = \frac{-Q^2 - 2\nu\left[\frac{m_p^2-m_\Delta^2}{2m_p}+\nu\right] + 2\sqrt{\nu^2+Q^2}\cos\theta_{\gamma\gamma^*}\left[\frac{m_p^2-m_\Delta^2}{2m_p}+\nu\right]}{1+\frac{\nu}{m_p} - \frac{\sqrt{\nu^2+Q^2}\cos\theta_{\gamma\gamma^*}}{m_p}}. \tag{2.84}$$

In parts of the analysis a missing mass is used

$$M_x^2 = (k-k'+P_0-P_\gamma)^2 = M^2 + 2M(\nu - E_\gamma) + t. \tag{2.85}$$

The angle between real and virtual photon is defined by

$$\theta_{\gamma\gamma^*} = \arccos\left(\frac{\vec{q}\cdot\vec{P}_\gamma}{|\vec{q}||\vec{P}_\gamma|}\right). \tag{2.86}$$

The azimuthal angle between lepton scattering plane and photon production plane can be calculated according to

$$\phi = \arccos\frac{\left(\vec{q}\times\vec{k}\right)\cdot\left(\vec{q}\times\vec{P}_\gamma\right)}{\left|\vec{q}\times\vec{k}\right|\left|\vec{q}\times\vec{P}_\gamma\right|} \times \frac{\vec{P}_\gamma\cdot\vec{q}\times\vec{k}}{\left|\vec{P}_\gamma\cdot\vec{q}\times\vec{k}\right|}. \tag{2.87}$$

3. The HERMES experiment

3.1. HERA at DESY

HERA (*Hadron-Elektron-Ring-Anlage*) was a lepton-proton collider at DESY (*Deutsches Elektronen-Synchrotron*) at Hamburg, Germany. It consisted of two concentric beams with a circumference of 6.331 km each. One beam was a 920 GeV proton beam and the other one a lepton (electron/positron) beam at 27.6 GeV. The lepton beam was filled by several pre-accelerators starting with Linac II (up to 450 MeV), DESY-II (7.5 GeV) and finally PETRA (12 GeV). In the HERA the leptons were arranged in 170, about 8 mm long bunches, which passed through the experiment between intervals of 96 *ns*. Four experimental halls gave access to the beams. The north and south hall were occupied by the H1 and ZEUS experiment respectively. Both were collider experiments using both, the lepton and the proton beam. HERA-B was in operation only during the years 2001 till 2003 and located in the west hall using only the halo of the proton beam. The HERMES experiment was a fixed target experiment located in the east hall using the lepton beam only.

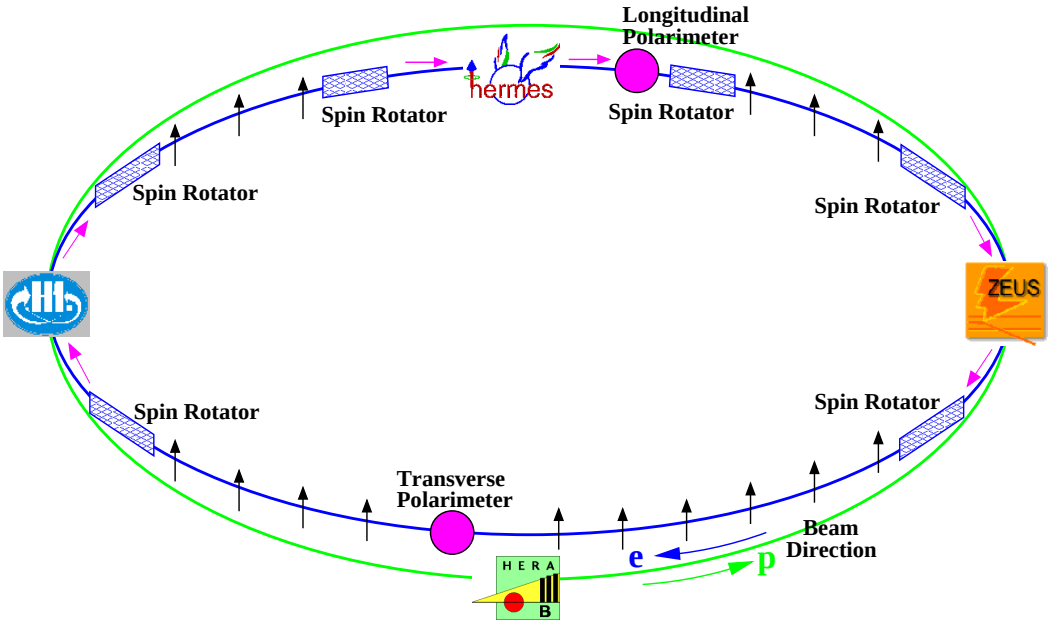

Figure 3.1.: Schematic overview of HERA setup from 2002 - 2007 [34]

HERA was the first high-energy storage ring with longitudinal polarization of electron/positron beams. The originally unpolarized lepton beam was subject to self-polarization due to Sokolov-Ternov effect [35]. Here the leptons emit synchrotron radiation passing through the magnetic dipole fields in the arcs. The synchrotron radiation contains a small asymmetric spin-flip amplitude which leads to a polarization parallel for positrons and antiparallel for electrons with respect to the magnetic field of the dipoles. The theoretical maximum of the polarization build up at HERA is given by 92.38 %. Due to depolarization effects such as

a not perfectly parallel spin motion to the beam, horizontal and longitudinal betatron and synchrotron oscillations by misaligned quadrupole magnets, the real polarization was much lower (see figure 5.1). In order to have longitudinally polarized beam, spin rotators before and after the interaction point (see figure 3.1) had been installed. The spin rotation of 90° was achieved by interleaved horizontal and vertical dipole magnets (a detailed description can be found in [36]). At first HERMES was the only experiment with a longitudinally polarized beam. The spin rotators for the experiments H1 and ZEUS were installed in 2001.
The HERA polarimeters deserve special attention since they were crucial devices for all experiments. The transverse and longitudinal polarization of the lepton beam was measured simultaneously by the transverse polarimeter (TPOL) isolated in the HERA west section and the longitudinal polarimeter (LPOL) located downstream of HERMES (see figure 3.1). Both were using the spin dependent cross section for Compton scattering of circularly polarized photons on polarized electrons from the beam. In case of the transversally polarized beam a small up-down asymmetry in the y-direction (transversal to the beam) of the back-scattered photons from two different helicity states of the laser beam can be observed in a calorimeter. The TPOL's systematic uncertainty was 3.4 % [37]. In case of the LPOL an asymmetry in the laser produced backscattered photons' energy was measured. Its systematic uncertainty was 1.6 % [38].

3.2. The HERMES forward spectrometer

The HERMES experiment was built between 1993 and 1995 and started data taking subsequently. In 2006 it was upgraded with the Recoil detector [39] as shown in figure 3.2. In case of DVCS the forward spectrometer had to identify the scattered lepton and real photon and measure their kinematics. This section briefly describes different detector types and devices used for this purpose. In general the forward spectrometer consisted of two symmetric halves which were separated by the beam pipes. The spectrometer's dipole magnet with an integrated field strength of 1.3 Tm divided each half in a front and back part. The maximum angular acceptance was ±170 mrad (horizontally) and ±140 mrad (vertically). The minimum angular acceptance of ±40 mrad was due to an iron plate which shields the beams against the magnetic field of the dipole.

Tracking devices

The track reconstruction for charged particles in the forward spectrometer was done using wire chambers. The drift vertex chambers (DVC) as well as the front (FC) and back chambers (BC) were horizontal-drift chambers, consisting of alternating cathode wires and anode sense wires between a pair of cathode foils. In case of the magnet chambers (MC) multi wire

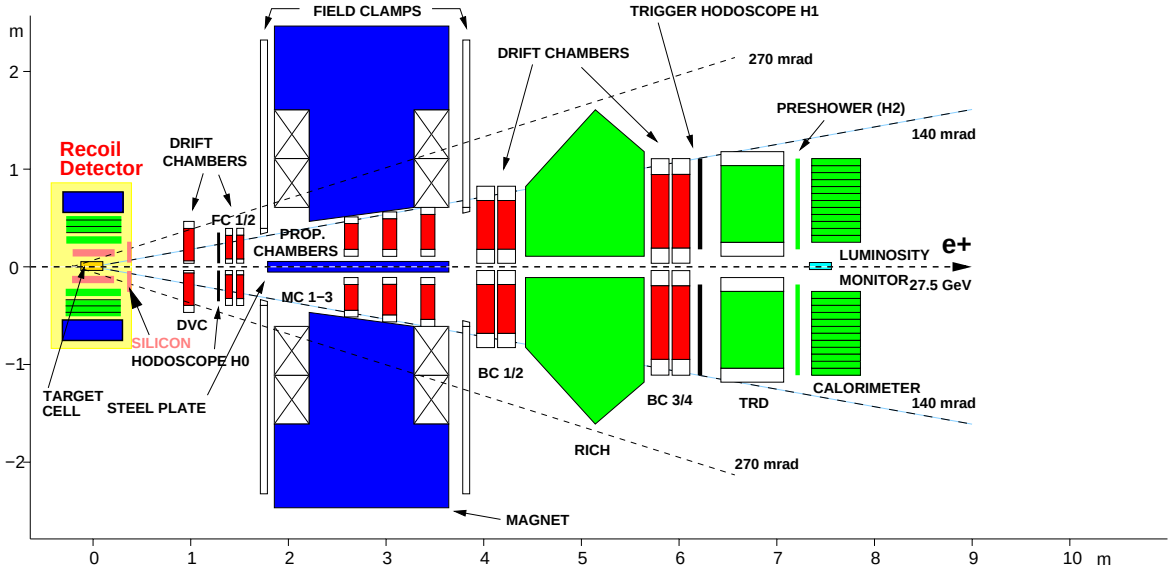

Figure 3.2.: Side view of the HERMES forward spectrometer during the data taking period 2006 and 2007 with the recoil detector being installed. Magnets are colored blue, PID devices green and tracking devices red.

proportional chambers were used. Each detector consisted of at least six planes of wires in pairs of U-, V-. X-coordinates. The X-planes were tautened vertically whereas the U- and V-planes were tilted by $\pm 30°$. This method had been chosen over a setup using X- and Y-planes which would be easier in terms of the track reconstruction but has mechanical disadvantages. The gas filling of the wire chambers was done with a non-flammable gas mixture of Ar (90 %), CO_2 (5 %), CF_4 (5 %). The resolution of a single plane was given between 220 and 300 μm for the drift chambers and 700 μm in case of the MWPCs [36]. The track reconstruction was done using a fast tree search algorithm [40]

The photon reconstruction was done with the calorimeter, which also served for other purposes such as particle identification (lepton/ hadron separation), trigger for electrons with a certain energy and of course energy measurement. It consisted of 840 lead glass blocks with a quadratic profile of 9 by 9 cm and a length of 50 cm (which corresponds to 18 radiation lengths) each read out by photomultiplier tubes (PMTs) and had an energy resolution of [41]

$$\frac{\sigma(E)}{E} = \frac{(5.1 \pm 1.0)\%}{\sqrt{E[\mathrm{GeV}]}} + (1.5 \pm 0.5)\% \tag{3.1}$$

Particle identification

At the HERMES forward spectrometer four different detectors were contributing to the particle identification (PID): a ring imaging Cherenkov detector (RICH), a transition radiation detector (TRD), a preshower detector and the previously described electromagnetic calorimeter. The purpose in the context of this analysis was the correct identification of the lepton

track and hence discrimination between hadron and lepton tracks. In case of the electromagnetic calorimeter this was done by measuring the deposited energy in the block of impact and the surrounding blocks, which results in 3 by 3 array, and compare it to the particle's momentum. Due to the rather long nuclear interaction length for hadrons and the relatively large width of the hadronic shower, the ratio $E_{cal,3x3}/p$ will be a mostly broad peak around 0.35, whereas the ratio for electrons and positron will give a clear peak at 1.
The preshower detector consisted of 42 plastic scintillators behind 1.1 cm of lead, which were read out by PMTs. It was supposed to complete the calorimeter and to enhance the difference in topology. Whereas the hadrons left a minimum ionizing signal, the deposited energy by electrons and positrons was roughly proportional to $\ln E$, which also gave information on the particle's identity. The preshower detector also served as the hodoscope H2, which together with the hodoscope H1 and the calorimeter formed a trigger.
The TRD was built of 12 modules (6 above and 6 below the beam). Transition radiation (TR) is emitted by a highly relativistic charged particle that crosses the boundary between two materials with different dielectric constants, the radiator. Each module consisted of a 63.5 mm thick fibre radiator and a MWPC for the readout. The transition radiation photon is emitted in forward direction with an energy proportional the Lorentz γ of the trespassing particle and in the range of X-rays. In order to gain information on the particle identity, the difference between $\mathrm{d}E/\mathrm{d}x$ (for low γ hadrons) and $\mathrm{d}E/\mathrm{d}x + TR$ (for high γ electrons/-positrons) has to be measured [42].
In 1998 the threshold Cherenkov detector was replaced by a RICH which is not used in this analysis. The particle information therefore is deduced from the combined preshower and Calorimeter PID likelihood ratio (PID2) and a callibrated TRD PID ratio (PID5).

3.3. The HERMES Recoil detector

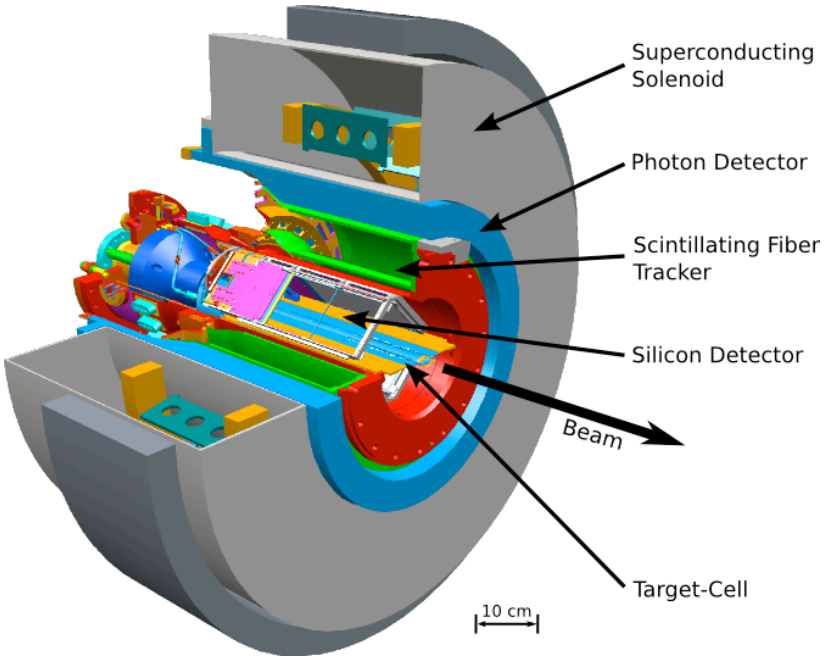

Figure 3.3.: Sectional view of the HERMES Recoil detector.

The HERMES Recoil detector (pictured in figure 3.3) was able to measure recoiling particles with low momenta and angles between 0.5 and 1.3 rad. It was enclosed by a superconducting solenoid with a magnetic field of 1 T at the center of the bore. The field was induced by two superconducting coils, which were separated by 19.8 cm in a Helmholtz configuration and cooled by liquid helium. It provided the field for momentum reconstruction and prevented Moeller electrons from reaching the SSD.

The very inside of the Recoil detector was occupied by a modified target cell. This cell consisted of an elliptical aluminum tube with a thickness of 75 μm, an overall length of 15 cm and an horizontal (vertical) stretch of 3 cm (2 cm). In comparison to the previous target cell it had been shifted to achieve optimal acceptance for the Recoil detector and the forward spectrometer. Due to repeated damage to the target cell it had to be partially redesigned [43].

Still within the beam vacuum chamber and only 5 cm away from the lepton beam, the SSD was installed [44]. It consisted of 16 double-sided silicon strip sensors arranged in a diamond like structure in two layers. Optimized for low momentum particles down to 125 MeV/c, the passive material was reduced as much as possible (see also figure 3.5). Unfortunately the SSD was not operational during the electron beam period and therefore is not considered in the framework of the presented analysis.

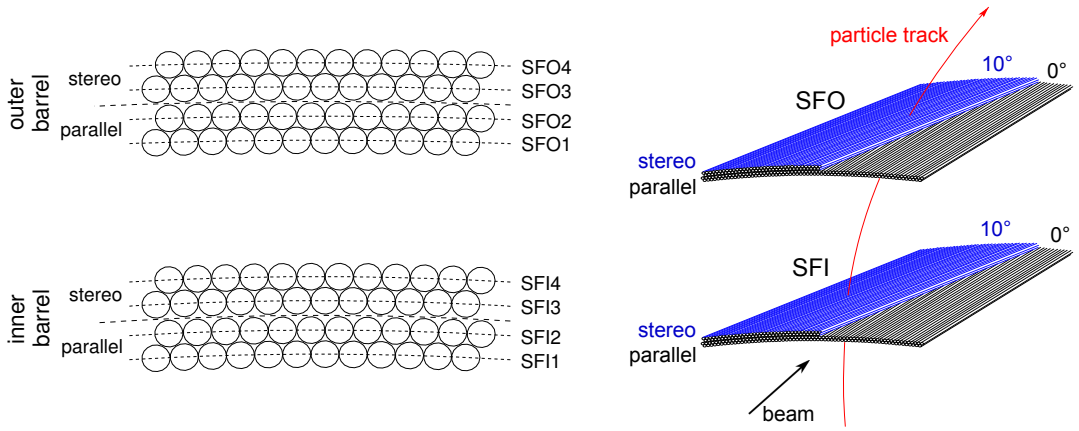

Figure 3.4.: The drawing shows a profil of the inner and out layers of the scintillating fibre tracker (left) and a particle track trespassing through the layers (right, both not to scale).

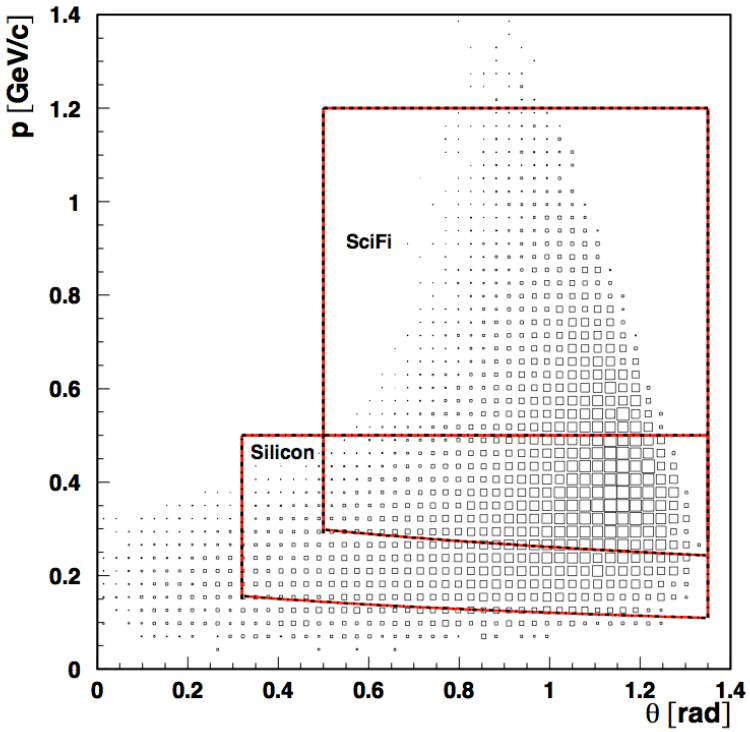

Figure 3.5.: The plot shows the acceptance for the different subdetectors of the HERMES Recoil detector for the kinematic variables p und θ. One can nicely see how the scintillating fibre tracker (SciFi) and the silicon strip detector (Silicon) complement one another.

Directly attached to the 1 mm thick aluminum vacuum chamber, the scintillating fibre tracker (SFT) was mounted [45]. Two concentric barrels of scintillating fibers with the radii of 108 mm for the inner and 183 mm for the outer barrel and an active length of 28 cm allowed for a 4π detection in the azimuthal projection and an acceptance between 0.7 and 1.35 rad (figure 3.5). Both barrels consisted of two subbarrels with a parallel and a stereo layer, where

the fibers are inclined by 10° to allow spacial reconstruction (see figure 3.4). The far-end (downstream) fibers were metallized in order minimize light losses, whereas the near-end (upstream) fibres were glued into custom made connectors. In total 4923 channels were read out by 78 64-channel multi-anode photomultiplier tubes Hamamatsu R5900-00-M64.
Further details can be found in the technical design report [39].

3.4. Track reconstruction with the HERMES Recoil detector

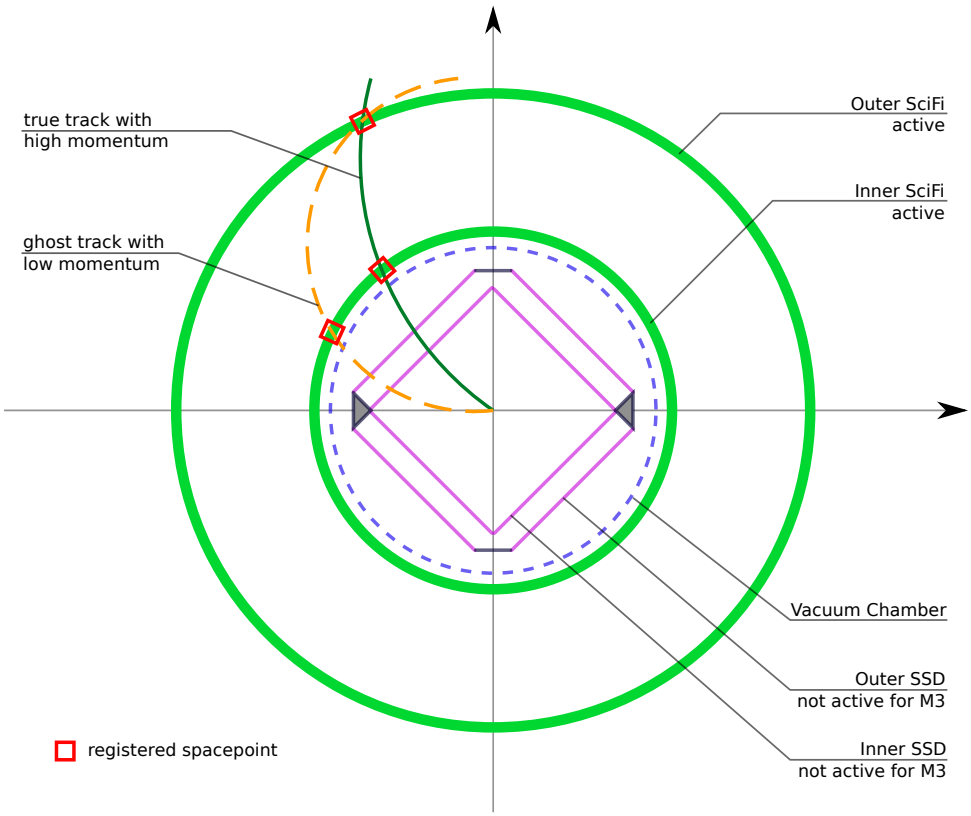

Figure 3.6.: Schematic example of track reconstruction using the scintillating fibre tracker only. In this example the inner layer has recorded two hit points whereas the outer layer has recorded only one.

For the track reconstruction inside the Recoil detector two main methods exist. The more sophisticated reconstruction was done with method 7 (refer to [46] and [47] for further details). However this method requires a fully operational SSD which wasn't available during the electron beam period and hence only tracks taken during runs with the positron beam could be reconstructed with method 7.
In order to measure the recoiling proton for both beam charges method 3 is used. It is solely based on the spacepoints recorded by the scintillating fibre tracker. These spacepoints were

formed considering geometrically allowed combinations of clusters in the parallel and stereo layers. Since the energy deposits from the different layers were only weakly correlated, no hard restrictions could be applied and ghost spacepoints were unavoidably created. In the simple reconstruction the recoiling particle was supposed to be a pion and with respect to the bending in the magnetic field of the Recoil detector its transverse momentum p_t and its polar and azimuthal angle (θ and ϕ) were reconstructed. This has been done for all combinable pairs of hit points from the inner and outer layer of the scintillating fibre tracker. Since this calculation has no degrees of freedom left, real tracks and ghost tracks cannot be distinguished (see figure 3.6). This is especially challenging because of high track multiplicities inside the Recoil detector.

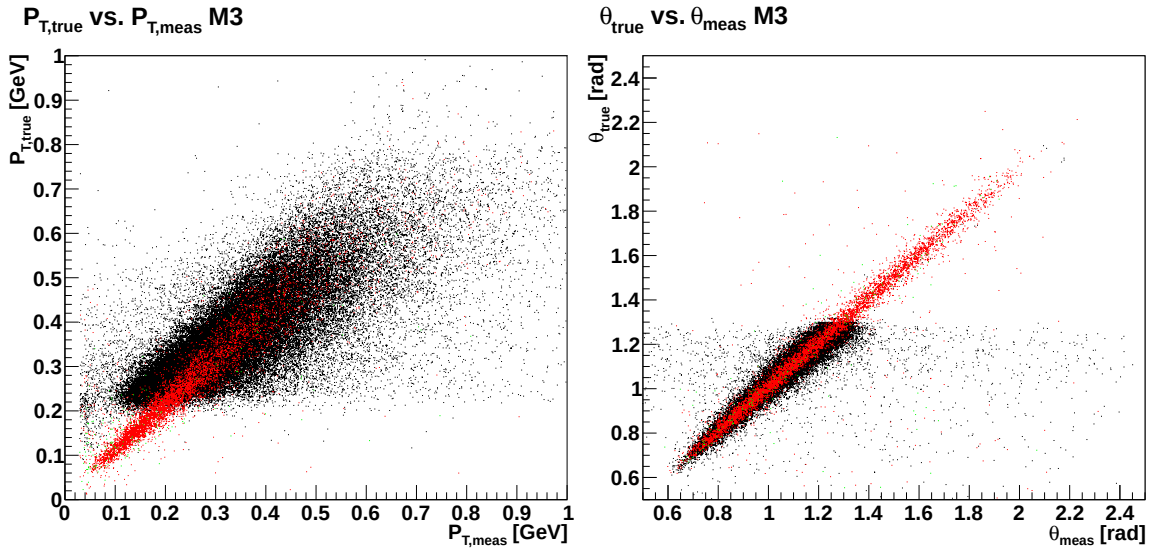

Figure 3.7.: The above plots compare true and measured kinematics according to Monte Carlo. Proton events are colored black, positively charged pions red and other particles green (hardly visible). In addition one can see that the resolution is broadened for protons and that protons with a momentum below 0.25 GeV do not pass through both layers of the SFT (left) and that no elastic protons are measured for angles greater than 1.3 rad (right).

The application of a pion hypothesis for the determination of the particle momentum naturally results in a wrong results if the track comes from a proton. This basically results in a too low momentum which is additionally extenuated by energy loss of the proton trespassing detector layers closer to the interaction point (see figure 3.7). Nevertheless it could be shown that a selection of elastic events is feasible [48].
Although no preselection of tracks inside the Recoil detector was possible with method 3, kinematic fitting enables us to select the best true track candidate (see also section 4.2 and chapter 6).

4. Event selection

This chapter focusses on the selection of associated DVCS events. The selection was done using HANNA++, which is a C++ extension to HANNA and allows a comfortable selection of data on uDST level [49]. All events are selected from 06f1 and 07d1 productions. In comparison to the selection of elastic events, the selection of associated DVCS events is only slightly different.
In general the selection happens in four steps. First an event candidate is selected according to DVCS and DIS criteria. Second all Recoil tracks belonging to this event candidate and fulfilling the Recoil cuts become track candidates. In a third step a kinematic fit is done for each track candidate and the track with the lowest χ^2 is selected. Finally an event candidate gets accepted if the selected χ^2-value is below or above a certain threshold.
Upper χ^2-cuts are always chosen to have a fit probability greater than 1% which is 13.7 in the elastic case with four degrees of freedom and greater than 10 % which is 4.6 in the resonant case with two degrees of freedom for the kinematic fit (see subsection 4.2.2).
Only the important information about event selection will be presented. A full overview can be found in [46], [50] and [51]

4.1. Selection in the HERMES forward spectrometer

The selection of an event candidate is done using the following requirements in the forward spectrometer. This part of the selection is also important to count the number of total DIS events which can be used for cross-checking and most importantly for the normalization of the extracted asymmetry amplitudes.

4.1.1. General selection

- Bad bit pattern $0x7c1e1bdc$ was used for crosschecking with method 7. Since this bad bit requires a fully operational recoil detector which is not necessary for method 3, this was only chosen to make the results of both methods more comparable. The final results of the analysis presented in the thesis are selected with bad bit pattern $0x741e1bdc$ where no SSD is required.
- Forward spectrometer tracking: HTC is used in combination with the vertex finder, track topology *1-track-to-beam-vertex*, and flavor `_TF_HTC_UNBOUND_VERTEX_` (i.e. the beam line is not used as additional constraint). A cut of > 0.01 is applied to the track probability of the DIS lepton. No cut on the vertex probability is applied.
- Position of calorimeter in z coordinate: $z = 734$ cm for photons and leptons.
- Beam energy correction according to [52].

4.1.2. Selection of deep inelastic scattering (DIS)

- Trigger-21 has fired (main physics trigger which looks for a single track corresponding to a scattered beam particle): `smTrack.bTrigMask & 0x100000 == 0x100000`
- Lepton track with the highest momentum is selected as *leading lepton* if:
  - it is not a *short track*: `g1Track.iSelect & 0x0200`
  - it has the same charge as the beam lepton.
  - its energy is less than the beam energy.
  - it is a lepton according to PID2 + PID5 $>$ 2 without flux correction: `g1Track.rPID2 + g1.Track.rPID5 > 2`
- Inclusive kinematic variables calculated from the leading lepton:
  - $Q^2 > 1\text{GeV}^2$
  - $W^2 > 9\text{GeV}^2$
  - $\nu < 22\text{GeV}$
- Vertex cut: 5 cm $<$ *fVertZ* $<$ 20 cm
- Fiducial volume cut (FVC) on the DIS lepton: *Andy's FVC* and additional cuts on the track (x, y) position in the calorimeter:
  - Front field clamp: *fMaxXOff* $<$ 31 cm
  - Septum plate: *fMinYOff* $<$ 7 cm
  - Rear field clamp (front track): *fMaxYOff* $<$ 54 cm
  - Rear field clamp (long track): *fMaxXPos*$\leq$ 100 cm, *fMaxYPos*$\leq$ 54 cm
  - Calorimeter: *fMaxXCalo* $\leq$ 175 cm, 30 cm $\leq$ *fMaxYPos* $\leq$ 108 cm

4.1.3. Selection of deeply virtual Compton scattering (DVCS)

The restriction on the Mandelstam variable t_c^{DVCS} was removed to extent the kinematic range and the more appropriate constrained Mandelstam variable t_c^{Δ} is used instead (see equations 2.83 and 2.84). A DVCS event has the following requirements:

- Exactly one track is a DIS lepton.
- Exactly one untracked cluster in the calorimeter (with a signal in the calorimeter but no measured track information).

- Energy deposition in the calorimeter and the preshower: `smCluster.rE` > 8 GeV [51], `smCluster.rPulsPre` > 0.001 GeV. No corrections for the photon energy are applied.
- Calorimeter position of the untracked cluster: `smCluster.rX1Ew` < 125 cm, 33 cm $<$ `smCluster.rY1Ew` < 105 cm.
- Kinematic cuts on event level: $Q^2 < 10\text{GeV}^2$, $0.03 < x_B < 0.35$.
- Angle between virtual and real photons: 5 mrad $< \theta_{\gamma\gamma^*} < 70$ mrad [51].

4.2. Selection with the HERMES Recoil detector

For each event candidate which was selected in the forward spectrometer according to the cuts mentioned above, all reconstructed tracks in the Recoil detector are considered. The track which corresponds to the final state proton/π^+ is selected as described in the following section.

4.2.1. Recoil cuts

A track becomes a candidate if

- it was reconstructed using Method 3.
- the pion hypothesis exists for this track.
- it had positive energy.
- it was not measured in Recoil quadrant 2 (see 4.2.3 for further details).

4.2.2. Kinematic fitting

Now for each event we have a sample of one lepton track, one photon track and one to many candidates for a recoiling particle (namely proton or pion). For each candidate a kinematic fit is done under the assumption that lepton, photon and recoiling particle are the final state particles of an (associated) DVCS event.
The output of a the kinematic fit is a χ^2-value:

$$\chi^2_{kin} = \sum_{i=0}^{n-1} \frac{(par_i^{fit} - par_i^{meas})^2}{\sigma_i^2} \tag{4.1}$$

To take into account that the kinematic fit has to fulfill certain constraints the method of *penalty functions* is used:

$$\chi^2_{pen} = \sum_{i=0}^{n-1} \frac{(par_i^{fit} - par_i^{meas})^2}{\sigma_i^2} + T \cdot \sum_{j=0}^{m-1} \frac{C_j^2}{\sigma_{C,j}^2}. \tag{4.2}$$

Hereby T is a very large number (10^8), C_j is the j-th constraint (4.3-4.6 and 4.7-4.8) and $\sigma_{C,j}$ its derived error. As a result χ^2_{pen} can be minimized and fulfill the given constraints simultaneously.
For an elastic event four independent constraints are formulated from four-momentum conservation

$$C_0 = p_{x,l} + p_{x,\gamma} + p_{x,P} = 0, \tag{4.3}$$
$$C_1 = p_{y,l} + p_{y,\gamma} + p_{y,P} = 0, \tag{4.4}$$
$$C_2 = p_{z,l} + p_{z,\gamma} + p_{z,P} - p_{\text{beam}} = 0, \tag{4.5}$$
$$C_3 = E_l + E_\gamma + E_P - E_{\text{beam}} - m_P = 0. \tag{4.6}$$

Unlike in case of an elastic event not all final state particles are measured as the uncharged π^0/ neutron is missing. Instead of four constraints only two can be formulated corresponding to the mass of the Δ particle itself and the missing final state particle (π^0/ neutron):

$$C_0 = E^2_{miss,\Delta} - p^2_{x,miss,\Delta} - p^2_{y,miss,\Delta} - p^2_{z,miss,\Delta} - m^2_\Delta = 0, \tag{4.7}$$
$$C_1 = E^2_{miss,\pi/n} - p^2_{x,miss,\pi/n} - p^2_{y,miss,\pi/n} - p^2_{z,miss,\pi/n} - m^2_{\pi/n} = 0, \tag{4.8}$$

with

$$E_{miss,\Delta} = \sqrt{p^2_{\text{beam}} + m^2_l} + m_p - \sqrt{p^2_l + m^2_l} - E_\gamma, \tag{4.9}$$
$$p_{x,miss,\Delta} = p_{x,l} + p_{x,\gamma}, \tag{4.10}$$
$$p_{y,miss,\Delta} = p_{y,l} + p_{y,\gamma}, \tag{4.11}$$
$$p_{z,miss,\Delta} = p_{\text{beam}} - p_{z,l} - p_{z,\gamma}, \tag{4.12}$$

and

$$E_{miss,\pi^0/n} = \sqrt{p^2_{\text{beam}} + m^2_l} + m_p - \sqrt{p^2_{p,\pi^+} + m^2_{p,\pi^+}} - \sqrt{p^2_l + m^2_l} - E_\gamma, \tag{4.13}$$
$$p_{x,miss,\pi^0/n} = p_{x,p/\pi} + p_{x,l} + p_{x,\gamma}, \tag{4.14}$$
$$p_{y,miss,\pi^0/n} = p_{y,p/\pi} + p_{y,l} + p_{y,\gamma}, \tag{4.15}$$
$$p_{z,miss,\pi^0/n} = p_{\text{beam}} - p_{z,p/\pi^+} - p_{z,l} - p_{z,\gamma}. \tag{4.16}$$

Here p_{beam} is the momentum of the incoming beam-lepton, m_l the electron mass (511 keV), m_p the proton mass (938.272 MeV), p_l the momentum of the scattered lepton, E_γ the photon energy and $p_{x,l}$ the momentum of the scattered lepton in x direction. The remaining variables follow this naming scheme and the used masses are $m_{\pi^+} = 139.566$ MeV, $m_{\pi^0} = 134.9766$ MeV, $m_n = 939.565$ MeV, $m_\Delta = 1232$ MeV.

The fitted parameters are

$$\begin{aligned} par_0 &= \tan(p_{x,l}/p_{z,l}), \\ par_1 &= \tan(p_{y,l}/p_{z,l}), \\ par_2 &= 1/p_l, \\ par_3 &= \tan(p_{x,\gamma}/p_{z,\gamma}), \\ par_4 &= \tan(p_{y,\gamma}/p_{z,\gamma}), \\ par_5 &= 1/p_\gamma, \\ par_6 &= \Phi_P, \\ par_7 &= \Theta_P, \\ par_8 &= 1/(p_P \cdot \sin(\Theta_P)) = p_t. \end{aligned} \tag{4.17}$$

Correlations between kinematic parameters are not included, but these parameters are chosen to be the least correlated. For the recoiling proton transversal momentum, Φ and Θ are independent in good approximation. Photon energy and angles are not correlated because of the way they are reconstructed in the calorimeter. In case of the lepton, there is a correlation between momentum and the angle projection in horizontal plane (px/pz), but almost no correlation between momentum and the angle in the vertical plane (py/pz). A correlation matrix for photon reconstruction is missing as well. The situation for the lepton is similar [53].

4.2.3. Exclusion of events in the second Recoil quadrant

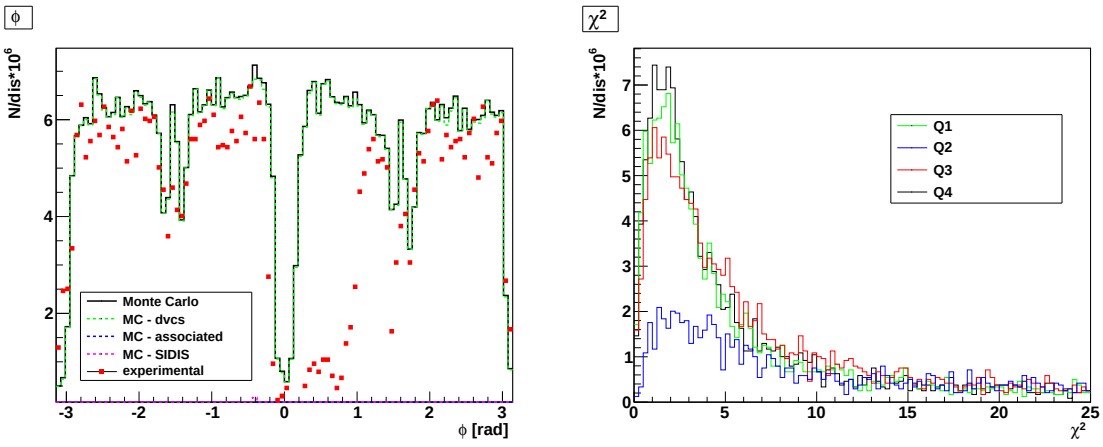

Figure 4.1.: The left plot shows the low statistics in the second quadrant (between 0 and $\frac{\pi}{2}$ rad) after applying the upper $\chi^2_{elastic}$-cut of 13.7. The plot of the $\chi^2_{elastic}$-distributions on the right indicates that events measured in this quadrant cannot be included without doubts.

A significant part of the outer stereo layer of the SFT in the second Recoil quadrant ($0 < \Phi < \frac{\pi}{2}$) had very low efficiency [54]. In case of method 3 these problematic fibers have been

unaccounted for in the Monte Carlo production (see figure 4.1(a)). A look at the $\chi^2_{elastic}$-distributions for each quadrant separately shows a clear discrepancy. Thus it is expected to have a much higher background in the interesting region, therefore event candidates in quadrant two are excluded from the analysis.

4.2.4. Track multiplicities for method 3

Because the track reconstruction for Recoil particles with method 3 doesn't have any degrees of freedom left, the track multiplicities in comparison to method 7 are much larger, which can be seen in the left plot of figure 4.2 (please refer to section 3.4 for further details). Furthermore ghost tracks could not be properly included in the Monte-Carlo as shown in the right plot of figure 4.2.

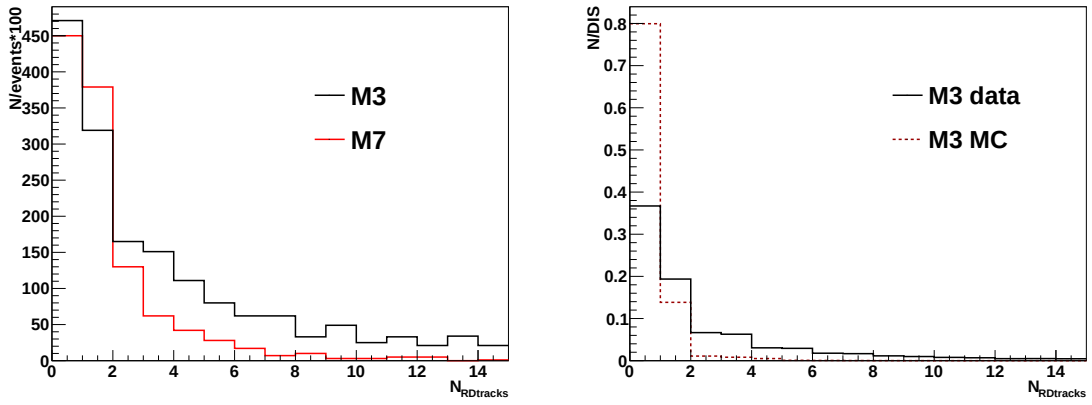

Figure 4.2.: Difference in track multiplicities N_{RD} between method 3 and method 7 (left) and disagreement for track multiplicities between data and Monte Carlo (right).

The consequences are illustrated in figure 4.3, where the $\chi^2_{ep\to e\gamma p\pi^0}$-distributions for different track multiplicities are drawn. The left plot visualizes the frequency of occurrence similar to figure 4.2. In the right plot each $N_{RDtracks}$-bin has been normalized to its overall number of events. The higher the track multiplicity, the more the χ^2-distribution is shifted to low values. This was negligible for kinematic fitting for $ep \to e\gamma p$, but because of the weaker constraints for the associated DVCS/BH hypotheses it is more likely that a ghost track fulfills the conditions best. This probability of course rises with the track multiplicity.
According to these observations only events with 5 Recoil tracks or less will be regarded whenever kinematic fitting with an associated DVCS/BH hypothesis ($ep \to e\gamma p\pi^0$ or $ep \to e\gamma n\pi^+$) is required.

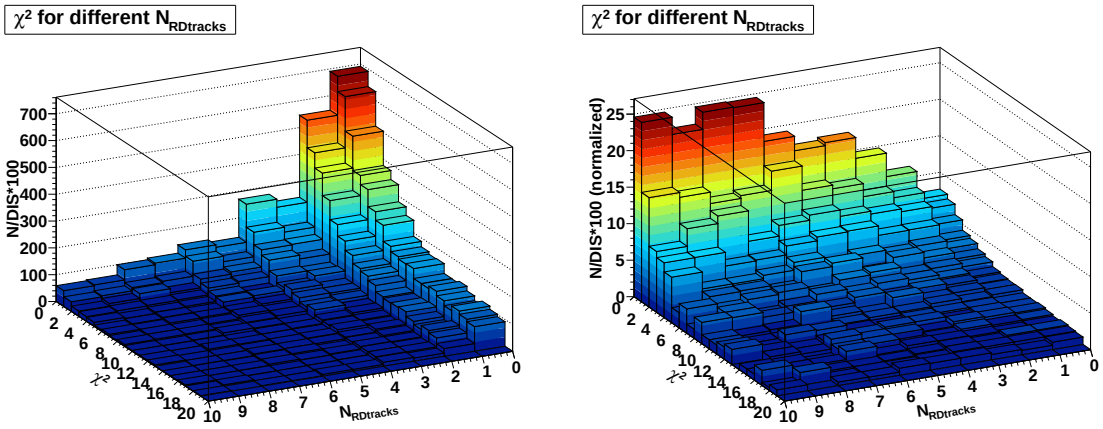

Figure 4.3.: The lego plot on the left illustrates the $\chi^2_{ep\to e\gamma p\pi^0}$-distributions for the different track multiplicities for real data. On the right the N_{RD} bins have been normalized to their overall number of events in order to accentuate the difference.

4.2.5. Final selection

After kinematic fitting for each event the track with the lowest χ^2-value is chosen. Depending on the analysis different additional cuts are applied for the final selection. A summary table can be found below (4.1).

4.2.5.1. Elastic sample ($ep \to e\gamma p$)

This sample is not relevant in the framework of this thesis but has been used for crosschecking. An event candidate is accepted if

- $\chi^2_{ep\to e\gamma p} < 13.7$.

4.2.5.2. Associated sample ($ep \to e\gamma\Delta^+$)

To have a statistically more significant sample to estimate the background of previous analysis such as [55] and [56], an associate sample was created using a lower χ^2 cut on the elastic hypothesis and a missing mass cut to reduce contribution by elastic DVCS/BH and SIDIS:

- $\chi^2_{ep\to e\gamma p} > 50$,
- $0.0\,\mathrm{GeV}^2 < M_x^2 < 3.5\,\mathrm{GeV}^2$.

4.2.5.3. Associated sample ($ep \to e\gamma p\pi^0$)

This sample aims at a high fraction of associated DVCS/BH events where the Δ^+ resonance decays into a proton and a π^0:

- $\chi^2_{ep\to e\gamma p\pi^0} < 4.6$,
- $\chi^2_{ep\to e\gamma p} > 50$,
- $p_p > 0.25$ GeV/c,

with p_p being the momentum of the measured recoiling particle.

4.2.5.4. Associated sample ($ep \to e\gamma n\pi^+$)

Related to the previous one, this sample aims at a high fraction of associated DVCS/BH events where the Δ^+ resonance decays into a neutron and a π^+:

- $\chi^2_{ep\to e\gamma n\pi^+} < 4.6$,
- $\chi^2_{ep\to e\gamma p} > 30$,
- $1 \text{ rad} < \theta_p < 2 \text{ rad}$,

with θ_p being the measured polar angle of the recoiling particle. Because the channel $ep \to e\gamma n\pi^+$ has rather characteristic kinematic distributions for its momentum and polar angle another "alternative" selection closely related to the combined associated selection (see 4.2.5.2) has been studied:

- $\chi^2_{ep\to e\gamma p} > 50$,
- $\theta_p > 1$ rad,
- $p_p < 0.5$ GeV/c,

For details on the determination of the kinematic- and lower $\chi^2_{ep\to e\gamma p}$-cuts please refer to chapter 6.

4.2.6. Comment on particle identification with the Recoil detector

Unlike the selection of the elastic processes, the selection of associated DVCS with method 7 was using Recoil PID in order to suppress cross contamination of the two channels and to reduce background in general. Originally Recoil PID was not foreseen for method 3 and has not been included in the final data production. Based on the results in [50] it would have been very desirable to have PID. This thesis is an approach to do the selection without particle identification.

	$\chi^2_{ep\to e\gamma p}$	$\chi^2_{ep\to e\gamma p\pi^0}$	$\chi^2_{ep\to e\gamma n\pi^+}$	M_x^2 [GeV^2	p_p [GeV/c]	θ_p [rad]
elastic	< 13.7	-	-	-	-	-
associated	> 50	-	-	$(0.0, 3.5)$	-	-
associated (M7)	> 100	-	-	< 3.5	-	-
associated p	> 50	< 4.6	-	-	> 0.25	-
associated n	> 30	-	< 4.6	-	-	$(1, 2)$
associated n (alt.)	> 50	-	-	$(0.0, 3.5)$	< 0.5	> 1

Table 4.1.: Summary of the cuts for the final selection as mentioned above. In addition the cuts for an associated reference sample with method 7 are included.

5. Data quality studies

5.1. Previous results

This analysis is one of the first to include data which was measured with the Recoil detector during the whole period of data taking in 2006 and 2007. Other studies using the Recoil detector only considered events starting with run 27934 in the year 2006 when both, silicon strip detector and scintillating fibre tracker were fully operational for the first time.

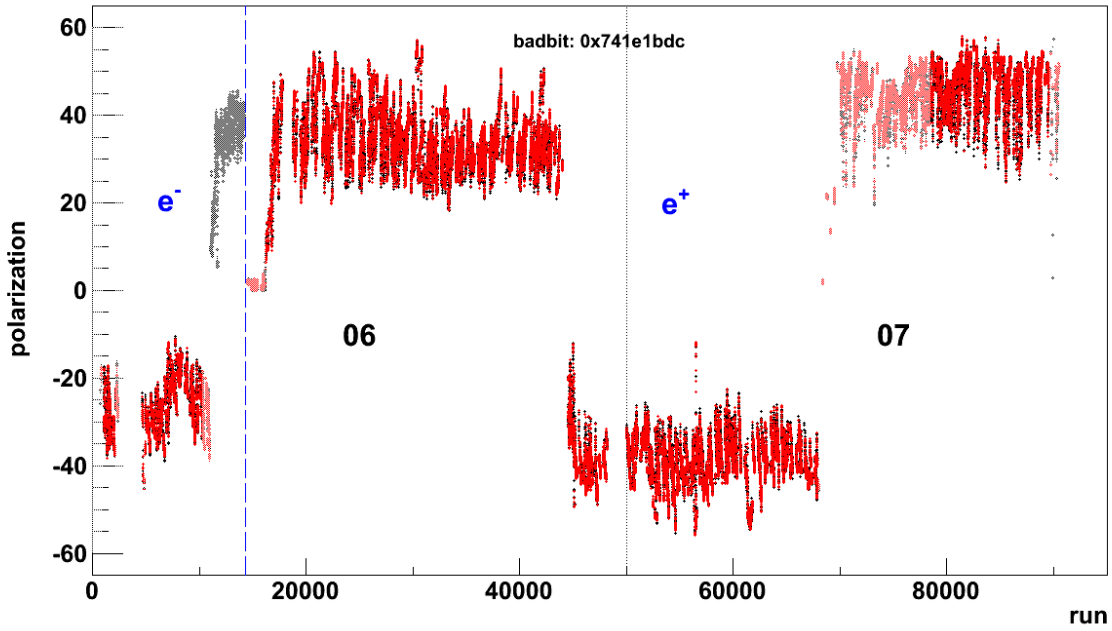

Figure 5.1.: Available data for the time period 2006 and 2007 requiring a fully operational forward spectrometer only (black dots) or measurements with the Recoil detector and method 3 (red dots). Brightened time periods have been excluded from the analysis requiring Recoil detector information. Between runs 11'000 and 14'000 the SFT had been almost completely removed due to an issue with the target cell.

Figure 5.1 illustrates the available data during the Recoil detector period. Black dots correspond to runs where tracks have been measured using the forward spectrometer and red dots to those which additionally were measured using the SFT of the Recoil detector. A run corresponds to a file of data which in general contains 560 Mbytes of information. Each run itself contains many bursts. A burst is defined as the 10 second time scale between two scaler events, which contain additional information by several counters. Burstlists are used during selection in order to exclude bad bursts or runs that have been previously identified by the data quality as bad from the selection. Applying the bad bit $0x741e1bdc$, which requires a fully operational SFT no regions without Recoil measurements but forward spectrometer only measurements should be left. Nevertheless a clear gap between runs 11'000 and 14'000

could be identified for the positively polarized electron beam period. Due to an issue with the target cell the Recoil detector had to be dismounted [57]. However a few stripes of the SFT were left and - although not recording useful data - they were in principal working properly and hence corresponding bursts were not marked as bad [58].

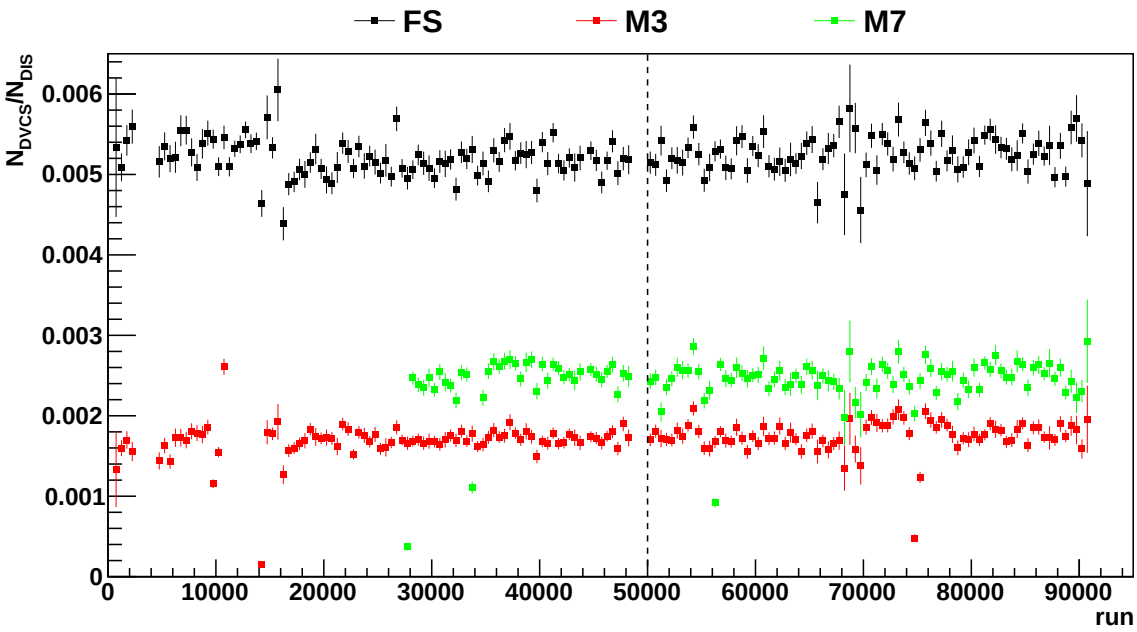

Figure 5.2.: The plots shows the ratios of DVCS/DIS for events taken during 2006 and 2007. The drop in the ratio is due to limited acceptance and efficiency.

5.2. Additional studies

Besides this gap more significant intervals without any Recoil measurement could be identified and excluded by manually reviewing the recorded runs. The absence of positively polarized electron beam data is not only reducing the statistics for beam charge asymmetry studies but restricts the analysis concerning simultaneous extraction of beam charge and beam spin asymmetries as well.

Special attention is drawn to the ratio DVCS/DIS. This is necessary since the number of DIS events is used for the normalization of our samples (equations 2.68 and 2.71). A significant drop or rise in this ratio would indicate a malfunction in either, the spectrometer or more likely the SFT. Such a drop can be seen around run 75'000[1] for the M3/DIS ratio in 5.2. This is the ratio we are interested in because the analysis is based on this method to select DVCS events. Figure 5.3 shows the ratio and already indicates the excluded regions which are summarized in table 5.1. Besides the drop around run 75'000 one can see a small rise between runs 68'000 and 78'500 which significantly deviates from the mean value. A visual

[1] here the run numbers from the 2007 data starts with 50'001 instead of 1

crosscheck with Recoil offline data quality plots [59] confirmed this impression. There one can see a correlation between the positron beam fill pattern and the energy deposition of pions in the inner and outer SFT. Because this is an undesired behavior all runs in this time period are excluded from the analysis. This not as problematic since only positively polarized positron beam data is concerned.

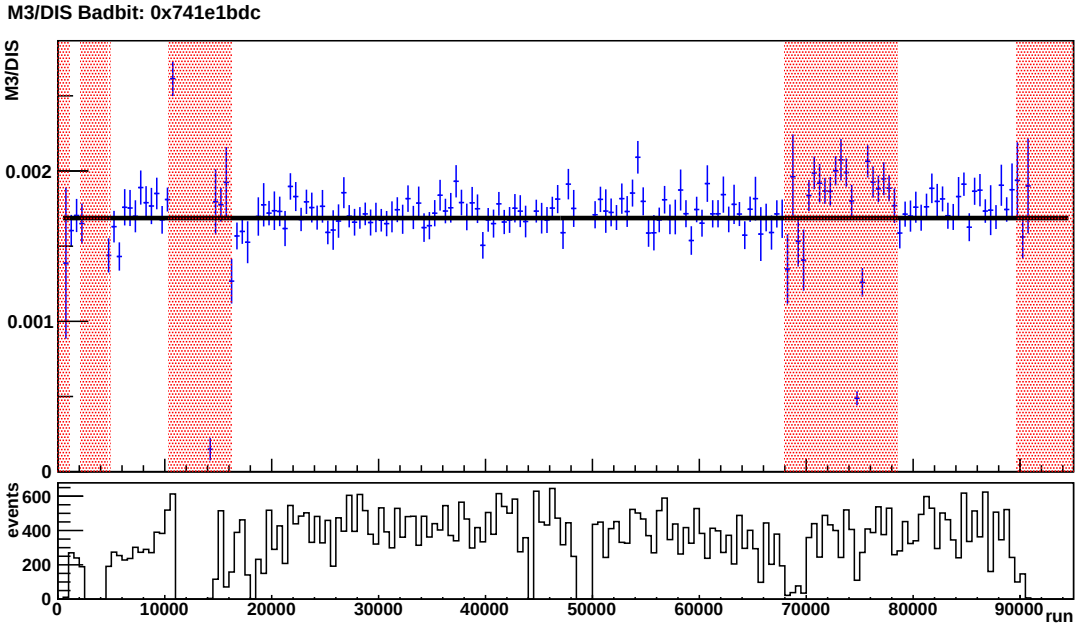

Figure 5.3.: The upper plot shows the DVCS/DIS ratio for method 3 and the exluded runs (red stripes). The region between 68′000 and 78′500 shows a significant deviation from the mean value. The lower histogram displays the number of recorded events for each bin.

Besides the M3/DIS ratio, the behavior of the measured kinematic variables against time/ runs has been plotted and checked for inconsistencies (in figure A.1 this has been done for the track multiplicities). No significant deviations can be observed which would have led to additional exclusion of runs. One can also see that other large deviations can be understood by limited statistics in the corresponding run-bin.

In figure 5.4 the M3/DIS ratio is plotted for the different Recoil quadrants. Besides the dark band in quadrant 2 ($0 < \Phi < \frac{\pi}{2}$) no conspicuous regions can be identified. The quadrants have been further divided in order to check for inconsistencies within a quadrant but again no conspicuous regions could be found (see figure A.2 in the appendix). Other large deviations in the color are due to low statistics in the corresponding run-bin as indicated by the lower histogram.

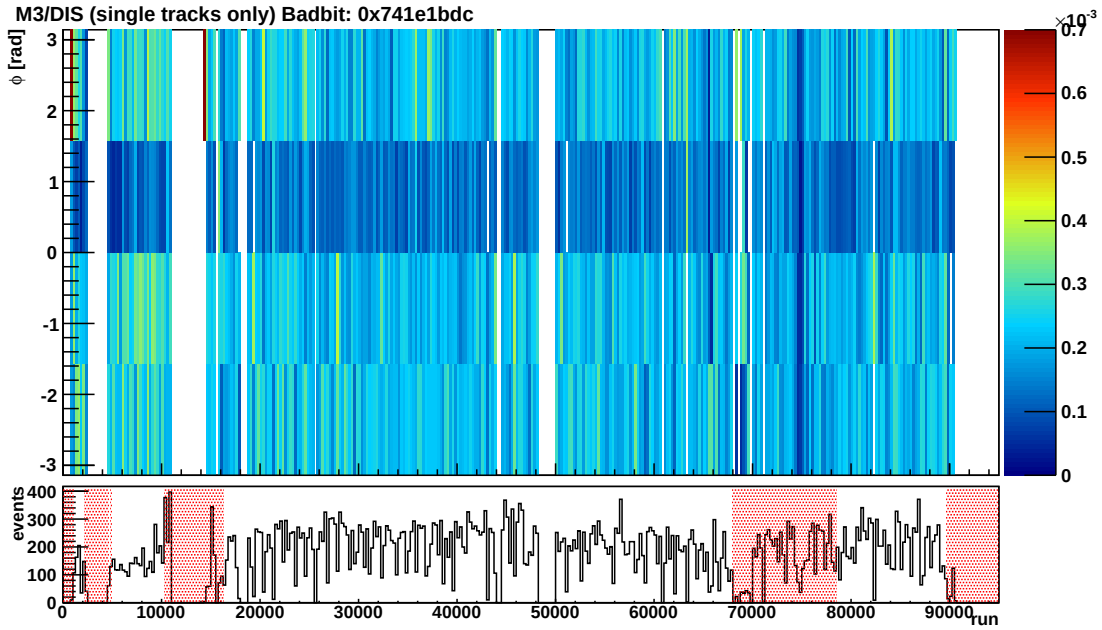

Figure 5.4.: The upper plot shows the DVCS/DIS ratio for method 3 in the different Recoil quadrants. In the second quadrant ($0 < \Phi < \frac{\pi}{2}$) one can clearly see the missing efficieny as it has been described in 4.2.3. The lower histogram displays the number of recorded events for each bin and marks the excluded regions.

excluded runs			reason
700	-	1'040	bad energy deposition in DQ plots [59]
2'154	-	4'360	bad energy deposition in DQ plots [59]
10'305	-	16'250	unmounted Recoil detector due to target cell issue [57] insufficient polarization for early positron data bad energy deposition in DQ plots [59]
68'000	-	78'500	periodical change in tracks/DIS and bad energy deposition correlated with positron beam fill pattern bad M3/DIS ratio
89'650	-	90'100	bad M3/DIS ratio partially not covered by DQ plots [59]

Table 5.1.: The table summarizes the additionally excluded regions for the 2006 and 2007 data taking. Runs from 2007 start with number 50'001.

6. Monte-Carlo studies

For the Monte-Carlo studies two different HERMES Monte-Carlo productions were used. The (associated) DVCS/BH events were taken from the production [054] using the *gmcDVCS* generator with 4 million events. The semi-inclusive deep inelastic scattering background (SIDIS) came from the production [055] using the *disNG* generator with 50 million events. Both productions are based on the 2006 geometry, have a proton target, HRC, HTC and XTC available for tracking and Recoil detector information is included [60].

6.1. Summary of previous studies to select elastic events

In previous studies such as [48] and [61], it was shown that the selection of an elastic sample with a purity above 99 % was feasible with method 3. In this connection the resolution of the kinematic variables measured by the Recoil detector had been estimated.

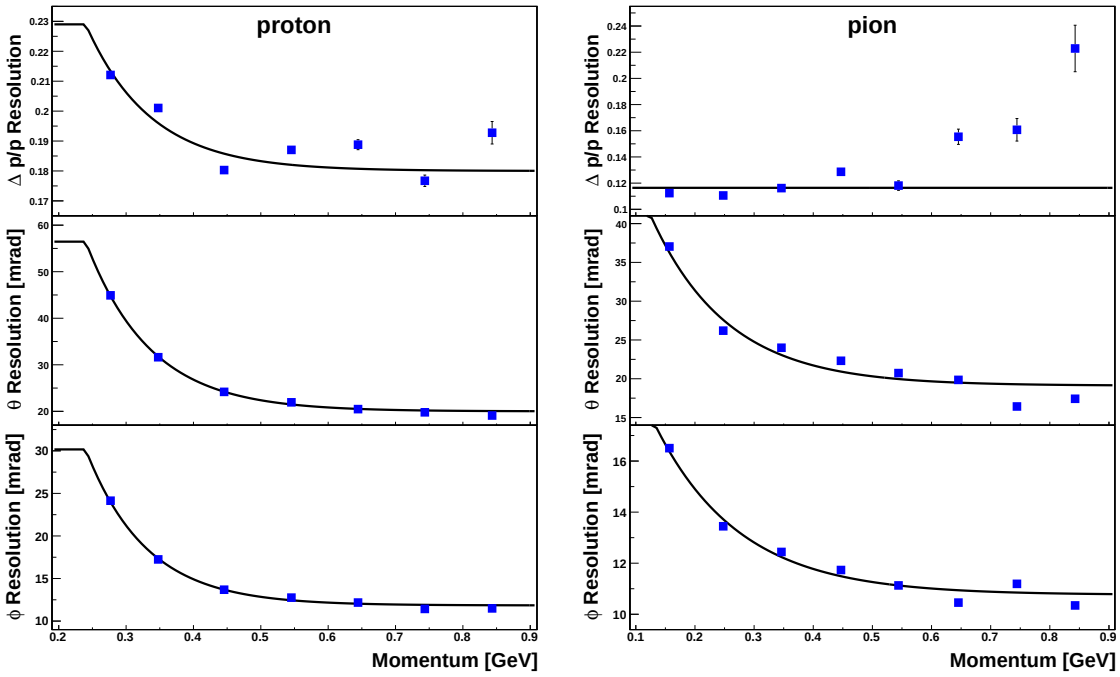

Figure 6.1.: The left (right) plot shows the resolution of the proton's (pion's) kinematic variables reconstructed with method 3. The solid line is the resulting parametrization. The deviations for high momentum pions can be neglected (see figure 3.7).

The momentum dependent parametrization was done using Monte-Carlo data and comparing the output of the track reconstruction with the original kinematics. Therefore for each Recoil parameter the difference $par_{i,meas} - par_{i,true}$ ($i = \{6,7,8\}$, see equations 4.17) has been histogrammed. The resulting distributions were Gaussianlike and their standard deviations

were used as a first estimate of the resolution. Afterwards this was parameterized according to figure 6.1. Figure 6.2 shows the resolution of the transverse momentum p_t for different momentum bins after an optimization (see section 6.2).

In case of the proton resolution a constant term has to be added (left plots in figure 6.1). At first an exponential function had been used to fit the data points. When the Monte-Carlo data was first compared to real data an unphysical bump below 0.25 GeV was visible. Because of the absorption in the sublayers of the detector no protons were expected to be measured. Because many of the concerned events were also available for method 7 it could be shown that those tracks did not belong to pions. A systematic study showed that due to high track-multiplicities in case of method 3 and an overestimated resolution for $p < 0.25$ GeV, ghost tracks were accidentally chosen by the kinematic fitting. Hence a constant term was added for low momenta which resulted in a good agreement for Monte Carlo and real data.

The same procedure was repeated in order to estimate the pion resolution which can be found in the right plot of figure 6.1. The resolution of pions' transversal momentum is flat in good approximation.

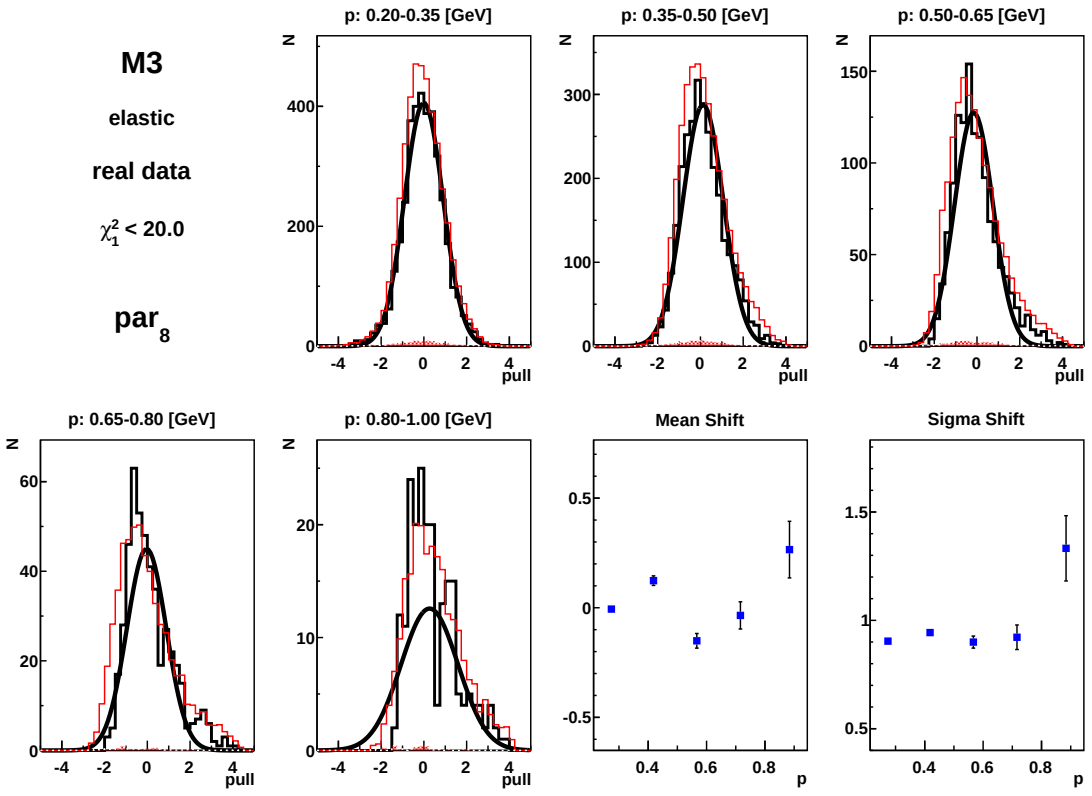

Figure 6.2.: Illustration of the optimization of kinematic fitting. The histrograms show the resolution for different kinematic bins. In this example the transverse momentum of the recoiling particle (par_8) is investigated. The black histograms represent real data, whereas the red histograms repesent Monte Carlo data. The two graphs on the bottom right summarize the mean and standard deviations of the Gaussian fits to the histograms.

6.2. Optimization of kinematic fitting

The good performance of selecting elastic events using kinematic fitting with method 3 is due to the relatively high number in degrees of freedom and the high frequency of occurrence of elastic events. In contrast to the elastic scenario where one mainly wants to reduce the background for an a priori dominant signal, one's goal is the selection of the background process itself when doing kinematic fitting for associated events. Additionally only the charged decay product of the Δ resonance can be measured and the uncharged particle remains undetected, which bisects the degrees of freedom for the kinematic fit to 2 (4.7 and 4.8). Because two decay channels ($\Delta^+ \to p\pi^0$ and $\Delta^+ \to n\pi^+$) with different kinematics have to be considered, statistics are much lower and cross contamination of the decay channels has to be avoided as much as possible.

As mentioned before, particle identification for method 3 is not available, which complicates the separation of the decay channels. Since kinematic fitting is only way of quantifying the probability of a track coming from either a proton or a pion, the optimization of kinematic fitting with method 3 was a major subject.

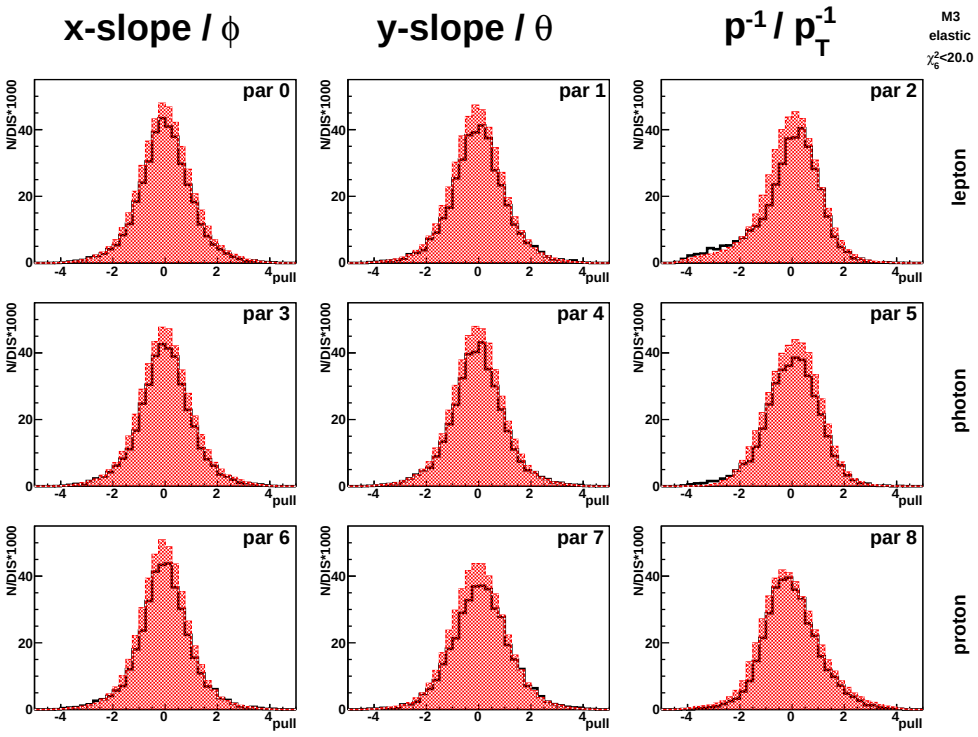

Figure 6.3.: Pull distributions for real data (black histograms) and Monte Carlo (red histograms) for kinematic fitting under the hypothesis $ep \to e\gamma p$. The filled area represents real elastic events in the Monte Carlo.

This optimization was carried out for Monte-Carlo and real data to receive a good agreement.

Two main issues had to be improved:

- Since the parametrization was solely based on Monte-Carlo data the resolution for real data can be different.
- In case of method 3 the track reconstruction is done using the pion hypothesis. Together with the energy loss of protons when trespassing sublayers of the detector, the reconstructed momentum is too low (see section 3.4).

Whereas the bias in the momentum reconstruction can be corrected for Monte-Carlo, it remains hidden for real data. In this regard pull distributions are a common tool to correct for the bias and the resolution in the context of kinematic fitting [62]. In figures 6.3, 6.4 and 6.5 one can see the pull distribution for the relevant processes. The pulls are defined as

$$pull_i = \frac{par_i^{fit} - par_i^{meas}}{\sqrt{\sigma_i^2(par_i^{meas}) - \sigma_i^2(par_i^{fit})}} \tag{6.1}$$

and are available as an output for every track's kinematic fit.
If it is presumed that the data is Gaussian, pulls are Gaussian themselves and contain information on the bias, which is visible through a shift of the mean of the distribution, and also information on the resolution, which results in a too small (large) pull width if the resolution is too high (low). In order to optimize kinematic fitting, pull distributions for different kinematic bins for all kinematic variables had been investigated. Here the mean and width of each kinematic bin was plotted into a graph and then this graph was fitted by a polynomial of low degree. The result of the fit for every parameter was afterwards implemented in the kinematic fitting routine. In order to correct for the bias, the input data was shifted and the resolution corrected. In a last step the kinematic fitting was repeated with the new parametrization and offset. This procedure was repeated multiple times until the pulls were roughly normal distributed around 0. This automatically led to a good agreement between Monte-Carlo and real data (figure 6.3). Figure 6.2 shows the final plot in case of the proton's transversal momentum for above procedure (additional plots can be found appendix: A.3, A.4).
In figure 6.4 the pull distributions under the hypothesis $ep \to e\gamma p\pi^0$ are shown. The kinematic fit is using the same parametrization and corrections as the fit under the elastic hypothesis. Nevertheless the pulls are not Gaussian, which is mainly caused by the large background giving rise to the tails. Sharp peaks around 0 are caused by bad track selection due to high multiplicities in the Recoil detector.
A similar behavior can be found for the pulls in figure 6.5 that correspond to fits under the hypothesis $ep \to e\gamma n\pi^+$. Due to very limited statistics for real data a momentum dependent optimization is not possible. However since the track reconstruction is based on a pion hypothesis, no problematic bias should exist.

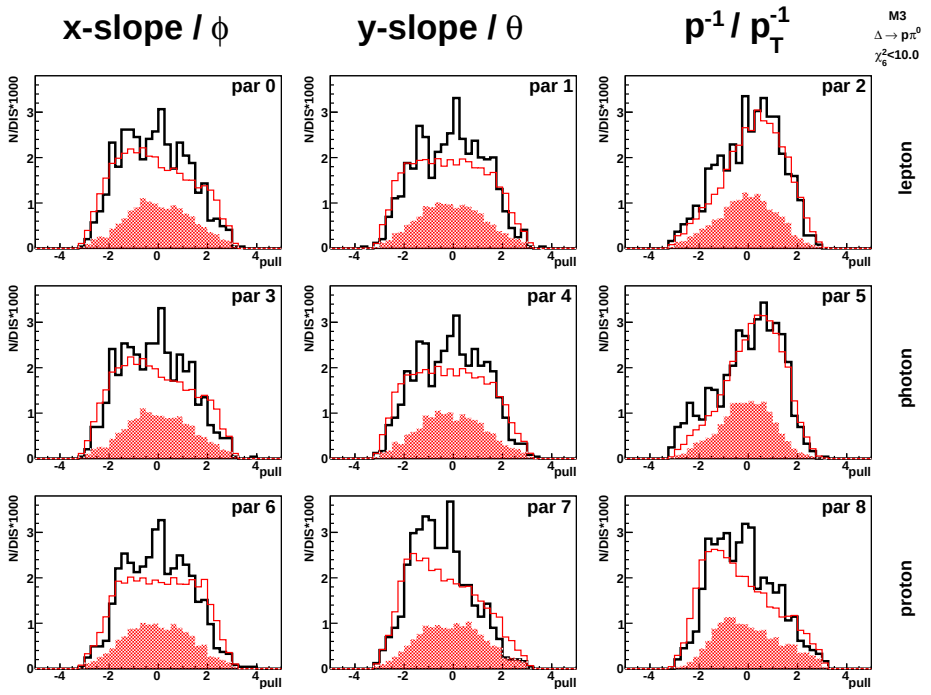

Figure 6.4.: Pull distributions for real data (black histograms) and Monte Carlo (red histograms) for kinematic fitting under the hypothesis $ep \to e\gamma p\pi^0$ after all cuts have been applied. The filled area represents real signal events in the Monte Carlo.

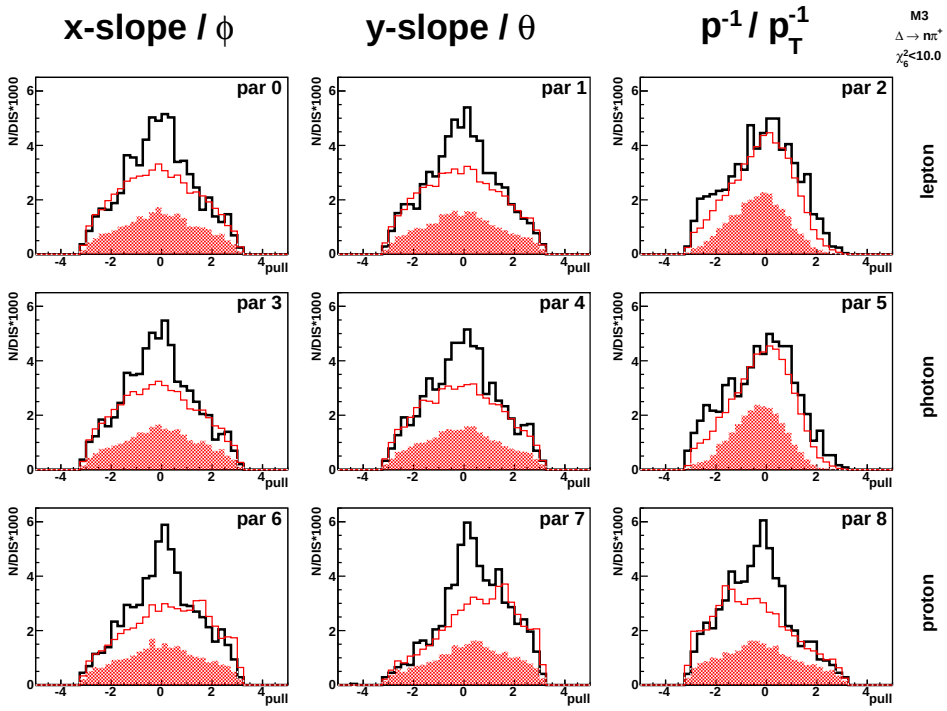

Figure 6.5.: Pull distributions for real data (black histograms) and Monte Carlo (red histograms) for kinematic fitting under the hypothesis $ep \to e\gamma n\pi^+$ after all cuts have been applied. The filled area represents real signal events in the Monte Carlo.

6.3. Study of the selection of resonant events

6.3.1. Associated events $ep \to e\gamma\Delta^+$ (combined)

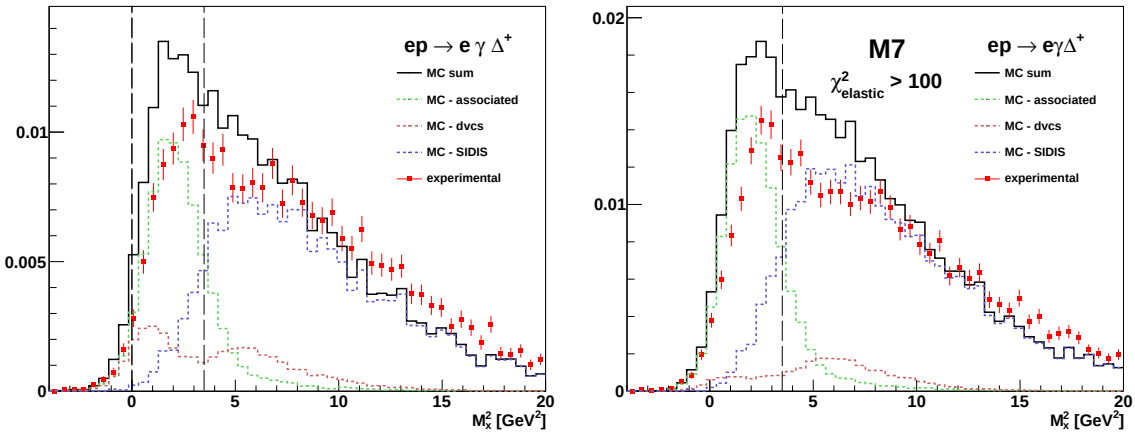

Figure 6.6.: The histograms show the missing mass distribution after a lower $\chi^2_{ep\to e\gamma p}$ of 50 (100 in case of method 7) has been applied. Dashed and solid lines correspond to Monte-Carlo, the markers with error bars are from real data. The dashed vertical lines indicate the position(s) of the missing-mass cut. As long as not indicated otherwise the y-axis corresponds to the entries normalized to the total measured DIS events times 1000.

In order to achieve a high-statistics event sample a new approach was tested. Here the final selection is done without kinematic fitting for any of the associated DVCS/BH hypotheses but using a lower cut on the elastic kinematic fitting. This lower cut aims at excluding elastic events from the analysis. The contribution of SIDIS events is suppressed by introducing a missing mass cut. The shift in the missing-mass peak position between real data and Monte-Carlo is a general issue. Systematic studies indicate that the shift in the missing-mass peak position is due to electromagnetic-calorimeter calibration issues associated with the measurement of photon energies, which do not enter the calculation of kinematic quantities other than the missing mass [63].

This selection doesn't allow a separation of the Δ's decay processes why it will be referred to as combined associated DVCS. Nevertheless it is useful to estimate the contamination of associated processes for previous BCA analyses, where this background remained unregarded. The right plot in figure 6.6 contains the missing-mass spectrum for method 7 with a lower $\chi^2_{ep\to e\gamma p}$-cut of 100. The method 7 analysis was carried out in order to get a reference sample for this process. In the left plot of 6.6 the missing-mass spectrum for method 3 is shown. Here the lower $\chi^2_{ep\to e\gamma p}$-cut is only 50, which was chosen as a trade-off between purity and efficiency (see also figure 6.7). The fractions of the contributing processes for the relevant kinematic variables can be found in figure 6.8 and table 6.1. Figure 6.8 also contains the comparison between real data and Monte-Carlo.

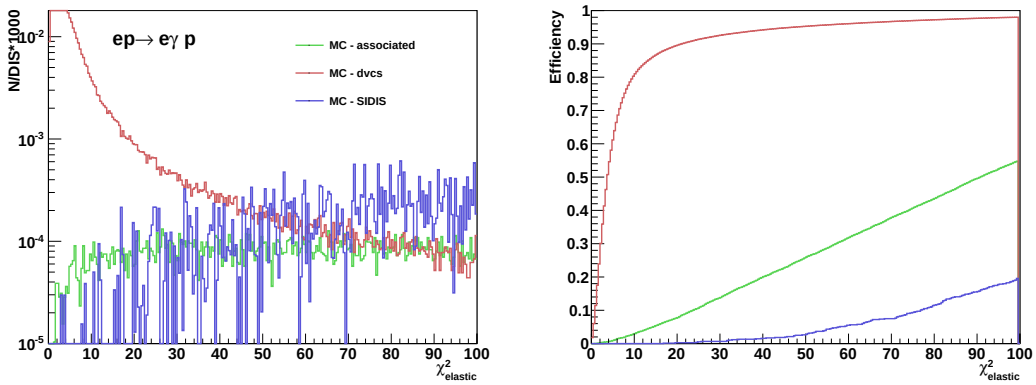

Figure 6.7.: χ^2-distribution of the $ep \rightarrow e\gamma p$ hypothesis (left) and the corresponding efficiencies (right). Shown processes are elastic DVCS/BH (red), associated DVCS/BH (green) and SIDIS (blue).

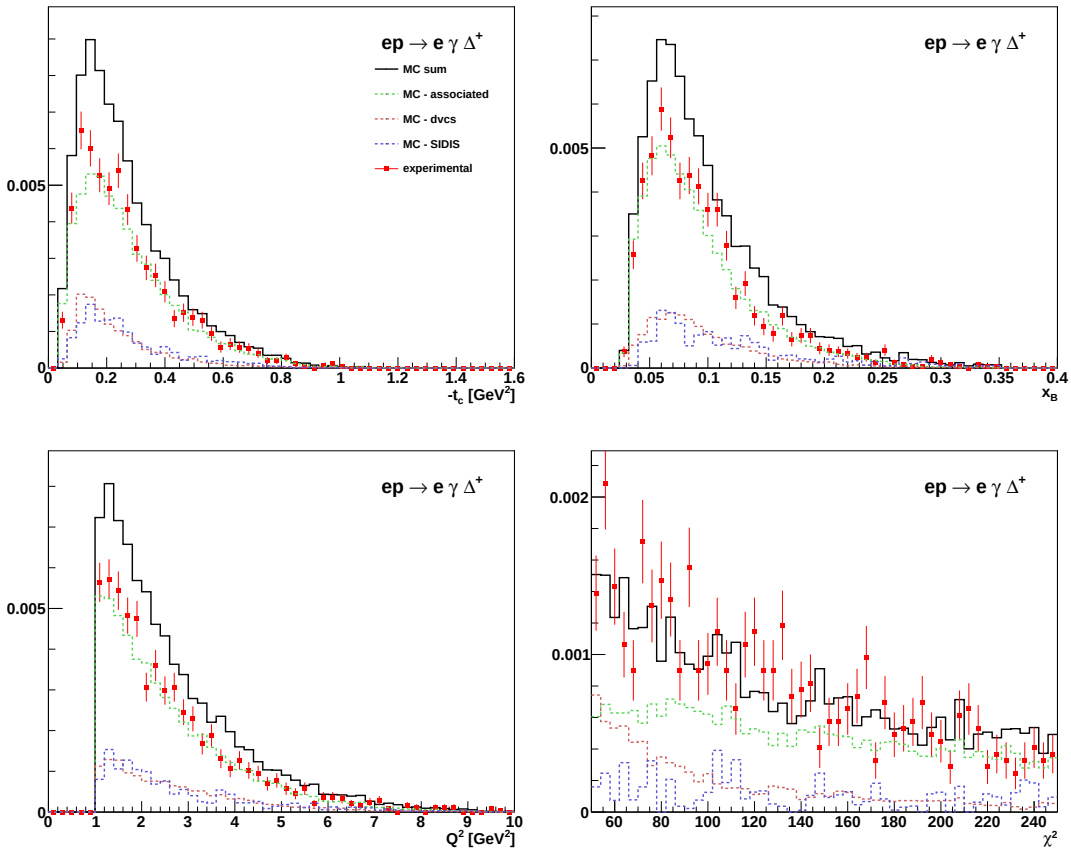

Figure 6.8.: Distributions of different channels for the kinematic variables t_c^{Δ} (top left), x_B (top right), Q^2 (bottom left) and $\chi^2_{ep\rightarrow e\gamma p}$. Shown processes are elastic DVCS/BH (red), associated DVCS/BH (green) and SIDIS (blue).

$ep \to e\gamma\Delta^+$		associated	elastic	SIDIS
overall		66.5 ± 1.0	16.7 ± 0.3	16.8 ± 1.2
t_c	0.00- 0.17	63.7 ± 1.7	20.8 ± 0.7	15.6 ± 2.3
	0.17- 0.30	65.0 ± 1.7	16.5 ± 0.6	18.5 ± 2.2
	0.30- 0.50	71.6 ± 1.7	13.4 ± 0.5	15.0 ± 1.7
	0.50- 1.50	69.5 ± 2.4	11.4 ± 0.7	19.2 ± 2.3
x_B	0.03- 0.07	71.9 ± 1.7	15.7 ± 0.5	12.4 ± 2.0
	0.07- 0.10	68.1 ± 1.9	18.4 ± 0.7	13.5 ± 2.3
	0.10- 0.15	63.4 ± 1.9	17.1 ± 0.7	19.6 ± 2.5
	0.15- 0.35	55.6 ± 1.9	15.5 ± 0.7	28.9 ± 2.6
Q^2	1.00- 1.50	69.1 ± 2.4	16.4 ± 0.7	14.5 ± 3.0
	1.50- 2.30	67.1 ± 1.9	15.4 ± 0.6	17.5 ± 2.4
	2.30- 3.50	67.2 ± 1.7	17.7 ± 0.6	15.2 ± 1.9
	3.50- 10.0	62.5 ± 1.5	17.6 ± 0.6	19.9 ± 1.6

Table 6.1.: Fractional contributions for the $ep \to e\gamma\Delta^+$ selection, which were used for the background correction.

6.3.2. Associated events $ep \to e\gamma p\pi^0$

The selection of event-type $ep \to e\gamma p\pi^0$ follows the standard technique for associated events [50]. In the upper plots of figure 6.10 the χ^2-distributions and efficiencies under the $ep \to e\gamma p\pi^0$ hypothesis are plotted. In contrast to the elastic selection, the contamination at low $\chi^2_{ep\to e\gamma p\pi^0}$ is large. To have a fit probability of at least 10 %, an upper cut of 4.6 is chosen. Each track is additionally fitted under the $ep \to e\gamma p$ hypothesis and a lower cut of 50 on its χ^2-value is applied in order to remove elastic background (lower part of figure 6.10). In the method 7 analysis the χ^2-distribution for tracks of the associated channel, which were selected under the $ep \to e\gamma p\pi^0$ hypothesis, is almost flat and a higher $ep \to e\gamma p$ of 100 was chosen.

At first a large discrepancy between real data and Monte-Carlo had been observed. Looking at the momentum distribution a peak in real data for events with a Recoil momentum below 0.25 GeV indicates miss-selection due to high track multiplicities (left plot of figure 6.9). According to 4.2.4 events with more than 5 tracks were excluded from the analysis (right plot of figure 6.9). A lower momentum cut of $p > 0.25GeV$ was introduced, too. Although the agreement between Monte-Carlo and real data could be improved the number of real data events, which is artificially reduced due to the multiplicity cut, still exceeds Monte-Carlo.

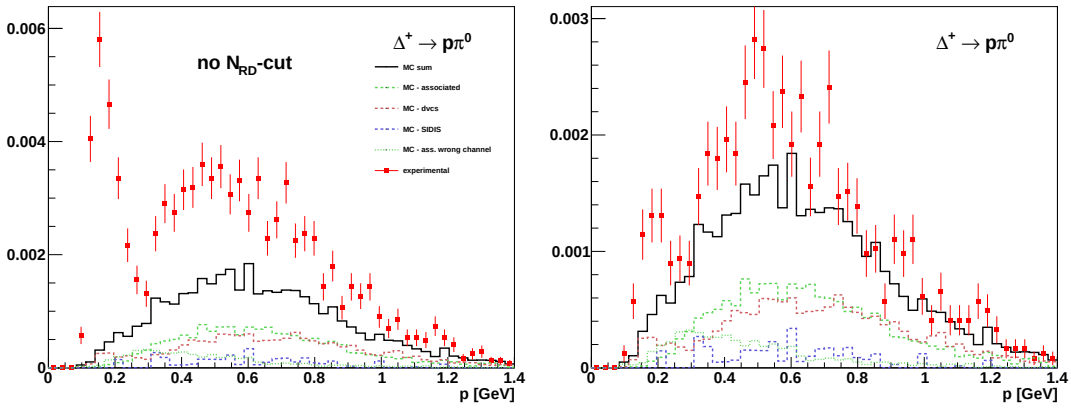

Figure 6.9.: The situation after all kinematic and χ^2 cuts have been applied (left) and the distribution if events with a Recoil track multiplicity of less than 6 is required (right).

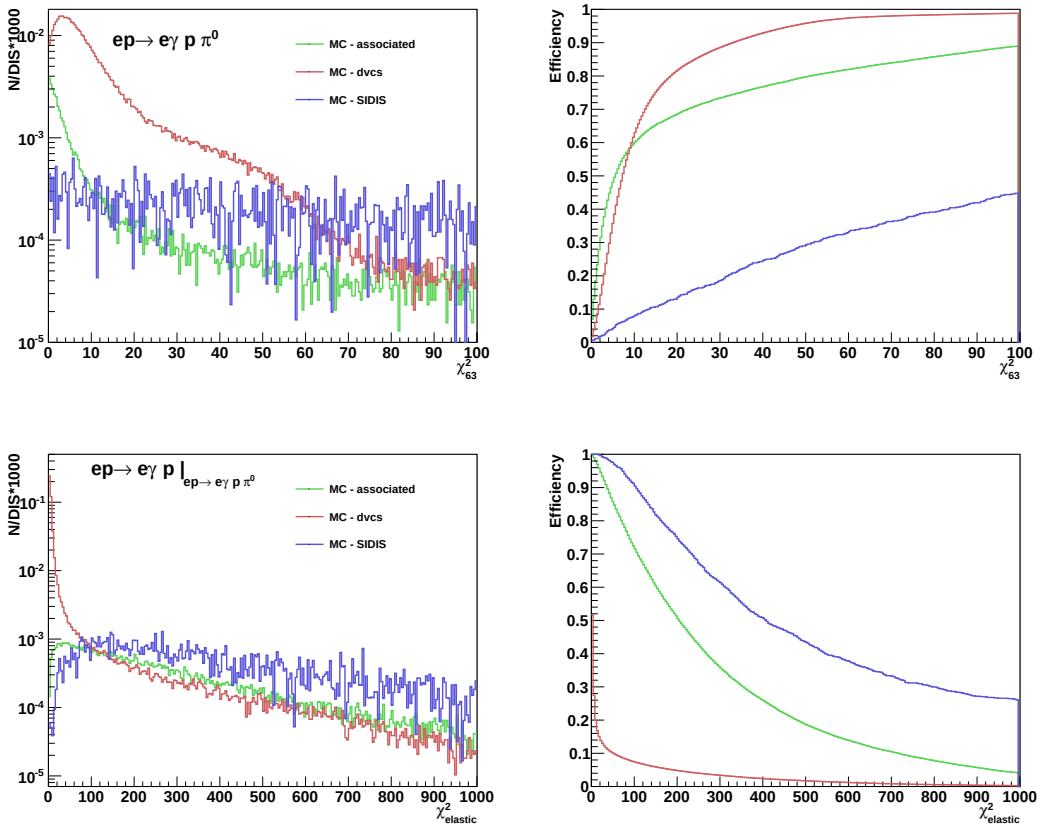

Figure 6.10.: χ^2 distributions without the lower $\chi^2_{ep\rightarrow e\gamma p}$-cut of the $ep \rightarrow e\gamma p\pi^0$ hypothesis (top left) and the corresponding efficiencies (top right). $\chi^2_{ep\rightarrow e\gamma p}$ distributions (bottom left) and corresponding efficiency distributions for the tracks selected under the $ep \rightarrow e\gamma p\pi^0$ hypothesis but without an upper χ^2-cut (bottom right). Shown processes are elastic DVCS/BH (red), associated DVCS/BH (green) and SIDIS (blue).

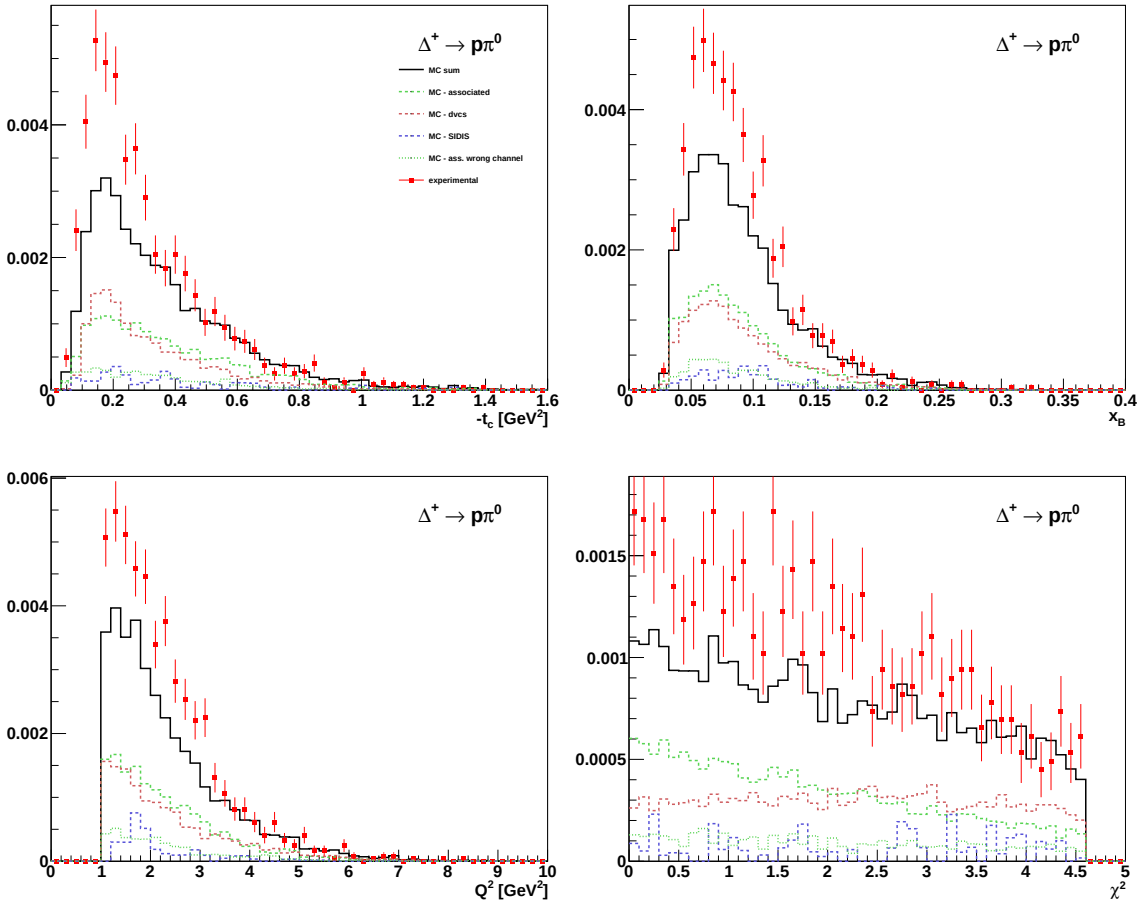

Figure 6.11.: Distributions of different channels for the kinematic variables t_c^{Δ} (top left), x_B (top right), Q^2 (bottom left) and $\chi^2_{ep\to e\gamma p\pi^0}$. Shown processes are elastic DVCS/BH (red), associated DVCS/BH (green) and SIDIS (blue).

In figure 6.11 and table 6.2 the fractions for the relevant kinematic variables can be found. An important fraction is the contribution of the decay channel $\Delta^+ \to n\pi^+$ which is quantified in table A.1. A way to reasonably treat this in a systematic error has yet to be found. According to Monte-Carlo, the rejection factor for $ep \to e\gamma p\pi^0$ with respect to the overall number of associated events is about 5. This fraction has to be as small as possible because no independent measurement for the background correction is available. In the lower right plot of figure 6.11, its χ^2-distribution appears to be flat, which means that kinematic fitting is in principle able to separate the channels. Nevertheless the separation could be very much improved, if Recoil PID was available.

$ep \to e\gamma p\pi^0$		associated	elastic	SIDIS
overall		54.1 ± 1.0	37.5 ± 0.8	8.4 ± 1.3
t_c	0.00- 0.17	53.2 ± 2.1	40.5 ± 1.7	6.3 ± 2.4
	0.17- 0.30	48.2 ± 1.8	42.7 ± 1.7	9.2 ± 2.7
	0.30- 0.50	55.4 ± 2.0	35.9 ± 1.4	8.7 ± 2.5
	0.50- 1.50	61.4 ± 2.3	29.7 ± 1.3	8.9 ± 2.3
x_B	0.03- 0.07	56.5 ± 1.6	37.1 ± 1.2	6.4 ± 1.7
	0.07- 0.10	54.5 ± 2.1	35.9 ± 1.5	9.6 ± 2.8
	0.10- 0.15	52.7 ± 2.2	37.1 ± 1.6	10.1 ± 2.9
	0.15- 0.35	47.9 ± 2.6	44.0 ± 2.4	8.1 ± 2.8
Q^2	1.00- 1.50	54.7 ± 1.9	40.3 ± 1.5	5.0 ± 2.2
	1.50- 2.30	52.2 ± 2.0	34.3 ± 1.4	13.5 ± 3.0
	2.30- 3.50	58.3 ± 1.9	35.7 ± 1.3	6.0 ± 1.7
	3.50-10.0	51.0 ± 2.1	42.3 ± 1.8	6.7 ± 1.9

Table 6.2.: Fractional contributions for the $ep \to e\gamma p\pi^0$ selection, which were used for the background correction.

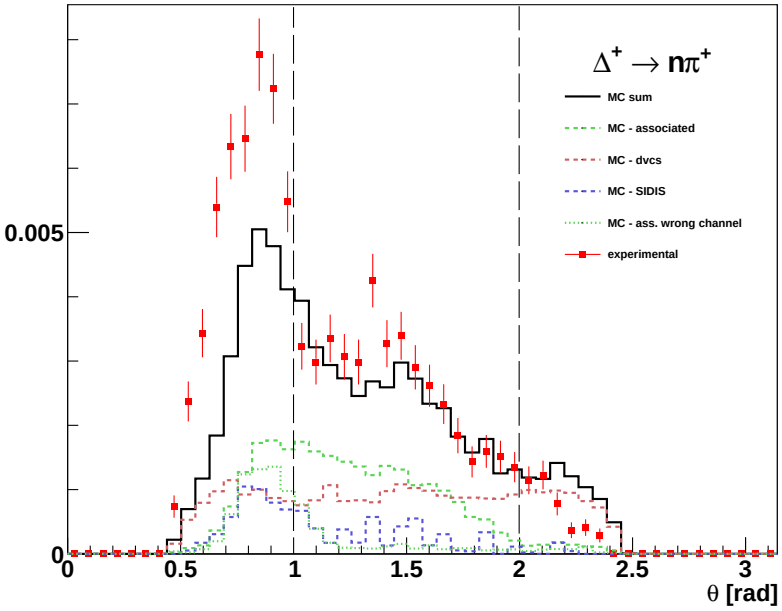

Figure 6.12.: Polar angle distribution of $ep \to e\gamma n\pi^+$ events. The dahsed lines represent the applied upper and lower cut.

6.3.3. Associated events $ep \to e\gamma n\pi^+$

A very similar selection to 6.3.2 was carried out for $ep \to e\gamma n\pi^+$. Besides this "traditional" way of selecting associated events, another alternative way will be introduced. It was found that the $\Delta \to n\pi^+$ channel has rather characteristic kinematics in the combined associated selection. Although the cuts narrow the kinematic dependence, a relatively pure sample with much higher statistics can be selected.

Traditional selection

In figure 6.13 one can see that the situation in terms of upper and lower χ^2-cuts is similar to the hypothesis $ep \to e\gamma p\pi^0$. Due to very low statistics a lower cut on the elastic hypothesis of only 30 was chosen. In case of method 7 this cut could even be pushed down to 5, since PID removes almost all background coming from the elastic DVCS/BH process. The polar angle distributions in figure 6.12 reveals interesting information about the selection itself. Whereas the agreement between 1 rad and 2 rad for real data and Monte-Carlo is very good, it deviates for the regions above and below. The enhancement for $\theta < 1$ is an indicator that elastic events or protons from $\Delta \to p\pi^0$ are more likely to pass the selection than expected from Monte-Carlo. In addition the elastic contribution is rather flat and covers almost the whole measured range. This shows that even in the Monte-Carlo many ghost tracks have been wrongly selected as $ep \to e\gamma n\pi^+$ events, because theoretically one wouldn't expect any elastic protons above 1.3 rad (see section 3.4).
Plots in figure 6.14 show Monte-Carlo and real data for the relevant kinematic variables and χ^2. Due to the very strict cut on the polar angle, the agreement is much better than in the previous analysis. Same is true for the purity and the cross-contamination by events coming from $ep \to e\gamma p\pi^0$ as can be see in tables 6.3 and A.2. Nevertheless the selection with method 3 is not capable of competing with the results using method 7, where purities above 75 % were reached [50].

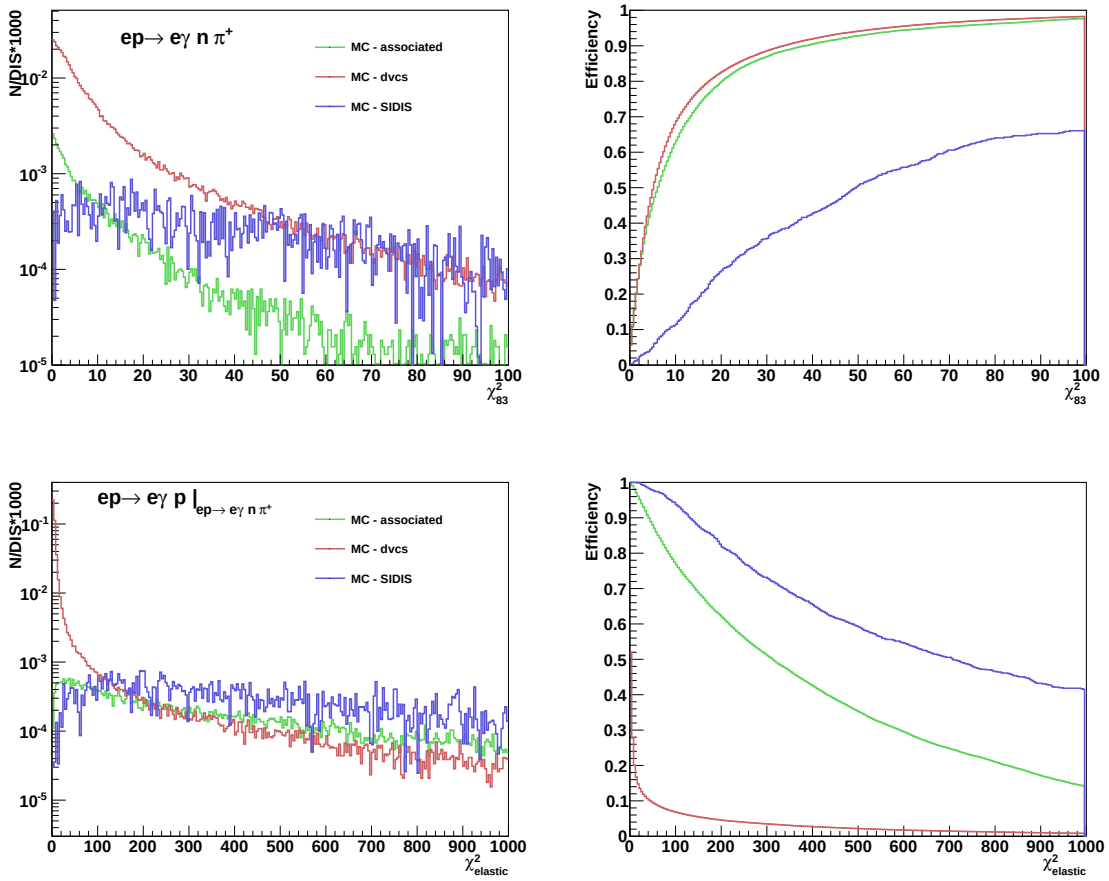

Figure 6.13.: χ^2 distributions without the lower $\chi^2_{ep\to e\gamma p}$-cut of the $ep \to e\gamma n\pi^+$ hypothesis (top left) and the corresponding efficiencies (top right). $\chi^2_{ep\to e\gamma p}$ distributions (bottom left) and the corresponding efficiency distributions for the tracks selected under the $ep \to e\gamma n\pi^+$ hypothesis but without an upper χ^2-cut (bottom right). Shown processes are elastic DVCS/BH (red), associated DVCS/BH (green) and SIDIS (blue).

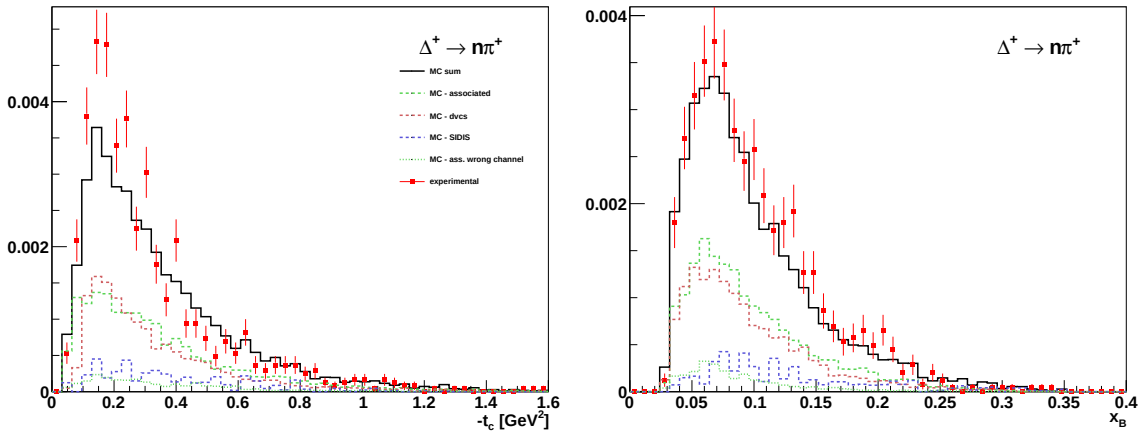

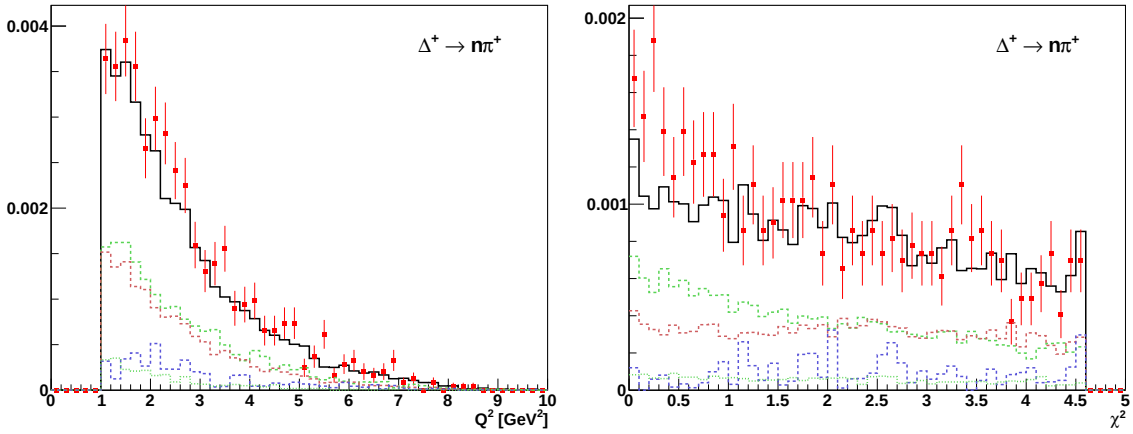

Figure 6.14.: Distributions of different channels for the kinematic variables t_c^{Δ} (previous page left), x_B (previous page right), Q^2 (left) and $\chi^2_{ep\to e\gamma n\pi^+}$ (right). Shown processes are elastic DVCS/BH (red), associated DVCS/BH (green) and SIDIS (blue).

$ep \to e\gamma n\pi^+$		associated		elastic		SIDIS	
overall		51.1 ± 1.0		37.4 ± 0.8		11.5 ± 1.3	
t_c	0.00- 0.17	54.0 ± 2.0		37.5 ± 1.5		8.5 ± 2.6	
	0.17- 0.30	47.6 ± 1.7		42.4 ± 1.6		10.0 ± 2.4	
	0.30- 0.50	51.2 ± 2.0		36.3 ± 1.5		12.5 ± 2.7	
	0.50- 1.50	52.1 ± 2.2		31.5 ± 1.5		16.3 ± 3.0	
x_B	0.03- 0.07	53.8 ± 1.6		41.1 ± 1.3		5.1 ± 1.7	
	0.07- 0.10	50.2 ± 2.0		37.3 ± 1.6		12.5 ± 3.0	
	0.10- 0.15	50.2 ± 2.1		36.5 ± 1.6		13.3 ± 3.0	
	0.15- 0.35	48.3 ± 2.3		30.1 ± 1.6		21.6 ± 3.2	
Q^2	1.00- 1.50	53.1 ± 2.1		40.2 ± 1.7		6.7 ± 2.9	
	1.50- 2.30	50.1 ± 1.9		36.7 ± 1.5		13.2 ± 2.9	
	2.30- 3.50	50.8 ± 1.8		37.8 ± 1.5		11.4 ± 2.4	
	3.50-10.0	51.0 ± 1.8		34.6 ± 1.3		14.4 ± 2.0	

Table 6.3.: Fractional contributions for the traditional $ep \to e\gamma n\pi^+$ selection, which were used for the background correction.

Alternative selection

Because $ep \to e\gamma n\pi^+$ requires the measurement of a pion in the Recoil detector, the kinematic behavior of those events is rather unique. In this alternative selection no usage of kinematic fitting for the associated process is used. Starting from the combined extraction (introduced in subsection 6.3.1), two kinematic cuts are applied, which are illustrated in figure 6.16.

The upper momentum cut of 0.5 GeV is chosen, because pions carry a rather small momentum and are not absorbed by sublayers, why they can be measured down to very small momenta even with the SFT. A lower cut on the polar angle of 1 rad follows the same arguments as in the traditional selection and is extremely powerful in removing cross-contamination by the other decay channel.

As mentioned before, an event sample with higher purity and number of events, which is almost compatible to the method 7 selection, is counterbalances by a truncated kinematic range. This can be seen in figure 6.15, where high $-t_c^\Delta$ are almost absent. Table 6.4 summarizes the contribution of background processes.

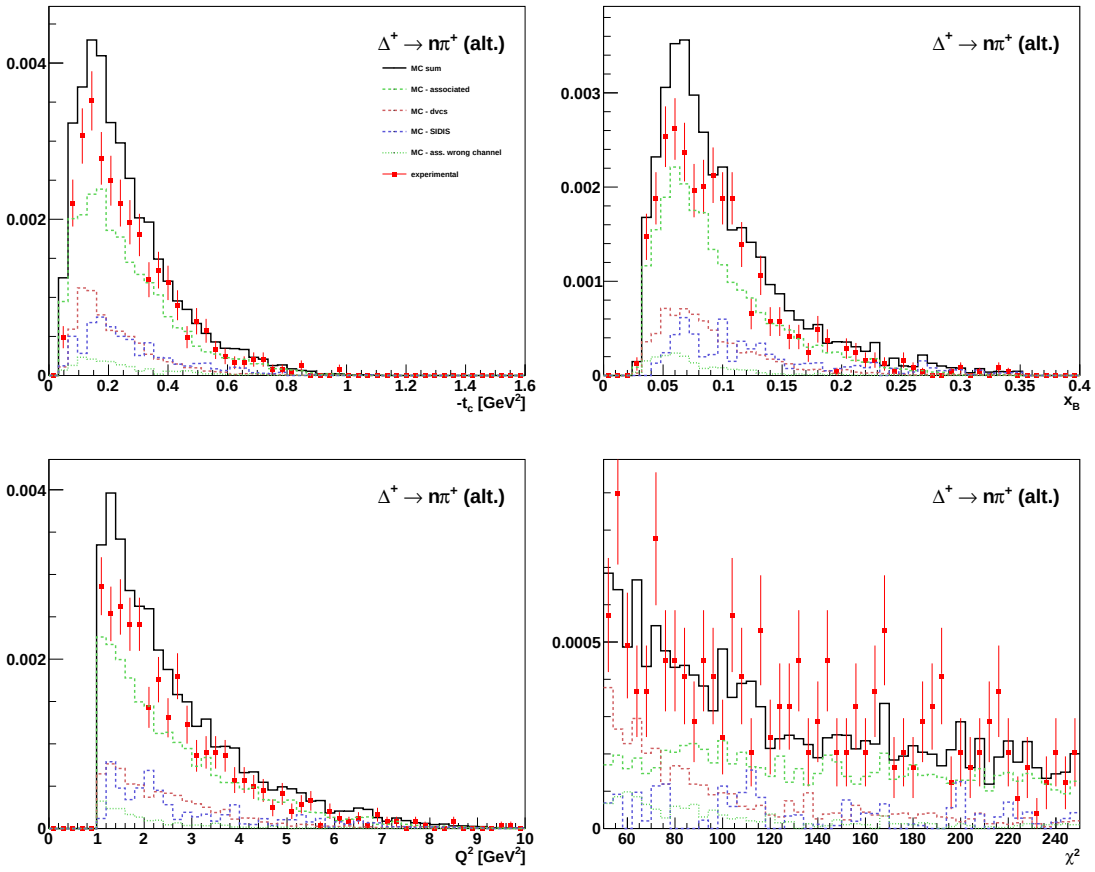

Figure 6.15.: Distributions of different channels for the kinematic variables t_c^Δ (top left), x_B (top right), Q^2 (bottom left) and $\chi^2_{ep\to e\gamma p}$ in case of the alternative associated n-sample. Shown processes are elastic DVCS/BH (red), associated DVCS/BH (green) and SIDIS (blue).

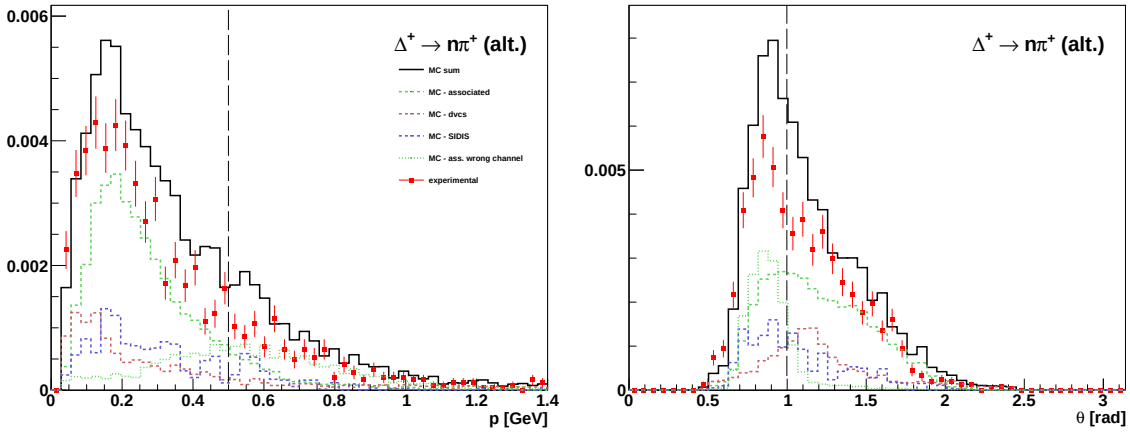

Figure 6.16.: Plots show the momentum (left) and polar angle (distribtion) of $ep \rightarrow e\gamma n\pi^+$ events after the alternative selection and the applied cut positions.

$ep \rightarrow e\gamma n\pi^+$		associated	elastic	SIDIS
overall		66.4 ± 1.3	17.9 ± 0.5	15.7 ± 1.6
t_c	0.00- 0.17	65.6 ± 2.2	22.4 ± 0.9	12.0 ± 2.7
	0.17- 0.30	63.7 ± 2.5	18.1 ± 0.9	18.2 ± 3.3
	0.30- 0.50	70.4 ± 2.5	14.0 ± 0.8	15.5 ± 2.4
	0.50- 1.50	69.6 ± 3.8	8.7 ± 0.9	21.6 ± 3.8
x_B	0.03- 0.07	72.2 ± 2.3	19.4 ± 0.8	8.4 ± 2.4
	0.07- 0.10	66.0 ± 2.7	20.5 ± 1.0	13.5 ± 3.2
	0.10- 0.15	62.5 ± 2.9	16.8 ± 1.0	20.7 ± 4.0
	0.15- 0.35	59.3 ± 2.7	12.1 ± 0.8	28.7 ± 3.5
Q^2	1.00- 1.50	70.5 ± 3.1	19.2 ± 1.0	10.3 ± 3.6
	1.50- 2.30	65.0 ± 2.7	17.5 ± 0.9	17.5 ± 3.6
	2.30- 3.50	65.0 ± 2.4	20.8 ± 1.0	14.3 ± 2.8
	3.50- 10.0	65.5 ± 2.2	14.3 ± 0.7	20.3 ± 2.3

Table 6.4.: Fractional contributions for the alternative $ep \rightarrow e\gamma n\pi^+$ selection, which were used for the background correction.

7. Extraction of BSA amplitudes

Measurement of beam spin asymmetries for associated events has already been carried out using method 7 [50]. This provides a good opportunity to test the capability of the method 3 analysis with respect to extraction of associated events. The selected event samples for method 3 and method 7 are partially correlated.
For method 3 an extended event sample of 2006 and 2007 has been used. The extension was possible, because before only events that also contained method 7 track reconstruction were considered. With respect to the data quality study in chapter 5, all positron data was available for selection (method 7 studies usually started with run 27934). Table 7.1 summarizes the number of DIS events and polarizations for 2006, 2007 and the combined data taking period which enter the asymmetry extraction according to equation 2.68.
For the elastic extraction no background correction is needed since this sample is considered as pure. The background correction for the associated processes is done according to

$$A_{corr} = \frac{A_raw - f_{el}A_{el} - f_{SIDIS}A_{SIDIS}}{1 - f_{el} - f_{SIDIS}}, \tag{7.1}$$

where A_{corr} (A_{raw}) is the corrected (measured) amplitude, A_{el} (A_{SIDIS}) are the amplitudes for the background processes [64] ([51]), and f_{el} (f_{SIDIS}) their corresponding fractions (see chapter 6).
The statistical error propagation yields

$$\delta A_{raw} = \frac{\mathrm{d}A_{raw}}{1 - f_{el} - f_{SIDIS}}, \tag{7.2}$$

$$\delta A_{el(SIDIS)} = \frac{f_{el(SIDIS)}}{1 - f_{el} - f_{SIDIS}} \cdot \mathrm{d}A_{el(SIDIS)}, \tag{7.3}$$

$$\delta f_{el(SIDIS)} = \frac{A_{raw} - A_{el(SIDIS)} - f_{SIDIS(el)}(A_{SIDIS(el)} - A_{el(SIDIS)}}{(1 - f_{el} - f_{SIDIS})^2)} \cdot \mathrm{d}f_{el(SIDIS)}, \tag{7.4}$$

$$\mathrm{d}A_{corr} = \sqrt{\delta A_{raw}^2 + \delta A_{el}^2 + \delta A_{SIDIS}^2 + \delta f_{el}^2 + \delta f_{SIDIS}^2}, \tag{7.5}$$

where $\mathrm{d}f_{el(SIDIS)}$ are the statistical errors of the calculated fractions.
Because the kinematic binning with respect to the Mandelstam t has changed, the correction was done using the overall amplitudes. Beam spin asymmetries for elastic DVCS/BH were taken from [64], beam spin asymmetries for SIDIS are extracted with a two-photon analysis [50].
The compatibility of method 7 selection with and without using Recoil PID has already been tested [65]. It was shown that by applying reasonable cuts the results are in good agreement.

	DIS			Polarization		
	$\overrightarrow{DIS^+}$	$\overleftarrow{DIS^+}$	DIS^+	$\langle\overrightarrow{\lambda^+}\rangle$	$\langle\overleftarrow{\lambda^+}\rangle$	$\langle\lambda\rangle$
06	12'866'753	2'092'219	14'958'972	33.86	-38.69	23.71
07	5'138'868	7'662'984	12'801'852	47.19	-39.66	-7.51
06+07	18'005'621	9'755'203	27'760'824	39.66	-39.45	10.56

Table 7.1.: The above table contains the number of DIS events and the corresponding average beam polarizations for all runs that were used for the BSA extraction.

7.1. Elastic channel

The compatibility of method 3 with method 7 in case of the elastic amplitudes has already been shown [61]. In figure 7.1 one can see that the good agreement also holds for the extended sample with 10588 events. Almost all deviations are inside the statistical error bars. The large deviation for the smallest t-bin can be explained by the limited acceptance of the Recoil detector for protons with a momentum below 0.25 GeV. Values are summarized in table A.4. For the time period where the Recoil detector was fully operational, about 83 % of method 3 events were covered in the method 7 selection as well. In case of the associated channels this overlap is only about 50 %, which is mainly due to the larger background for method 3 samples.

7.2. Associated channel $ep \to e\gamma\Delta^+$ (combined)

In figure 7.2 the corrected amplitudes for both methods are compared. The collected event numbers are 2583 (with an estimated purity of 76 %) for method 7 and 2253 (with an estimated purity of 67 %) in case of method 3. The constant term and the $\sin(2\phi)$ amplitude are in good agreement. In case of the $\sin(\phi)$ the amplitudes in the overall-bin have opposite sign, though with large statistical uncertainties. Both methods are in good agreement with their decay channels. For example the positive amplitude for $\sin(\phi)$ does also appear in the channel $ep \to e\gamma p\pi^0$. In case of method 7 the extracted amplitudes appear to be an almost perfect junction.
Corresponding raw amplitudes can be found in the appendix in figures A.5 and A.6. Values (of method 7) are summarized in table A.5 (A.3).

7.3. Associated channel $e^+p \to e^+\gamma p\pi^0$

In the case of $e^+p \to e^+\gamma p\pi^0$ 1425 events with an estimated purity of 54 % are selected. This high number in comparison to method 7 (about 1000 events) is due to the different

lower χ^2-cut. Unfortunately the agreement is not very satisfying. Few deviations are beyond the the errors bars and $\sin(\phi)$ has a very large positive amplitude. In addition the constant term is not compatible with 0 and has the same sign. Figure 7.3 compares the extracted amplitudes for both methods. Corresponding raw amplitudes can be found in figure A.7 and are summarized in table A.6.

7.4. Associated channel $e^+p \to e^+\gamma n\pi^+$

Figure 7.4 shows the extracted amplitudes for method 7 [51] and for both selections with method 3. In case of the traditional selection 603 events with a purity of only 51 % are selected, whereas for the alternative selection 977 events with an estimated purity of 66 % are available, which is competitive with the method 7 study. This is confirmed by a very good agreement between method 7 and the alternative method 3 selection. In contrast the traditional selection using method 3 has a very distinct negative $\sin(\phi)$ amplitude. Corresponding raw amplitudes for the traditional and alternative selection can be found in figure A.8 and A.9, respectively. Tables A.7 and A.8 summarize these values.

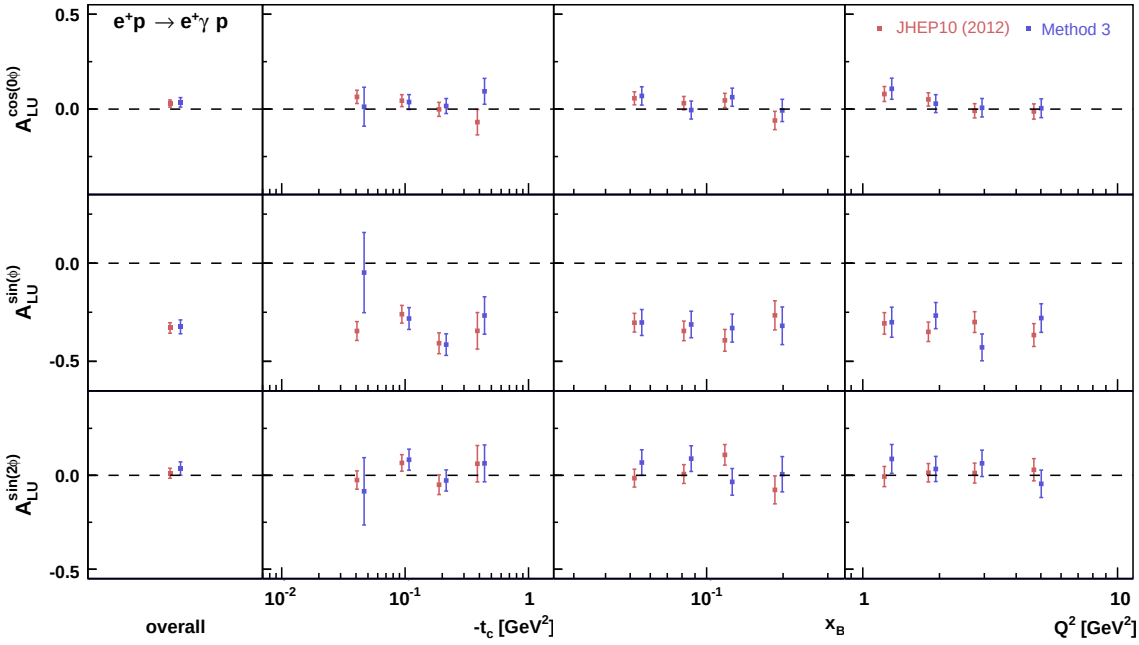

Figure 7.1.: Beam spin asymmetry amplitudes for elastic DVCS/BH ($e^+p \to e^+\gamma p$) compared to the latest HERMES publication where amplitudes were extracted using method 7 [64].

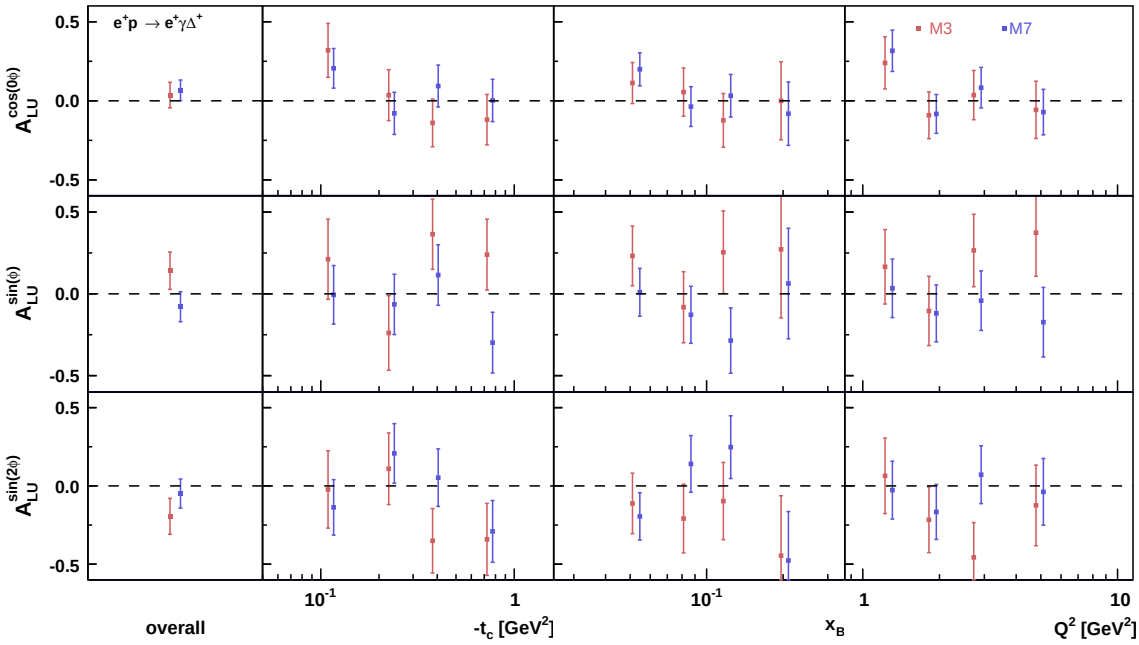

Figure 7.2.: Comparison of beam spin asymmetry amplitudes for associated DVCS/BH ($e^+p \to e^+\gamma\Delta^+$) with amplitudes of events selected with method 7.

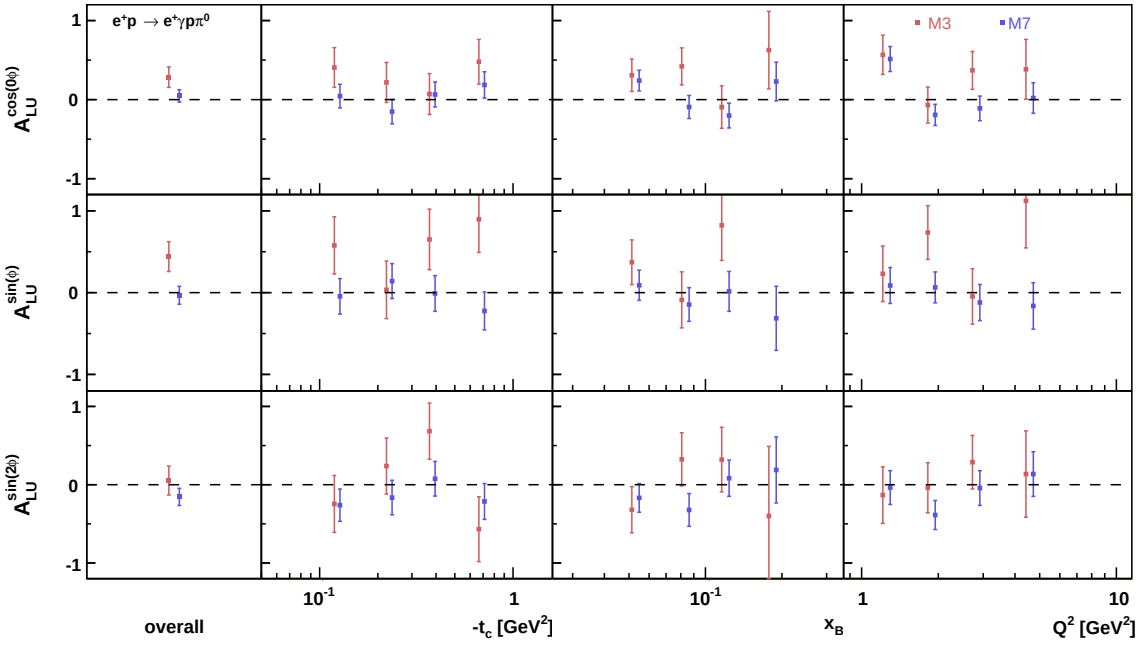

Figure 7.3.: Comparison of beam spin asymmetry amplitudes for associated DVCS/BH ($e^+p \to e^+\gamma p\pi^0$) with previous results of amplitudes of events selected with method 7.

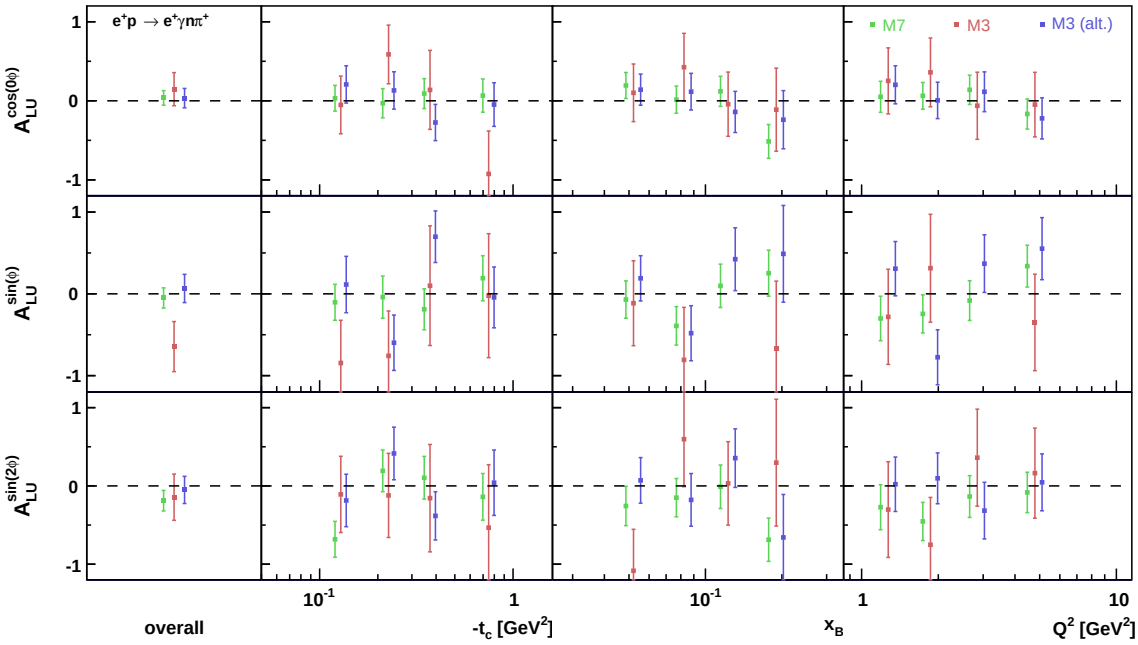

Figure 7.4.: Comparison of beam spin asymmetry amplitudes for associated DVCS/BH ($e^+p \to e^+\gamma n\pi^+$) with previous results of amplitudes of events selected with method 7.

8. Extraction of BCA amplitudes

In comparison to the previous selection for beam spin asymmetries, all available runs (according to chapter 5) for 2006 and 2007 are considered. The numbers, which are used for normalization according to equation 2.71 are summarized in table 8.1. A key problem is the relatively small number of events collected with electron beam, which hardly allows the extraction for individual kinematic bins and gives rise to the statistical errors, especially studying associated processes.

These are the first results of beam charge asymmetry measurements of associated events at HERMES and no reference values exist. However, "pure" beam charge asymmetries for elastic DVCS/BH were extracted in order to prepare the following analysis and are in good agreement with previous HERMES results using the forward spectrometer only (please refer to [66] and [56] for further details). Secondly the comparison to previously extracted beam spin asymmetries as shown in chapter 7, helps to interpret the results in terms of their precision and compatibility with theoretical predictions as shown in section 2.1.3. The applied background corrections are done according to equations 7.1 and 7.2 as described in the previous chapter. The correction for elastic DVCS/BH is done using the extracted overall amplitudes from the preliminary pure sample. Beam charge asymmetries of SIDIS are compatible with zero [67].

	DIS			Charge
	DIS^+	DIS^-	DIS	$\langle\eta\rangle$
06	14′958′972	2′309′511	17′268′483	0.733
07	12′801′852	-	12′801′852	1
06+07	27′760′824	2′309′511	30′070′335	0.846

Table 8.1.: The above table contains the number of DIS events and the corresponding average beam charge for all runs that were used for the BCA extraction.

8.1. Associated channel $ep \to e\gamma\Delta^+$ (combined)

The extracted asymmetries for the combined associated sample can be found in Figure 8.1. Table A.9 contains the values of raw and corrected amplitudes. 2477 events (224 measured with the electron beam) are contained in the selected data sample. In principle the constant term has to be suppressed by a negative kinematical factor, which is the case within statistical uncertainties, and therefore is yet acceptable. Systematic uncertainties due to background correction and wrongly assigned background contributions are not included. If we neglect the constant term, the overall amplitude is positive and theoretical predictions are found to be in agreement with the measurement.

8.2. Associated channel $ep \to e\gamma p\pi^0$

The selected sample for $ep \to e\gamma p\pi^0$ contains 1543 events (118 measured with the electron beam). The raw and corrected amplitudes are written in table A.10 and plotted in figure 8.2. ln comparison to previous extractions, some strong oscillation in the kinematic dependence can be found (for example in the t-dependence of $\cos(3\phi)$). Some of the corrected amplitudes even reach unphysical asymmetry values above $+1$ or below -1 in the highest x_B bin. Theoretical predictions seem to be in agreement with the data, however in connection with the bad agreement for beam spin asymmetries, the trustiness of the results has to be questioned.

8.3. Associated channel $ep \to e\gamma n\pi^+$

The two samples for $ep \to e\gamma n\pi^+$ contain 653 events (50 measured with the electron beam) in case of the traditional selection and 1057 events (80 measured with the electron beam) in case of the alternative selection. Besides a rather smooth shape for kinematic dependence in comparison to $ep \to e\gamma p\pi^0$, the same weak points in the traditional analysis can be observed (see figures 8.4 and A.10). The values are summarized in tables A.11 and A.12. According to the Monte-Carlo only about 25 of the selected events from electron data are not background. Because of the weak agreement between real data and Monte-Carlo this number is likely to be different, which might have a large impact on the outcome of the extraction. Hence the precision of this measurement is questionable and results have to be doubted.
In contrast the extracted amplitudes for $ep \to e\gamma n\pi^+$ from the alternative sample are mostly compatible with zero with a small positive deviation for the overall $\cos(\phi)$ amplitude (see figures 8.3 and 8.4). Due to the improved statistics the errors are reduced by almost a factor of two or more. With the exception of one Q^2 bin for $\cos(2\phi)$, no amplitudes show huge oscillations or unphysical behavior even in case of the corrected amplitudes.

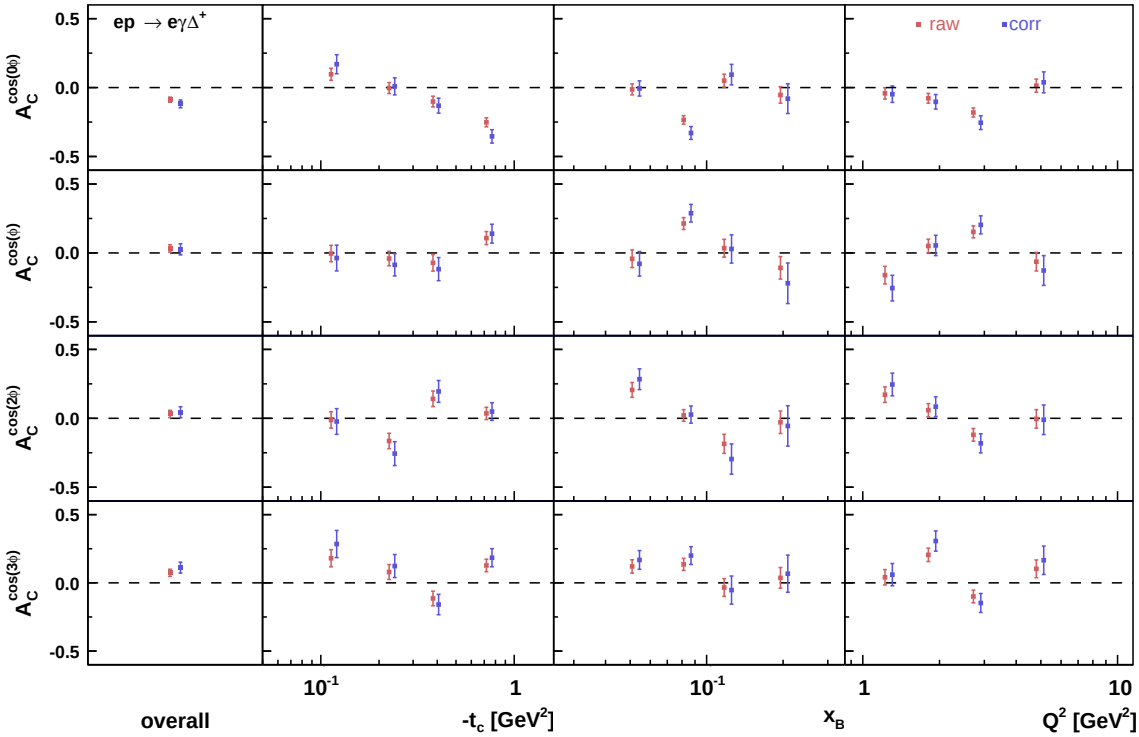

Figure 8.1.: Raw and corrected beam charge asymmetrie amplitudes for associated DVCS/BH ($ep \to e\gamma\Delta^+$).

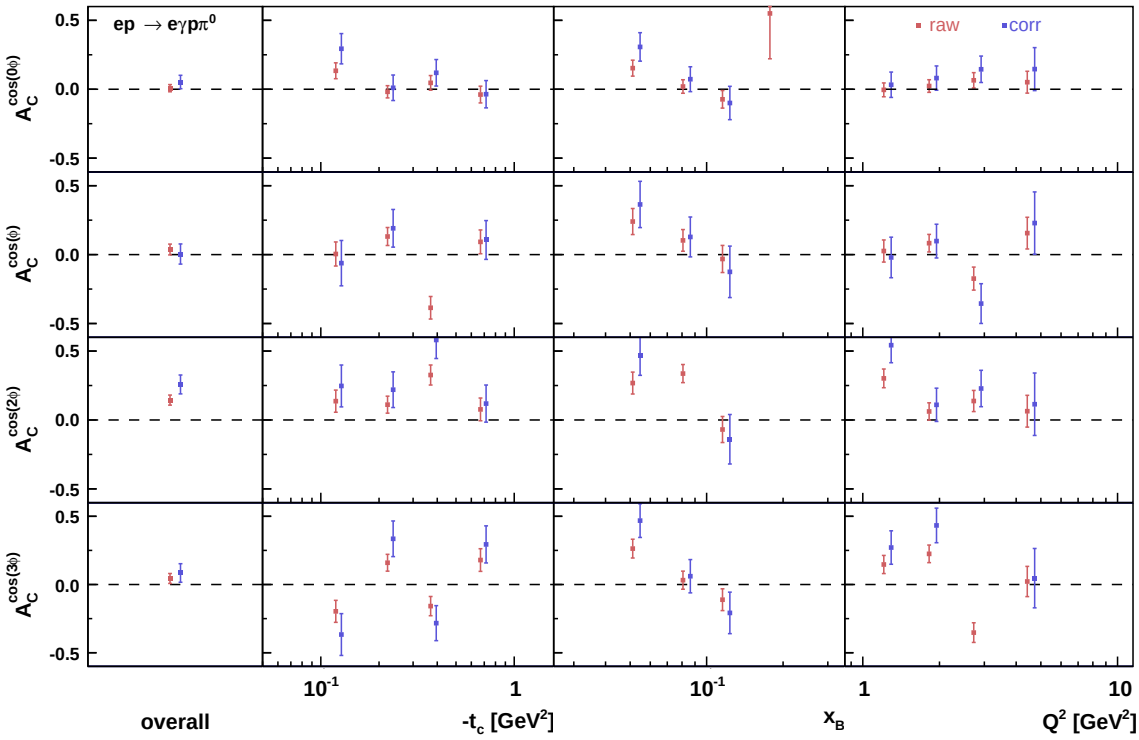

Figure 8.2.: Raw and corrected beam charge asymmetrie amplitudes for associated DVCS/BH ($ep \to e\gamma p\pi^0$).

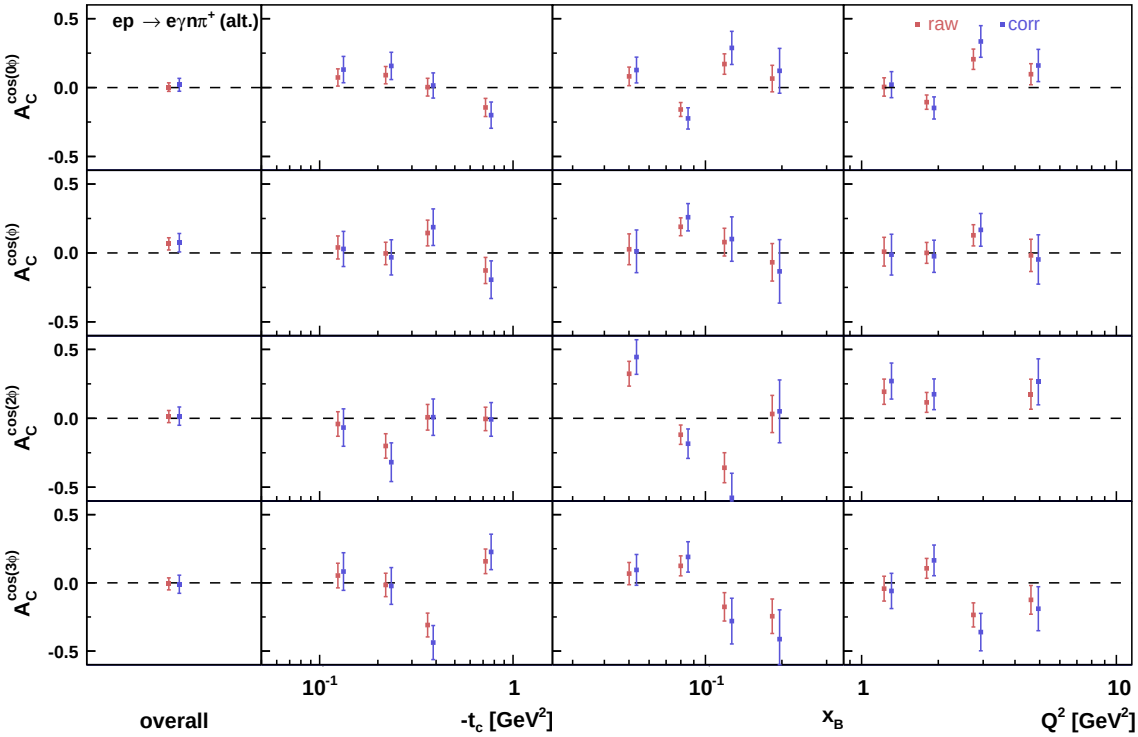

Figure 8.3.: Raw and corrected beam charge asymmetrie amplitudes for associated DVCS/BH ($ep \to e\gamma n\pi^+$) selected with the alternative approach. .

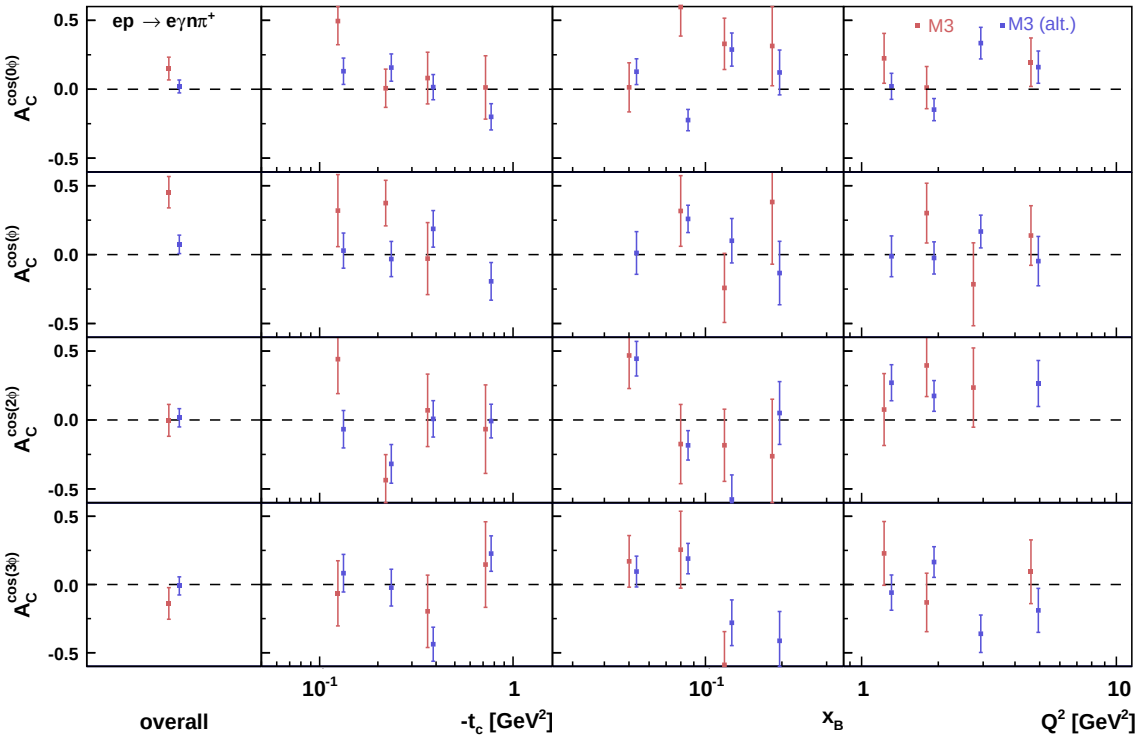

Figure 8.4.: Comparison of beam charge asymmetrie amplitudes for associated DVCS/BH ($ep \to e\gamma n\pi^+$) selected with the traditional and alternative approach.

9. Summary and conclusion

For the first time beam charge asymmetry amplitudes for associated DVCS/BH ($ep \to e\gamma\Delta$) and the underlying processes $ep \to e\gamma p\pi^0$ and $ep \to e\gamma n\pi^+$ have been measured at HERMES . After a brief introduction to the theoretical framework given by GPDs for the elastic process $eN \to e\gamma N$ and their extension to the case of $eN \to e\gamma N\pi$, the HERMES experiment was described focussing on the Recoil detector. This analysis is also the first to include Recoil information for the entire 2006, 2007 data taking period. Therefore an additional data quality study was carried out in order to check for inconsistencies, especially in the DVCS/DIS ratio, which is of high importance for the normalization of the selected samples.

Before 2006 the selection of associated DVCS/BH was not feasible because their corresponding missing mass region is highly dominated by the SIDIS and abundant elastic DVCS/BH events. Due to the installation the HERMES Recoil detector, measurements of charged recoiling particles became possible and in this connection kinematic fitting under two constraints could be carried out.

Because only the Recoil detector's scintillating fibre tracker (SFT) was fully operational for the early data taking period of 2006, which includes all data that has been recorded with the electron beam, only a simplified track reconstruction was applicable. This so called method 3 does not have any degrees of freedom left, which prevents the identification and rejection of ghost tracks. This implies higher track multiplicities inside the Recoil detector that have to be dealt with. In preparation for this thesis the resolution for method 3 had been determined and was optimized in order to compensate for the missing particle identification with method 3. Particle identification would have been very useful to suppress cross contamination between the decay channels of the Δ-resonance.

A detailed Monte-Carlo study was made to evaluate fractions of the main background processes and determine additional cuts to improve the samples' purity. Besides the traditional approach of using kinematic fitting under the respective hypothesis, a statistically more significant combined associated sample using a lower χ^2-cut for kinematic fitting under the elastic hypothesis was selected. Due to characteristic kinematics an improved, so called alternative sample of the process $ep \to e\gamma n\pi^+$ could be selected.

Extractions of beam spin asymmetry amplitudes were repeated using method 3 and compared with previous results obtained with method 7. In case of the combined associated analysis, the extraction with method 7 was done for the first time as well. Extractions which were only based on kinematic fitting for the elastic processes (namely the combined associated sample and the alternative $\Delta \to n\pi^+$ sample) were in good agreement for both methods. The agreement for the remaining selections is much weaker and in some cases an agreement can only be reached if a large systematic uncertainty would be applied.

A similar behavior could be observed for the extracted beam charge asymmetry amplitudes, although no reference values are available. When the samples were extracted using kinematic

fitting for an associated hypothesis, at least one of the overall amplitudes showed a fluctuating behavior and the kinematic dependence was partially not smooth. One of the reasons could be that the fractions, on which the background correction is based on are not determined correctly. This is quite probable due to a rather poor agreement between Monte-Carlo and real data, especially for the channel $ep \to e\gamma p\pi^0$. Furthermore the selected event numbers are limited with only a small fraction of events with a positive beam charge. Because the extraction for method 7 without using Recoil PID repeated previous results well, the main problem seems to be the inferior resolution of method 3. Theoretical predictions are mostly in agreement with the measurements within their statistical uncertainties. For both channels all but one amplitude are compatible with zero.
In contrast, the extracted beam charge asymmetry amplitudes for the combined associated sample and the alternative sample for the process $ep \to e\gamma n\pi^+$ are solid. Overall amplitudes and kinematical dependence appear to be reasonable. For each sample all but one amplitude are compatible with zero within their statistical uncertainties. Although the kinematic range of the alternative $ep \to e\gamma n\pi^+$ is limited, measurements and theoretical predictions are in good agreement.

Despite the relatively small data sample for positive beam charge and the limited resolution and missing particle identification for the reconstruction using the scintillating fibre tracker only, first results were obtained. Previous measurements done with a fully operational Recoil detector for beam spin asymmetries hint the true potential of the HERMES experiment. Nevertheless the possibility to select associated events using a hybrid of kinematic fitting for the elastic hypothesis and the missing-mass technique might be interesting for method 7 studies on beam spin asymmetry as well. In order to release the presented results, the systematic uncertainties have yet to be investigated. Their magnitude will be dominated by the size of the background corrections and the systematics from BSA comparisons as described in this thesis.

Bibliography

[1] J. J. Aubert, et al.: *A detailed study of the nucleon structure functions in deep inelastic muon scattering in iron*, Nucl. Phys. B 272, 158 (1986) 1

[2] C. G. Callan Jr., D. J. Gross: *High-Energy Electroproduction and the Constitution of the Electric Current*, Phys. Rev. Lett. 22, 156 (1969) 1

[3] J. D. Bjorken: *Applications of the Chiral* $U(6) \otimes U(6)$ *Algebra of Current Densities*, Phys. Rev. 148, 1467 (1966) 1

[4] J. Ellis, R. Jaffe: *Sum rule for deep-inelastic electroproduction from polarized protons*, Phys. Rev. D 9, 1444 (1974) 2

[5] J. Ashman, et al.: *A measurement of the spin asymmetry and determination of the structure function* g_1 *in deep inelastic muon-proton scattering* , Phys. Lett. B 206, 364 (1988) 2

[6] A. Airapetian, et al.: *Precise determination of the spin structure function* g_1 *of the proton, deuteron, and neutron*, Phys. Rev. D 75, 012007 (2007) 2

[7] V. Yu. Alexakhin, et al.: *The deueron spin-dependent structure function* g_1^d *and its first moment*, Phys. Lett. B 647, 8 (2007) 2

[8] J. Blümlein, H. Böttcher: *QCD analysis of polarized deep-inelastic scattering data and parton distributions*, Nucl. Phys. B 636 (2002) 2

[9] M. Hirai, S. Kumano, N. Saito: *Determination of polarized parton distribution functions with recent data on polarization asymmetries*, Phys. Rev. D 74, 014015 (2006) 2

[10] D. de Florian, R. Sassot, M. Stratmann, W. Vogelsang: *Global Analysis of Helicity Parton Densities and their Uncertainties*, Phys. Rev. Lett. 101, 72001 (2008) 2

[11] H. Avakian, S. J. Brodsky, A. Deur, F. Yuan: *Effect of Orbital Angular Momentum on Valence-Quark Helicity Distributions* Phys. Rev. Lett. 99, 082001(2007) 2

[12] X. Ji:*Gauge-Invariant Decomposition of Nucleon Spin*, Phys. Rev. Lett. 78, 610 (1997), Phys. Rev. D 55, 7114 (1997) 2, 7

[13] E. P. Wigner:*On the Quantum Correction For Thermodynamic Equilibrium*, Phys. Rev. 40, 749 (1932) 4

[14] S. J. Brodsky, H.-C. Pauli, S. S. Pinsky: *Quantum chromodynamics and other field theories on the light cone*, Phys. Rep. 301, 299 (1998) 4

[15] J. B. Kogut, D. E. Soper: *Quantum Electrodynamics in the Infinite-Momentum Frame*, Phys. Rev. D 1, 2901 (1970) 4

[16] R. P. Feynman: *Photon-Hadron Interactions*, Addison Wesley Longman, Inc. (1972) 5

[17] A. V. Belitsky, X. Ji, F. Yuan: *Quark imaging in the proton via quantum phase-space distributions*, Phys. Rev. D 69, 074014 (2004)] 5

[18] X. Ji, W. Melnitchouk, X. Song: *Study of off-forward parton distributions*, Phys. Rev. D 56, 5511 (1997) 7

[19] V. Petrov, et al.: *Off-forward quark distributions of the nucleon in the large-N_c limit*, Phys. Rev. D 57, 4325 (1998) 7

[20] D. Müller, et. al.: *Wave Functions, Evolution Equations and Evolution Kernels from Light-Ray Operators of QCD*, Fortsch. Phys. 42, 101 (1994) 7

[21] A. V. Radyushkin: *Nonforward parton distributions*, Phys. Rev. D 56, 5524 (1997) 7

[22] M.V. Polyakov, C. Weiss: *Skewed and double distribution in the pion and the nucleon*, Phys. Rev. D 60, 114017 (1999) 7, 11

[23] K. Goeke, M.V. Polyakov, M. Vanderhaeghen: *Hard exclusive reactions and the structure of hadrons*, Prog. Part. Nucl. Phys. 47, Issue 2, 401 (2001) 7, 8, 9

[24] M. Vanderhaeghen, P. A. M. Guichon, M. Guidal: *Deeply virtual electroproduction of photons and mesons on the nucleon: Leading order amplitudes and power corrections*, Phys. Rev. D 60, 094017 (1999) 7

[25] P. A. M. Guichon, L Mossé, M. Vanderhaeghen: *Pion production in deeply virtual Compton scattering*, Phys. Rev. D 68, 034018 (2003) 7, 10

[26] H. F. Jones, M. D. Scadron: *Multipole $\gamma N - \Delta$ form factors and resonant photo- and electroproduction*, Ann. of. Phys. 81, Issue 1, 1 (1973) 8

[27] S. Adler: *Photo-, electro-, and weak single-pion production in the (3,3) resonance region*, Ann. of. Phys. 50, Issue 2, 189 (1968); Phys. Rev. D 12, 2644 (1975) 9

[28] L. Tiator, D. Drechsel, O. Hanstein, S. S. Kamalov, S. N. Yang: *The $E2/M1$ and $C2/M1$ ratios and form factors in $N \to \Delta$ transitions* Nucl. Phys. A 689, 205 (2001) 9

[29] S. Adler, R. Dashen: *Current Algebras* Benjamin, New York (1968) 9

[30] M. Guidal, S. Bouchigny, J. P. Didelez, C. Hadjidakis, E. Hourany, M. Vanderhaeghen: *Generalized Parton Distributions and Nucleon Resonances* arXiv:hep-ph/0304252v1 9

[31] A. V. Belitsk, D. Müller, A. Kirchner: *Theory of deeply virtual compton scattering on the nucleon*, Nucl. Phys. B 629, 323 (2002) 12, 15

[32] V. A. Korotkov, W.-D. Nowak: *Future Measurements of Deeply Virtual Compton Scattering at HERMES*, arXiv:hep-ph/0108077; DESY-HERMES-01-109 13, 15

[33] Z. Ye: *Transverse Target-Spin Asymmetry Associated with Deeply Virtual Compton Scattering on the Proton and A Resulting Model-Dependent Constraint on the Total Angular Momentum of Quarks in the Nucleon* Ph.D. thesis, University Hamburg (2006) 16

[34] M. J. Murray: *DVCS at HERMES: The Recoil Detector & Transverse Target Spin Asymmetries* PhD-Thesis, DESY (2008) 19

[35] A. A. Sokolov, I. M. Ternov: *On polarization and spin effects in synchrotron radiation theory* Sov. Phys. Doklady 8, 1203 (1964) 19

[36] M. Düren: *The HERMES Experiment: From the Design to the First Results*, Habilitation thesis, Friedrich-Alexander-Universität Erlangen-Nürnberg (1995) 20, 21

[37] D. P. Barber et al.: *The HERA polarimeter and the first observation of electron spin polarization at HERA* Nucl. Instrum. Meth. A 329, 79 (1993) 20

[38] M. Beckmann et al: *The Longitudinal Polarimeter at HERA* Nucl. Instrum. Meth A 479, 334 (2002) 20

[39] S. Belostotski, et al.: *The HERMES Recoil Detector - Technical Design Report*, Internal Report, DESY-HERMES-02-003 (2002) 20, 25

[40] W. Wander: *Rekonstruktion hochenergetischer Streuereignisse im HERMES Experiment* PhD-Thesis, Friedrich-Alexander-Universität Erlangen-Nürnberg (1996) 21

[41] H. Avakian, et al.: *Performance of F101 Radiation Resistant Lead Glass Shower Counters* NIM A 378, 155 (1996) 21

[42] R. Kaiser: *Particle Identification at HERMES* Internal Report 97-025 (1997) 22

[43] I. Lehmann, et al.: *Heating studies on the HERMES Target Cell* Internal Report 06-080 (2006) 23

[44] M. Reinecke, et al.: *A silicon strip recoil detector for momentum measurement and tracking at HERMES* Nuclear Science Symposium Conference Record, Vol. 1, 561 (2003) 23

[45] M. Hoek: *Design and Construction of a Scintillating Fibre Tracker for measuring Hard Exclusive Reactions at HERMES* PhD-Thesis, Justus-Liebig-Univeristät Gießen (2006) 24

[46] J. Bowles, J. Burns, M. Murray, W.-D. Nowak , C. Riedl, S. Yaschenko: *Amplitudes of the single-charge beam-helicity asymmetry in DVCS off a hydrogen target with the proton remaining in the ground state*, Release Report (2011) 25, 27

[47] J. Bowles, J. Burns, M. Murray, C. Riedl, S. Yaschenko: *Extraction of elastic and background amplitudes of the DVCS singe-charge beam-spin asymmetry from the 2006/2007*

hydrogen data set including the analysis of Recoil detector data, Extended Analysis Report (2010) 25

[48] E. Etzelmüller: *Studies of proton momentum resolution and kinematic fitting for the HERMES detector with recoil track reconstruction using the Scintillating Fibre Tracker only*, Vertiefungsmodul, Justus-Liebig Universität Gießen (2012); http://fss.plone.uni-giessen.de/fss/fbz/fb07/fachgebiete/physik/einrichtungen/2pi/ag/ag-dueren/docs/studienarbeiten/201205etzelmuellermodul/file/201205etzelmuellermodul.pdf 26, 40

[49] Hanna++ Documentation: http://www-hermes.desy.de/groups/rcoilgrp/recoil/Documents/technical/software/Hanna++/html/index.html 27

[50] I. Brodski, E. Etzelmüller, A. Movsisyan, S. Yaschenko for the recoil detector and DVCS groups: *Beam-helicity asymmetry in associated electroproduction of real photons* $ep \to e\gamma\Delta^+$, Analysis Report (2012) 27, 34, 47, 51, 56

[51] A. Movsisyan: *Associated DVCS: Update*, Collaboration Meeting (2012) 27, 29, 56, 58

[52] Z. Akopov: talk given about beam energy, Collaboration Meeting (2007) http://www-hermes.desy.de/PLOTS/0703/zaven/newbeamenergy.pdf 27

[53] S. Yaschenko: *private communication* 31

[54] X-G. Lu: *The HERMES Recoil Detector: Particle Identification and Determination of Detector Efficiency of the Scintillating Fiber Tracker*, Diplomarbeit, Universität Hamburg (2009) 31

[55] A. Airapetian, et al.: *Exclusive Leptoproduction of Real Photons on a Longitudinally Polarised Hydrogen target*, JHEP 06, 019 (2010) 33

[56] A. Airapetian, et al.: *Beam-helicity and beam-charge asymmetries associated with deeply virtual Compton scattering on the unpolarised proton*, JHEP 07, 032 (2012) 33, 61

[57] Summary of 2006: http://hermes.desy.de/UDST_DOCU/RUNNING/major.events.asc 37, 39

[58] C. Riedl: *private communication* 37

[59] Recoil offline data quality: http://hermes.desy.de/groups/daqlgrp/OFFLINE_DQ/uDST/RDdaql.html 38, 39

[60] HERMES Wiki (MC Productions): https://hermes-wiki.desy.de/MC_Productions 40

[61] E. Etzelmüller: *Completion of feasibility study of recoil tracking and extraction of beam-helicity asymmetry using Scintillating Fibre Tracker only* Spezialisierungsmodul,

Justus-Liebig-Universität Gießen (2012); http://fss.plone.uni-giessen.de/fss/fbz/fb07/fachgebiete/physik/einrichtungen/2pi/ag/ag-dueren/docs/groupseminar/201212EtzelmuellerSpezial/file/201212EtzelmuellerSpezialisierungsmodul.pdf 40, 57

[62] L. Demortier, L. Lyons:*Everything you always wanted to know about pulls*, CDF note (2002) 43

[63] A. Airapetian, et al.: *Beam-helicity asymmetry arising from deeply virtual Compton scattering measured with kinematically complete event reconstruction*, Response to referee (2012), http://www-hermes.desy.de/notes/pub/publications/rdDVCS.v4.2.comments-ResponseToReferee.pdf 45

[64] A. Airapetian, et al.: *Beam-helicity asymmetry arising from deeply virtual Compton scattering measured with kinematically complete event reconstruction*, JHEP 10, 042 (2012) 56, 59

[65] E. Etzelmüller: *Feasibility study for selection of associated processes using the Scintillating Fibre Tracker for recoil track reconstruction only* talk, "Christmas" Analysis Week (2012), http://www-hermes.desy.de/groups/mgmtgrp/COLLABMEETINGS/AWEEK_DEC12/Exclusive-DVCS/erik_dec12.pdf 56

[66] I. Brodski: *unkown title* PhD-Thesis, Justus-Liebig-Universität Gießen (in preparation) 61

[67] A. Movsisyan: *Deeply Virtual Compton Scattering off a Deuterium Target at the HERMES Experiment* PhD-Thesis, Yerevan Physics Institute (2011) 61

List of Figures

2.1. Handbag diagram for (associated) DVCS . . . 6
2.2. Theoretical estimation of BCA and BSA . . . 10
2.3. Feynman diagrams for DVSC and BH . . . 11
2.4. Estimated cross sections for DVCS and BH . . . 13
2.5. Diagram for DVCS kinematics . . . 17
3.1. Schematic overview of HERA . . . 19
3.2. Side view of the HERMES forward spectrometer . . . 21
3.3. Sectional view of the HERMES Recoil detector . . . 23
3.4. Schematic drawings of the SFT . . . 24
3.5. Acceptance of the HERMES Recoil detector . . . 24
3.6. Track reconstruction using the scintillating fibre tracker . . . 25
3.7. Comparison between true and measured momentum and polar angle with Monte Carlo . . . 26
4.1. Low efficieny in case of quadrant 2 . . . 31
4.2. Comparison of track multiplicities . . . 32
4.3. χ^2-distributions for different track multiplicities . . . 33
5.1. Overview of available data, its polarization and charge . . . 36
5.2. Comparison of DVCS/DIS for the different methods . . . 37
5.3. DVCS/DIS ratio for method 3 . . . 38
5.4. Quadwise comparison of the DVCS/DIS ratio . . . 39
6.1. Parametrisation of proton and pion resolution . . . 40
6.2. Optimization of kinematic fitting for par_8 . . . 41
6.3. Pull distributions for $ep \to e\gamma p$ . . . 42
6.4. Pull distributions for $ep \to e\gamma p\pi^0$ . . . 44
6.5. Pull distributions for $ep \to e\gamma n\pi^+$ . . . 44
6.6. M_x^2 distribution for associated (combined) M3 and M7 . . . 45
6.7. χ^2 and efficieny distributions of $ep \to e\gamma p$ hypothesis . . . 46
6.8. Kinematic distributions for associated selection (combined) . . . 46
6.9. Momentum distribution of $ep \to e\gamma p\pi^0$ . . . 48
6.10. χ^2 and efficieny distributions of $ep \to e\gamma p\pi^0$ hypothesis . . . 48
6.11. Kinematic distributions for $ep \to e\gamma p\pi^0$ selection . . . 49
6.12. Polar angle distribution of $ep \to e\gamma n\pi^+$ (traditional) . . . 50
6.13. χ^2 and efficieny distributions of the traditional $ep \to e\gamma n\pi^+$ hypothesis . . . 52
6.14. Kinematic distributions for the traditional $ep \to e\gamma n\pi^+$ selection . . . 53
6.15. Kinematic distributions for the alternative $ep \to e\gamma n\pi^+$ selection . . . 54
6.16. Momentum and polar angle distributions of $ep \to e\gamma n\pi^+$ (alternative) . . . 55
7.1. BSA amplitudes for $e^+p \to e^+\gamma p$ . . . 59

7.2. Comparison of BSA amplitudes for $e^+p \to e^+\gamma\Delta^+$ with method 7 59
7.3. Comparison of BSA amplitudes for $e^+p \to e^+\gamma p\pi^0$ with method 7 60
7.4. Comparison of BSA amplitudes for $e^+p \to e^+\gamma n\pi^+$ with method 7 60
8.1. BCA amplitudes for $ep \to e\gamma\Delta^+$ 63
8.2. BCA amplitudes for $ep \to e\gamma p\pi^0$ 63
8.3. BCA amplitudes for $ep \to e\gamma n\pi^+$ (alternative) 64
8.4. Comparison of BCA amplitudes for $ep \to e\gamma n\pi^+$ selected with the traditional and alternative approach 64
A.1. Average track multiplicities for method 3 75
A.2. Extended quadwise comparison of the DVCS/DIS ratio 75
A.3. Optimization of kinematic fitting for par_6 76
A.4. Optimization of kinematic fitting for par_7 76
A.5. BSA amplitudes for $e^+p \to e^+\gamma\Delta^+$ 79
A.6. BSA amplitudes for $e^+p \to e^+\gamma\Delta^+$ (method 7) 79
A.7. BSA amplitudes for $e^+p \to e^+\gamma p\pi^0$ 80
A.8. BSA amplitudes for $e^+p \to e^+\gamma n\pi^+$ (traditional) 80
A.9. BSA amplitudes for $e^+p \to e^+\gamma n\pi^+$ (alternative) 81
A.10. BCA amplitudes for $ep \to e\gamma n\pi^+$ (traditional) 90

List of Tables

4.1. Summary of cuts for final selection 35
5.1. Table summarizing the excluded regions 39
6.1. Fractional contributions for the $ep \to e\gamma\Delta^+$ selection 47
6.2. Fractional contributions for the $ep \to e\gamma p\pi^0$ selection 50
6.3. Fractional contributions for the traditional $ep \to e\gamma n\pi^+$ selection 53
6.4. Fractional contributions for the alternative $ep \to e\gamma n\pi^+$ selection 55
7.1. DIS numberse and polarization for BSA extraction 57
8.1. DIS numberse and polarization for BCA extraction 61
A.1. Extended fractional contributions for the $ep \to e\gamma p\pi^0$ selection 77
A.2. Extended fractional contributions for the traditional $ep \to e\gamma n\pi^+$ selection . 77
A.3. BSA amplitudes for $e^+p \to e^+\gamma p\Delta^+$ (method 7) 78
A.4. BSA amplitudes for $e^+p \to e^+\gamma p$ 81
A.5. BSA amplitudes for $e^+p \to e^+\gamma\Delta^+$ 82
A.6. BSA amplitudes for $e^+p \to e^+\gamma p\pi^0$ 83
A.7. BSA amplitudes for $e^+p \to e^+\gamma n\pi^+$ (traditional) 84
A.8. BSA amplitudes for $e^+p \to e^+\gamma n\pi^+$ (alternative) 85
A.9. BCA amplitudes for $ep \to e\gamma\Delta^+$ 86
A.10. BCA amplitudes for $ep \to e\gamma p\pi^0$ 87
A.11. BCA amplitudes for $ep \to e\gamma n\pi^+$ (traditional) 88
A.12. BCA amplitudes for $ep \to e\gamma n\pi^+$ (alternative) 89

A. Appendix

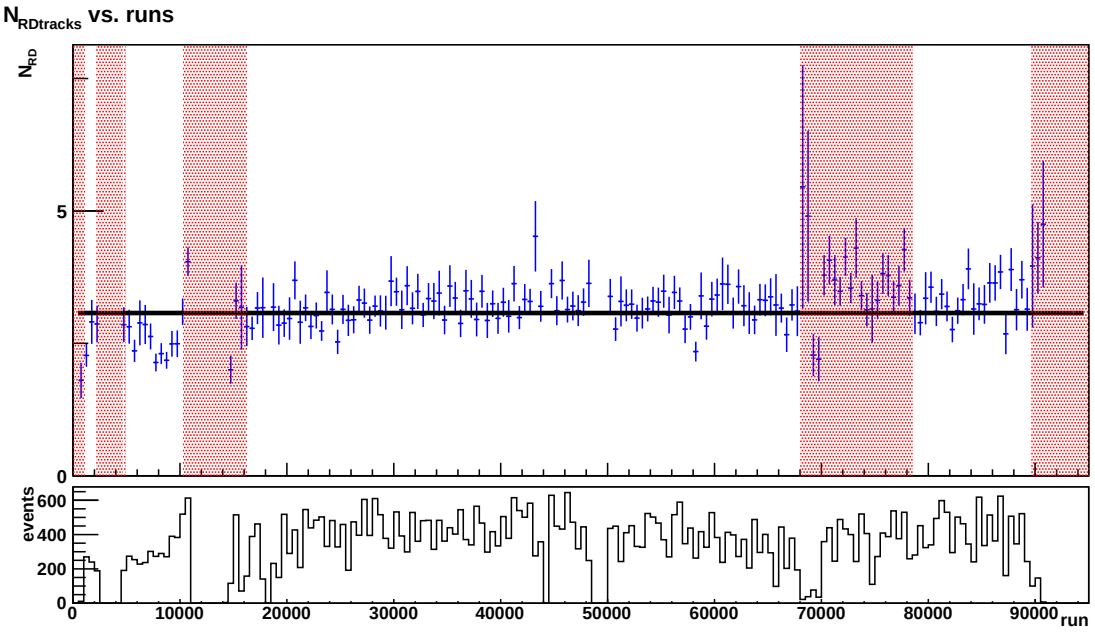

Figure A.1.: The upper plots shows the average track muliplicities for runs taken during 2006 and 2007. This study didn't result in additional cuts to the runs used in the analysis.

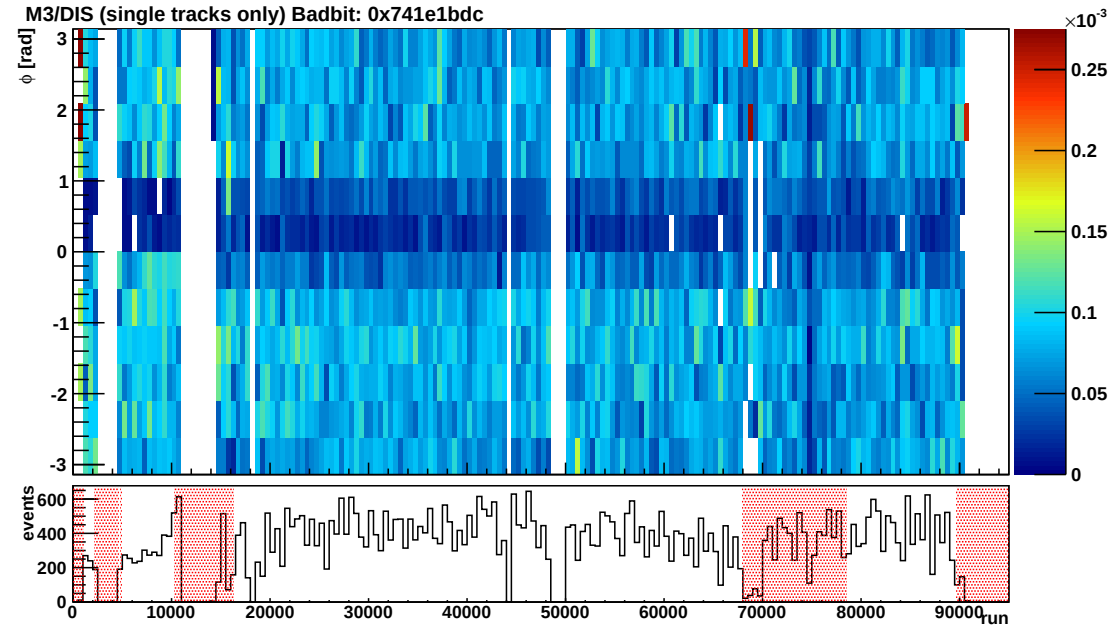

Figure A.2.: This plots is similar to figure 5.4. In addition each quadrant has been divided into three parts to observe problematic regions within a quadrant. Except quadrant 2, all others appear to worked as expected. The lower histogramm displays the number of recorded events for each bin and marks the excluded regions.

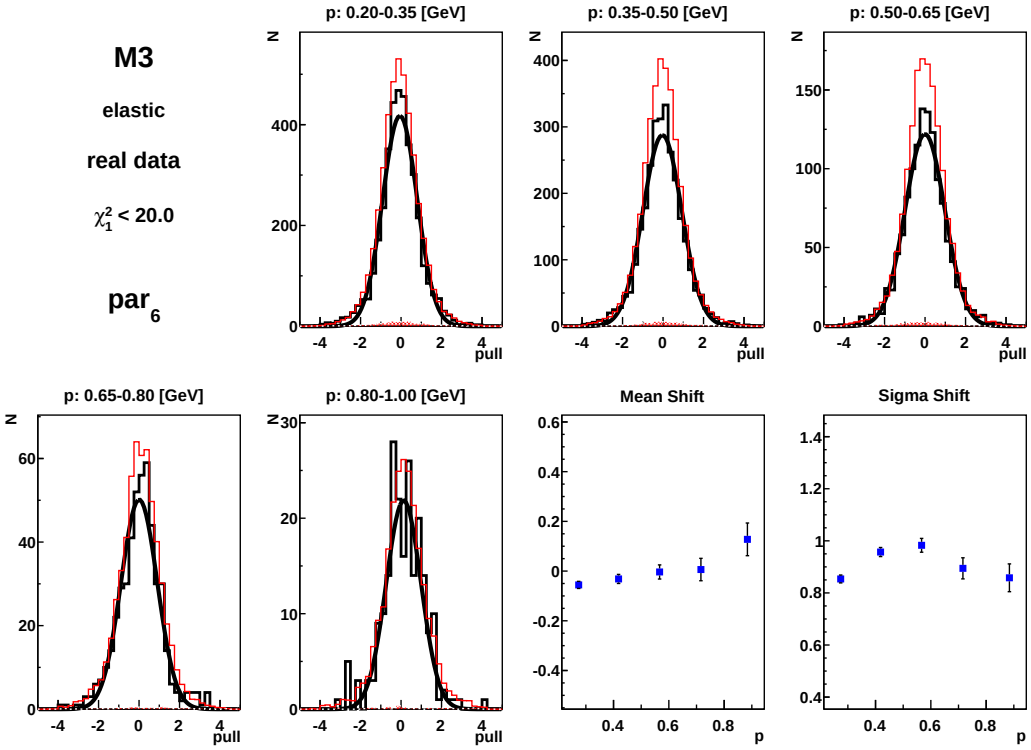

Figure A.3.: Illustration of the optimization of kinematic fitting for par_6. For further description please refer to figure 6.2

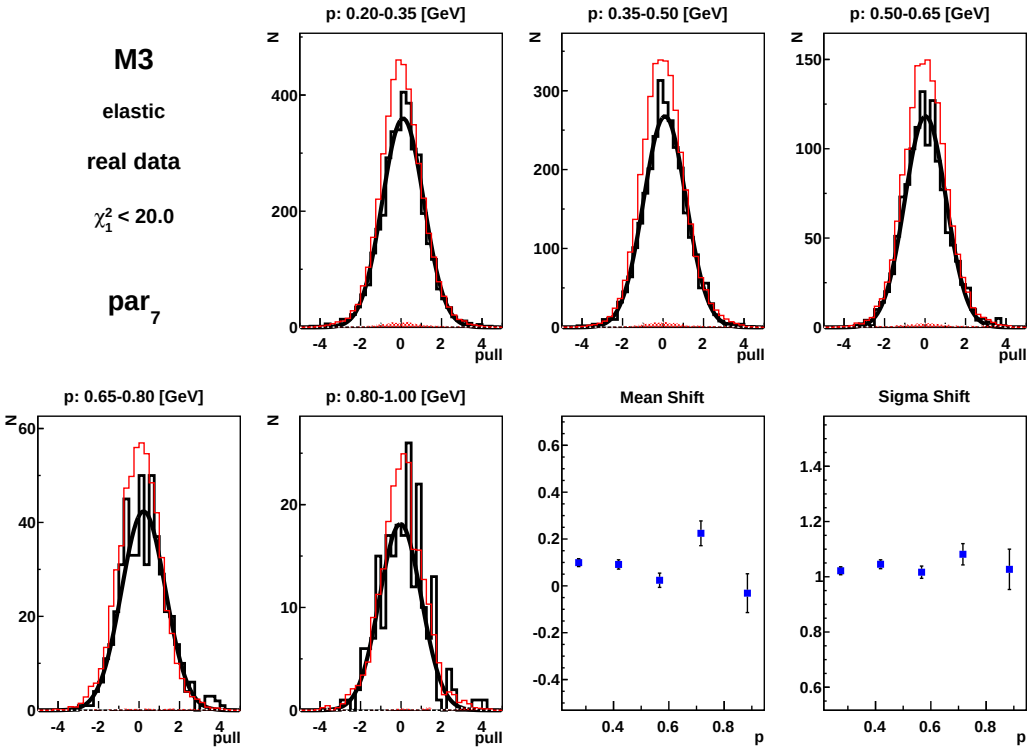

Figure A.4.: Illustration of the optimization of kinematic fitting for par_7. For further description please refer to figure 6.2

$ep \to e\gamma p\pi^0$		associated	ass (wrong)	elastic	SIDIS
overall		42.7 ± 0.8	11.4 ± 0.3	37.5 ± 0.8	8.4 ± 1.3
t_c	0.00- 0.17	39.1 ± 1.6	14.1 ± 0.8	40.5 ± 1.7	6.3 ± 2.4
	0.17- 0.30	38.7 ± 1.5	9.5 ± 0.6	42.7 ± 1.7	9.2 ± 2.7
	0.30- 0.50	43.6 ± 1.7	11.8 ± 0.7	35.9 ± 1.4	8.7 ± 2.5
	0.50- 1.50	50.6 ± 1.9	10.8 ± 0.7	29.7 ± 1.3	8.9 ± 2.3
x_B	0.03- 0.07	43.9 ± 1.3	12.6 ± 0.6	37.1 ± 1.2	6.4 ± 1.7
	0.07- 0.10	43.6 ± 1.7	10.9 ± 0.6	35.9 ± 1.5	9.6 ± 2.8
	0.10- 0.15	41.4 ± 1.8	11.3 ± 0.7	37.1 ± 1.6	10.1 ± 2.9
	0.15- 0.35	39.2 ± 2.2	8.6 ± 0.8	44.0 ± 2.4	8.1 ± 2.8
Q^2	1.00- 1.50	42.7 ± 1.6	12.0 ± 0.7	40.3 ± 1.5	5.0 ± 2.2
	1.50- 2.30	40.7 ± 1.6	11.4 ± 0.6	34.3 ± 1.4	13.5 ± 3.0
	2.30- 3.50	47.8 ± 1.6	10.5 ± 0.6	35.7 ± 1.3	6.0 ± 1.7
	3.50-10.0	39.2 ± 1.8	11.8 ± 0.8	42.3 ± 1.8	6.7 ± 1.9

Table A.1.: Extended fractional contributions for the $ep \to e\gamma p\pi^0$ selection. Fractions due to the wrong channel are included as well.

$ep \to e\gamma n\pi^+$		associated	ass (wrong)	elastic	SIDIS
overall		44.5 ± 0.9	6.6 ± 0.2	37.3 ± 0.8	11.5 ± 1.3
t_c	0.00- 0.17	47.8 ± 1.8	6.2 ± 0.4	37.5 ± 1.5	8.5 ± 2.6
	0.17- 0.30	41.6 ± 1.5	6.0 ± 0.4	42.4 ± 1.6	10.0 ± 2.4
	0.30- 0.50	45.0 ± 1.8	6.2 ± 0.5	36.3 ± 1.5	12.5 ± 2.7
	0.50- 1.50	43.7 ± 1.9	8.4 ± 0.6	31.5 ± 1.5	16.3 ± 3.0
x_B	0.03- 0.07	45.5 ± 1.4	8.3 ± 0.4	41.1 ± 1.3	5.1 ± 1.7
	0.07- 0.10	43.5 ± 1.8	6.7 ± 0.5	37.3 ± 1.6	12.5 ± 3.0
	0.10- 0.15	45.0 ± 1.9	5.2 ± 0.4	36.5 ± 1.6	13.3 ± 3.0
	0.15- 0.35	43.5 ± 2.1	4.8 ± 0.5	30.1 ± 1.6	21.6 ± 3.2
Q^2	1.00- 1.50	44.3 ± 1.8	8.8 ± 0.6	40.2 ± 1.7	6.7 ± 2.9
	1.50- 2.30	43.2 ± 1.7	6.9 ± 0.5	36.7 ± 1.5	13.2 ± 2.9
	2.30- 3.50	45.4 ± 1.7	5.4 ± 0.4	37.8 ± 1.5	11.4 ± 2.4
	3.50-10.0	45.6 ± 1.7	5.4 ± 0.4	34.6 ± 1.3	14.4 ± 2.0

Table A.2.: Extended fractional contributions for the traditional $ep \to e\gamma n\pi^+$ selection. Fractions due to the wrong channel are included as well.

$e^+p \to e^+\gamma\Delta^+$ (method 7)				
raw		$A_{LU}^{\cos(0\phi)}$	$A_{LU}^{\sin(\phi)}$	$A_{LU}^{\sin(2\phi)}$
overall		0.055 ± 0.049	-0.068 ± 0.069	-0.047 ± 0.070
t_c	0.00-0.17	0.140 ± 0.094	-0.013 ± 0.135	-0.132 ± 0.133
	0.17-0.30	-0.056 ± 0.097	-0.101 ± 0.134	0.101 ± 0.138
	0.30-0.50	0.099 ± 0.101	0.098 ± 0.142	0.062 ± 0.140
	0.50-1.50	0.001 ± 0.102	-0.223 ± 0.141	-0.224 ± 0.150
x_B	0.00-0.07	0.165 ± 0.085	-0.006 ± 0.119	-0.171 ± 0.123
	0.07-0.10	-0.024 ± 0.094	-0.115 ± 0.131	0.096 ± 0.136
	0.10-0.15	0.026 ± 0.098	-0.223 ± 0.145	0.171 ± 0.145
	0.15-0.35	-0.032 ± 0.130	0.056 ± 0.220	-0.317 ± 0.203
Q^2	1.00-1.50	0.257 ± 0.103	0.015 ± 0.141	-0.050 ± 0.146
	1.50-2.30	-0.054 ± 0.090	-0.094 ± 0.126	-0.126 ± 0.127
	2.30-3.50	0.055 ± 0.097	-0.043 ± 0.138	0.041 ± 0.139
	3.50-10.0	-0.035 ± 0.105	-0.142 ± 0.156	-0.024 ± 0.156
corrected		$A_{LU}^{\cos(0\phi)}$	$A_{LU}^{\sin(\phi)}$	$A_{LU}^{\sin(2\phi)}$
overall		0.066 ± 0.065	-0.079 ± 0.092	-0.049 ± 0.093
t_c	0.00-0.17	0.206 ± 0.125	-0.006 ± 0.179	-0.137 ± 0.177
	0.17-0.30	-0.079 ± 0.133	-0.065 ± 0.184	0.208 ± 0.190
	0.30-0.50	0.094 ± 0.132	0.115 ± 0.185	0.053 ± 0.184
	0.50-1.50	0.002 ± 0.134	-0.298 ± 0.186	-0.290 ± 0.197
x_B	0.00-0.07	0.199 ± 0.104	0.010 ± 0.146	-0.195 ± 0.151
	0.07-0.10	-0.036 ± 0.126	-0.128 ± 0.174	0.140 ± 0.181
	0.10-0.15	0.032 ± 0.135	-0.286 ± 0.200	0.248 ± 0.200
	0.15-0.35	-0.081 ± 0.200	0.063 ± 0.338	-0.477 ± 0.313
Q^2	1.00-1.50	0.316 ± 0.131	0.034 ± 0.179	-0.027 ± 0.185
	1.50-2.30	-0.083 ± 0.123	-0.119 ± 0.174	-0.166 ± 0.176
	2.30-3.50	0.083 ± 0.128	-0.042 ± 0.182	0.072 ± 0.185
	3.50-10.0	-0.071 ± 0.144	-0.173 ± 0.213	-0.038 ± 0.213

Table A.3.: Beam spin asymmetry amplitudes for associated DVCS/BH ($e^+p \to e^+\gamma p\Delta^+$) selected with method 7.

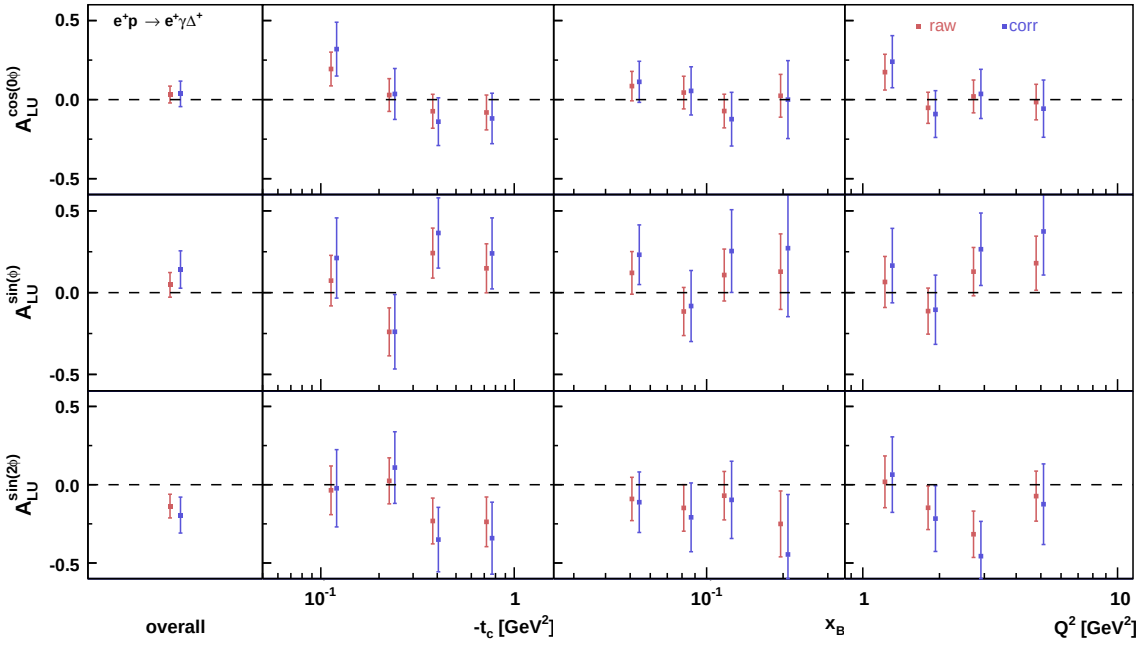

Figure A.5.: Beam spin asymmetrie amplitudes for associated DVCS/BH ($e^+p \to e^+\gamma\Delta^+$).

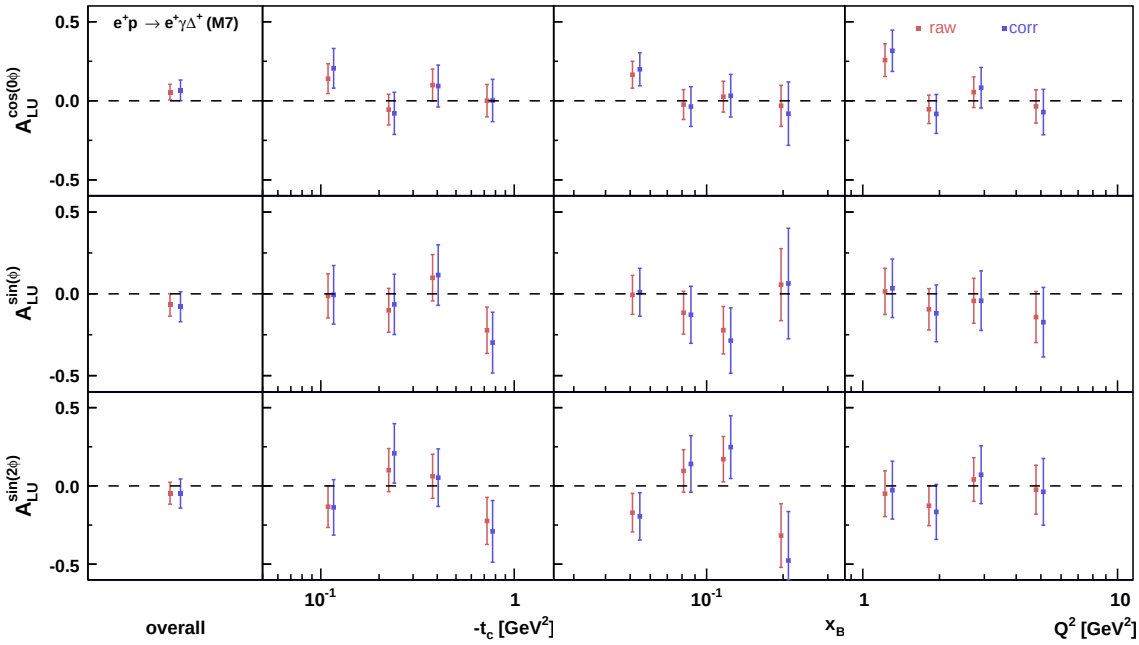

Figure A.6.: Beam spin asymmetry amplitudes for associated DVCS/BH ($e^+p \to e^+\gamma\Delta^+$) selected with method 7.

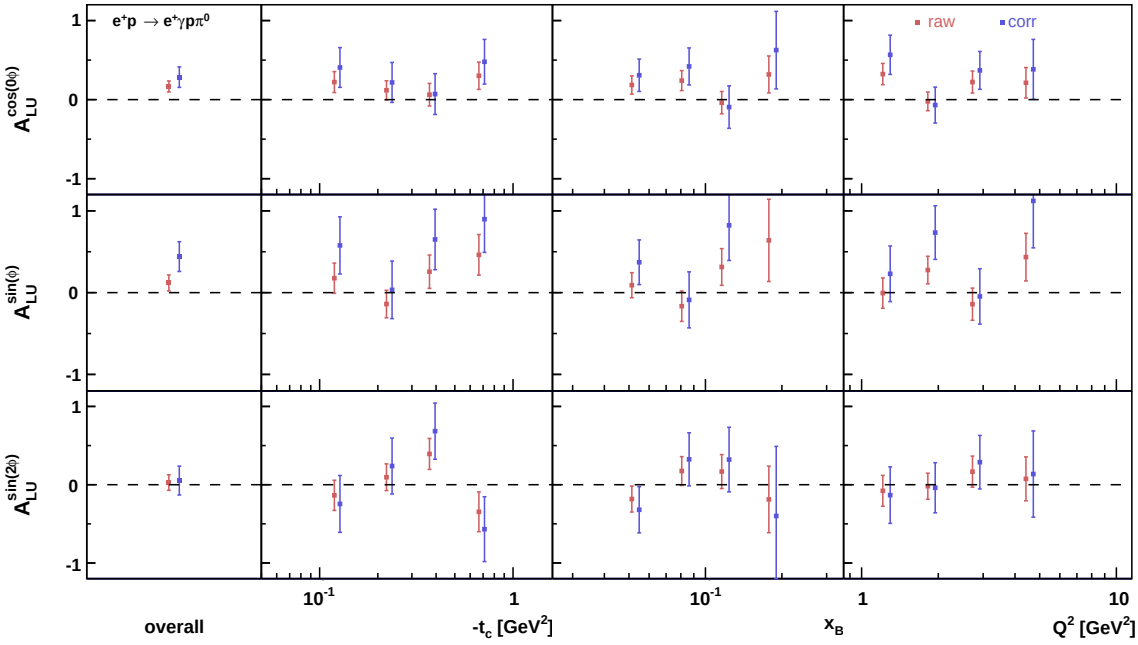

Figure A.7.: Beam spin asymmetry amplitudes for associated DVCS/BH ($e^+p \to e^+\gamma p\pi^0$).

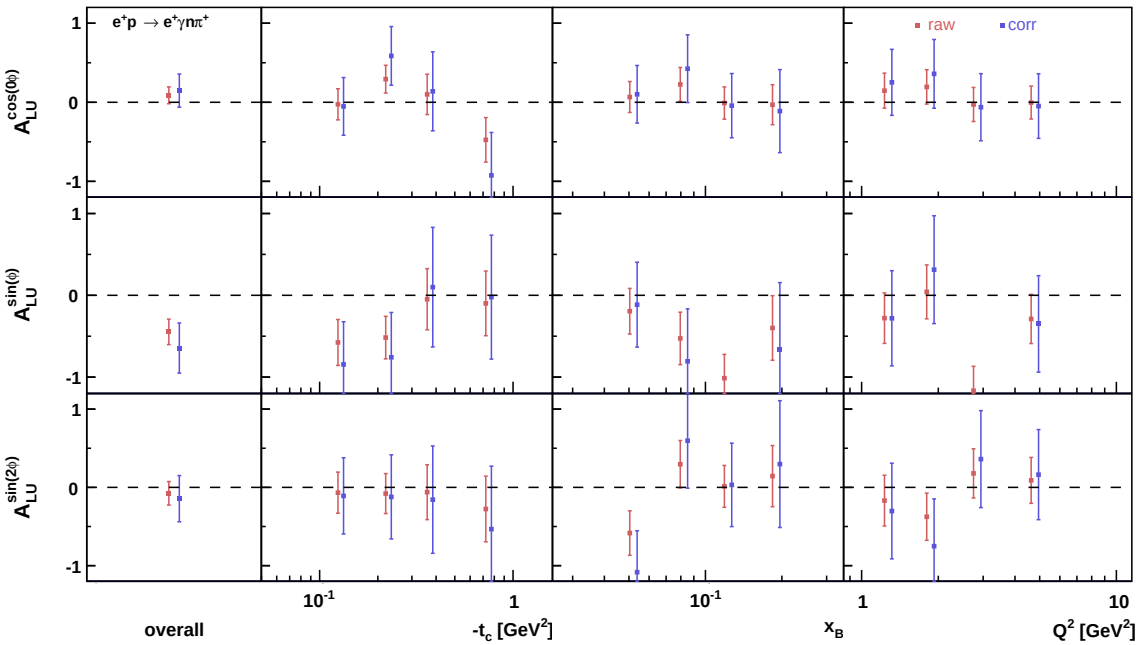

Figure A.8.: Beam spin asymmetrie amplitudes for associated DVCS/BH ($e^+p \to e^+\gamma n\pi^+$).

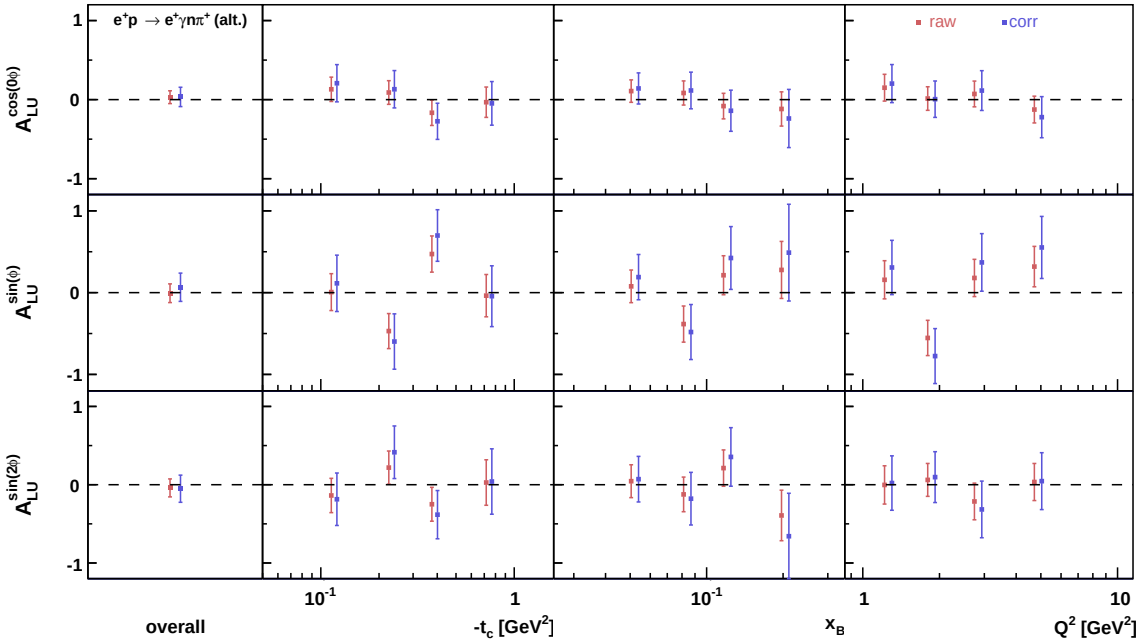

Figure A.9.: Beam spin asymmetry amplitudes for associated DVCS/BH ($e^+p \to e^+\gamma n\pi^+$) selected with the alternative approach.

$e^+p \to e^+\gamma p$											
		$A_{LU}^{\cos(0\phi)}$			$A_{LU}^{\sin(\phi)}$			$A_{LU}^{\sin(2\phi)}$			
overall		0.036	±	0.025	-0.324	±	0.035	0.036	±	0.036	
t_c	0.00-0.17	0.012	±	0.103	-0.048	±	0.204	-0.085	±	0.179	
	0.17-0.30	0.037	±	0.039	-0.282	±	0.056	0.083	±	0.056	
	0.30-0.50	0.016	±	0.040	-0.415	±	0.055	-0.028	±	0.056	
	0.50-1.50	0.094	±	0.068	-0.266	±	0.095	0.064	±	0.098	
x_B	0.00-0.07	0.069	±	0.048	-0.302	±	0.066	0.068	±	0.068	
	0.07-0.10	-0.005	±	0.048	-0.312	±	0.068	0.089	±	0.068	
	0.10-0.15	0.063	±	0.048	-0.331	±	0.071	-0.035	±	0.071	
	0.15-0.35	-0.007	±	0.059	-0.319	±	0.096	0.006	±	0.094	
Q^2	1.00-1.50	0.107	±	0.056	-0.301	±	0.077	0.087	±	0.077	
	1.50-2.30	0.029	±	0.047	-0.267	±	0.067	0.034	±	0.067	
	2.30-3.50	0.007	±	0.049	-0.429	±	0.068	0.064	±	0.070	
	3.50-10.0	0.004	±	0.050	-0.279	±	0.073	-0.045	±	0.073	

Table A.4.: Beam spin asymmetry amplitudes for elastic DVCS/BH ($e^+p \to e^+\gamma p$).

$e^+p \to e^+\gamma\Delta^+$											
		$A_{LU}^{\cos(0\phi)}$			$A_{LU}^{\sin(\phi)}$			$A_{LU}^{\sin(2\phi)}$			
overall		0.032	±	0.053	0.048	±	0.075	-0.137	±	0.076	
t_c	0.00-0.17	0.194	±	0.107	0.073	±	0.154	-0.036	±	0.156	
	0.17-0.30	0.029	±	0.104	-0.240	±	0.147	0.025	±	0.147	
	0.30-0.50	-0.074	±	0.107	0.242	±	0.153	-0.232	±	0.146	
	0.50-1.50	-0.081	±	0.110	0.149	±	0.150	-0.237	±	0.159	
x_B	0.00-0.07	0.086	±	0.093	0.121	±	0.130	-0.091	±	0.138	
	0.07-0.10	0.045	±	0.103	-0.115	±	0.147	-0.148	±	0.149	
	0.10-0.15	-0.072	±	0.106	0.108	±	0.159	-0.070	±	0.155	
	0.15-0.35	0.024	±	0.135	0.128	±	0.231	-0.250	±	0.210	
Q^2	1.00-1.50	0.174	±	0.113	0.065	±	0.156	0.018	±	0.165	
	1.50-2.30	-0.052	±	0.098	-0.113	±	0.141	-0.147	±	0.139	
	2.30-3.50	0.020	±	0.104	0.128	±	0.148	-0.317	±	0.148	
	3.50-10.0	-0.015	±	0.112	0.180	±	0.165	-0.073	±	0.160	
corrected		$A_{LU}^{\cos(0\phi)}$			$A_{LU}^{\sin(\phi)}$			$A_{LU}^{\sin(2\phi)}$			
overall		0.036	±	0.081	0.141	±	0.114	-0.194	±	0.115	
t_c	0.00-0.17	0.319	±	0.170	0.212	±	0.245	-0.023	±	0.247	
	0.17-0.30	0.036	±	0.161	-0.239	±	0.228	0.110	±	0.229	
	0.30-0.50	-0.139	±	0.151	0.365	±	0.215	-0.351	±	0.206	
	0.50-1.50	-0.119	±	0.160	0.240	±	0.217	-0.342	±	0.230	
x_B	0.00-0.07	0.113	±	0.130	0.232	±	0.182	-0.112	±	0.193	
	0.07-0.10	0.055	±	0.152	-0.082	±	0.217	-0.208	±	0.220	
	0.10-0.15	-0.124	±	0.170	0.254	±	0.253	-0.097	±	0.247	
	0.15-0.35	0.000	±	0.246	0.272	±	0.419	-0.446	±	0.383	
Q^2	1.00-1.50	0.240	±	0.165	0.165	±	0.228	0.064	±	0.241	
	1.50-2.30	-0.091	±	0.148	-0.104	±	0.212	-0.216	±	0.210	
	2.30-3.50	0.036	±	0.156	0.265	±	0.221	-0.458	±	0.222	
	3.50-10.0	-0.057	±	0.181	0.374	±	0.266	-0.125	±	0.257	

Table A.5.: Beam spin asymmetry amplitudes for associated DVCS/BH ($e^+p \to e^+\gamma\Delta^+$).

$e^+p \to e^+\gamma p\pi^0$											
raw		$A_{LU}^{\cos(0\phi)}$			$A_{LU}^{\sin(\phi)}$			$A_{LU}^{\sin(2\phi)}$			
overall		0.166	±	0.070	0.119	±	0.098	0.028	±	0.099	
t_c	0.00-0.17	0.222	±	0.133	0.177	±	0.184	-0.136	±	0.193	
	0.17-0.30	0.118	±	0.121	-0.139	±	0.169	0.096	±	0.171	
	0.30-0.50	0.062	±	0.143	0.256	±	0.204	0.393	±	0.198	
	0.50-1.50	0.302	±	0.173	0.462	±	0.248	-0.346	±	0.254	
x_B	0.00-0.07	0.185	±	0.115	0.091	±	0.153	-0.183	±	0.166	
	0.07-0.10	0.241	±	0.127	-0.166	±	0.186	0.175	±	0.184	
	0.10-0.15	-0.039	±	0.141	0.313	±	0.224	0.168	±	0.217	
	0.15-0.35	0.318	±	0.234	0.639	±	0.503	-0.188	±	0.425	
Q^2	1.00-1.50	0.323	±	0.135	-0.005	±	0.185	-0.078	±	0.197	
	1.50-2.30	-0.022	±	0.118	0.276	±	0.168	-0.019	±	0.166	
	2.30-3.50	0.222	±	0.139	-0.141	±	0.197	0.167	±	0.199	
	3.50-10.0	0.213	±	0.193	0.434	±	0.291	0.075	±	0.281	
corrected		$A_{LU}^{\cos(0\phi)}$			$A_{LU}^{\sin(\phi)}$			$A_{LU}^{\sin(2\phi)}$			
overall		0.284	±	0.130	0.441	±	0.182	0.053	±	0.184	
t_c	0.00-0.17	0.406	±	0.251	0.577	±	0.350	-0.245	±	0.363	
	0.17-0.30	0.217	±	0.253	0.034	±	0.352	0.239	±	0.357	
	0.30-0.50	0.070	±	0.258	0.650	±	0.370	0.684	±	0.359	
	0.50-1.50	0.479	±	0.282	0.898	±	0.406	-0.568	±	0.414	
x_B	0.00-0.07	0.308	±	0.204	0.372	±	0.273	-0.320	±	0.295	
	0.07-0.10	0.420	±	0.234	-0.088	±	0.343	0.324	±	0.339	
	0.10-0.15	-0.095	±	0.269	0.823	±	0.430	0.321	±	0.413	
	0.15-0.35	0.626	±	0.490	1.621	±	1.059	-0.399	±	0.889	
Q^2	1.00-1.50	0.567	±	0.248	0.230	±	0.340	-0.133	±	0.361	
	1.50-2.30	-0.069	±	0.227	0.734	±	0.328	-0.039	±	0.320	
	2.30-3.50	0.370	±	0.239	-0.046	±	0.338	0.288	±	0.342	
	3.50-10.0	0.383	±	0.379	1.122	±	0.574	0.136	±	0.551	

Table A.6.: Beam spin asymmetry amplitudes for associated DVCS/BH ($e^+p \to e^+\gamma p\pi^0$).

$e^+p \to e^+\gamma n\pi^+$											
raw		$A_{LU}^{\cos(0\phi)}$			$A_{LU}^{\sin(\phi)}$			$A_{LU}^{\sin(2\phi)}$			
overall		0.088	$\pm$	0.107	-0.447	$\pm$	0.156	-0.076	$\pm$	0.150	
t_c	0.00-0.17	-0.026	$\pm$	0.197	-0.576	$\pm$	0.280	-0.067	$\pm$	0.262	
	0.17-0.30	0.292	$\pm$	0.175	-0.517	$\pm$	0.260	-0.079	$\pm$	0.255	
	0.30-0.50	0.100	$\pm$	0.256	-0.048	$\pm$	0.374	-0.061	$\pm$	0.351	
	0.50-1.50	-0.475	$\pm$	0.281	-0.099	$\pm$	0.395	-0.276	$\pm$	0.419	
x_B	0.00-0.07	0.067	$\pm$	0.196	-0.195	$\pm$	0.279	-0.584	$\pm$	0.284	
	0.07-0.10	0.226	$\pm$	0.214	-0.527	$\pm$	0.321	0.296	$\pm$	0.303	
	0.10-0.15	-0.010	$\pm$	0.204	-1.014	$\pm$	0.291	0.013	$\pm$	0.267	
	0.15-0.35	-0.030	$\pm$	0.253	-0.399	$\pm$	0.395	0.144	$\pm$	0.390	
Q^2	1.00-1.50	0.147	$\pm$	0.221	-0.280	$\pm$	0.308	-0.169	$\pm$	0.324	
	1.50-2.30	0.195	$\pm$	0.217	0.042	$\pm$	0.330	-0.375	$\pm$	0.301	
	2.30-3.50	-0.028	$\pm$	0.215	-1.166	$\pm$	0.298	0.178	$\pm$	0.314	
	3.50-10.0	-0.003	$\pm$	0.208	-0.289	$\pm$	0.300	0.089	$\pm$	0.293	
corrected		$A_{LU}^{\cos(0\phi)}$			$A_{LU}^{\sin(\phi)}$			$A_{LU}^{\sin(2\phi)}$			
overall		0.148	$\pm$	0.209	-0.645	$\pm$	0.306	-0.144	$\pm$	0.295	
t_c	0.00-0.17	-0.052	$\pm$	0.365	-0.846	$\pm$	0.522	-0.109	$\pm$	0.487	
	0.17-0.30	0.587	$\pm$	0.371	-0.758	$\pm$	0.548	-0.121	$\pm$	0.537	
	0.30-0.50	0.138	$\pm$	0.500	0.099	$\pm$	0.731	-0.157	$\pm$	0.686	
	0.50-1.50	-0.924	$\pm$	0.542	-0.023	$\pm$	0.758	-0.534	$\pm$	0.805	
x_B	0.00-0.07	0.101	$\pm$	0.364	-0.115	$\pm$	0.519	-1.084	$\pm$	0.530	
	0.07-0.10	0.425	$\pm$	0.428	-0.807	$\pm$	0.642	0.596	$\pm$	0.606	
	0.10-0.15	-0.043	$\pm$	0.406	-1.784	$\pm$	0.592	0.032	$\pm$	0.533	
	0.15-0.35	-0.112	$\pm$	0.525	-0.665	$\pm$	0.820	0.297	$\pm$	0.810	
Q^2	1.00-1.50	0.252	$\pm$	0.417	-0.281	$\pm$	0.582	-0.302	$\pm$	0.611	
	1.50-2.30	0.360	$\pm$	0.435	0.313	$\pm$	0.659	-0.752	$\pm$	0.604	
	2.30-3.50	-0.063	$\pm$	0.424	-2.063	$\pm$	0.598	0.361	$\pm$	0.619	
	3.50-10.0	-0.048	$\pm$	0.408	-0.350	$\pm$	0.590	0.163	$\pm$	0.576	

Table A.7.: Beam spin asymmetry amplitudes for associated DVCS/BH ($e^+p \to e^+\gamma n\pi^+$) extracted from the traditional selection sample.

$e^+p \to e^+\gamma n\pi^+$ (alternative)											
raw		$A_{LU}^{\cos(0\phi)}$			$A_{LU}^{\sin(\phi)}$			$A_{LU}^{\sin(2\phi)}$			
overall		0.031	±	0.081	-0.007	±	0.114	-0.041	±	0.115	
t_c	0.00-0.17	0.131	±	0.154	0.006	±	0.225	-0.138	±	0.219	
	0.17-0.30	0.090	±	0.150	-0.470	±	0.214	0.219	±	0.212	
	0.30-0.50	-0.166	±	0.161	0.472	±	0.221	-0.250	±	0.216	
	0.50-1.50	-0.033	±	0.192	-0.037	±	0.259	0.028	±	0.291	
x_B	0.00-0.07	0.108	±	0.142	0.077	±	0.199	0.045	±	0.210	
	0.07-0.10	0.084	±	0.153	-0.384	±	0.221	-0.124	±	0.221	
	0.10-0.15	-0.082	±	0.162	0.213	±	0.238	0.212	±	0.232	
	0.15-0.35	-0.118	±	0.216	0.278	±	0.349	-0.393	±	0.323	
Q^2	1.00-1.50	0.151	±	0.169	0.157	±	0.233	-0.003	±	0.245	
	1.50-2.30	0.014	±	0.149	-0.554	±	0.216	0.061	±	0.210	
	2.30-3.50	0.072	±	0.163	0.180	±	0.228	-0.214	±	0.234	
	3.50-10.0	-0.126	±	0.169	0.319	±	0.247	0.034	±	0.237	
corrected		$A_{LU}^{\cos(0\phi)}$			$A_{LU}^{\sin(\phi)}$			$A_{LU}^{\sin(2\phi)}$			
overall		0.034	±	0.122	0.066	±	0.173	-0.051	±	0.174	
t_c	0.00-0.17	0.207	±	0.236	0.114	±	0.345	-0.186	±	0.335	
	0.17-0.30	0.131	±	0.236	-0.598	±	0.338	0.415	±	0.336	
	0.30-0.50	-0.274	±	0.229	0.698	±	0.315	-0.383	±	0.308	
	0.50-1.50	-0.047	±	0.276	-0.044	±	0.372	0.041	±	0.418	
x_B	0.00-0.07	0.141	±	0.197	0.190	±	0.277	0.071	±	0.291	
	0.07-0.10	0.116	±	0.232	-0.482	±	0.336	-0.178	±	0.336	
	0.10-0.15	-0.141	±	0.260	0.424	±	0.384	0.355	±	0.374	
	0.15-0.35	-0.239	±	0.368	0.489	±	0.591	-0.658	±	0.549	
Q^2	1.00-1.50	0.203	±	0.241	0.308	±	0.332	0.021	±	0.348	
	1.50-2.30	0.005	±	0.230	-0.776	±	0.336	0.097	±	0.325	
	2.30-3.50	0.114	±	0.252	0.370	±	0.352	-0.316	±	0.362	
	3.50-10.0	-0.222	±	0.260	0.553	±	0.379	0.046	±	0.363	

Table A.8.: Beam spin asymmetry amplitudes for associated DVCS/BH ($e^+p \to e^+\gamma n\pi^+$) extracted from the alternative selection sample.

$ep \to e\gamma\Delta^+$															
raw		$A_C^{\cos(0\phi)}$			$A_C^{\cos(\phi)}$			$A_C^{\cos(2\phi)}$			$A_C^{\cos(3\phi)}$		
overall		-0.088	±	0.019	0.033	±	0.027	0.032	±	0.026	0.073	±	0.026
t_c	0.00-0.17	0.096	±	0.044	-0.004	±	0.059	-0.012	±	0.059	0.180	±	0.063
	0.17-0.30	-0.003	±	0.040	-0.041	±	0.052	-0.164	±	0.056	0.079	±	0.054
	0.30-0.50	-0.101	±	0.039	-0.072	±	0.060	0.141	±	0.057	-0.114	±	0.053
	0.50-1.50	-0.252	±	0.033	0.108	±	0.047	0.036	±	0.044	0.128	±	0.046
x_B	0.00-0.07	-0.013	±	0.040	-0.042	±	0.064	0.206	±	0.054	0.120	±	0.049
	0.07-0.10	-0.235	±	0.031	0.213	±	0.043	0.021	±	0.042	0.136	±	0.044
	0.10-0.15	0.050	±	0.047	0.034	±	0.065	-0.185	±	0.069	-0.034	±	0.065
	0.15-0.35	-0.053	±	0.060	-0.108	±	0.082	-0.029	±	0.081	0.037	±	0.076
Q^2	1.00-1.50	-0.042	±	0.041	-0.161	±	0.064	0.172	±	0.056	0.041	±	0.056
	1.50-2.30	-0.078	±	0.035	0.051	±	0.049	0.059	±	0.048	0.205	±	0.049
	2.30-3.50	-0.181	±	0.033	0.153	±	0.044	-0.120	±	0.046	-0.100	±	0.046
	3.50-10.0	0.014	±	0.047	-0.063	±	0.067	-0.004	±	0.067	0.103	±	0.065
corrected		$A_C^{\cos(0\phi)}$			$A_C^{\cos(\phi)}$			$A_C^{\cos(2\phi)}$			$A_C^{\cos(3\phi)}$		
overall		-0.118	±	0.028	0.026	±	0.041	0.044	±	0.040	0.111	±	0.040
t_c	0.00-0.17	0.169	±	0.069	-0.037	±	0.093	-0.023	±	0.093	0.285	±	0.100
	0.17-0.30	0.009	±	0.062	-0.086	±	0.081	-0.256	±	0.086	0.123	±	0.084
	0.30-0.50	-0.131	±	0.054	-0.117	±	0.084	0.195	±	0.079	-0.159	±	0.075
	0.50-1.50	-0.354	±	0.049	0.140	±	0.069	0.049	±	0.064	0.184	±	0.066
x_B	0.00-0.07	-0.006	±	0.055	-0.079	±	0.089	0.284	±	0.075	0.168	±	0.069
	0.07-0.10	-0.330	±	0.047	0.288	±	0.064	0.027	±	0.062	0.200	±	0.065
	0.10-0.15	0.094	±	0.074	0.029	±	0.103	-0.296	±	0.110	-0.053	±	0.103
	0.15-0.35	-0.080	±	0.108	-0.220	±	0.147	-0.055	±	0.147	0.067	±	0.136
Q^2	1.00-1.50	-0.048	±	0.060	-0.255	±	0.093	0.245	±	0.082	0.060	±	0.082
	1.50-2.30	-0.103	±	0.053	0.054	±	0.074	0.085	±	0.072	0.307	±	0.074
	2.30-3.50	-0.255	±	0.050	0.204	±	0.065	-0.182	±	0.069	-0.148	±	0.069
	3.50-10.0	0.038	±	0.076	-0.127	±	0.108	-0.011	±	0.107	0.166	±	0.104

Table A.9.: Beam charge asymmetrie amplitudes for associated DVCS/BH ($ep \to e\gamma\Delta^+$).

$ep \to e\gamma p\pi^0$															
raw		$A_C^{\cos(0\phi)}$			$A_C^{\cos(\phi)}$			$A_C^{\cos(2\phi)}$			$A_C^{\cos(3\phi)}$		
overall		0.008	±	0.026	0.037	±	0.039	0.144	±	0.037	0.044	±	0.036
t_c	0.00-0.17	0.134	±	0.058	0.004	±	0.087	0.136	±	0.080	-0.197	±	0.081
	0.17-0.30	-0.018	±	0.044	0.131	±	0.065	0.111	±	0.067	0.160	±	0.062
	0.30-0.50	0.046	±	0.053	-0.386	±	0.082	0.326	±	0.073	-0.158	±	0.070
	0.50-1.50	-0.039	±	0.061	0.093	±	0.086	0.077	±	0.083	0.179	±	0.083
x_B	0.00-0.07	0.153	±	0.058	0.240	±	0.094	0.268	±	0.080	0.263	±	0.069
	0.07-0.10	0.020	±	0.049	0.103	±	0.079	0.337	±	0.066	0.032	±	0.066
	0.10-0.15	-0.073	±	0.064	-0.032	±	0.098	-0.069	±	0.095	-0.111	±	0.080
	0.15-0.35	0.550	±	0.329	-0.905	±	0.565	0.946	±	0.398	-0.603	±	0.230
Q^2	1.00-1.50	-0.004	±	0.050	0.026	±	0.080	0.302	±	0.068	0.147	±	0.066
	1.50-2.30	0.023	±	0.046	0.083	±	0.064	0.062	±	0.063	0.225	±	0.064
	2.30-3.50	0.065	±	0.056	-0.174	±	0.084	0.138	±	0.077	-0.352	±	0.072
	3.50-10.0	0.051	±	0.079	0.156	±	0.115	0.064	±	0.115	0.022	±	0.111
corrected		$A_C^{\cos(0\phi)}$			$A_C^{\cos(\phi)}$			$A_C^{\cos(2\phi)}$			$A_C^{\cos(3\phi)}$		
overall		0.053	±	0.049	0.004	±	0.073	0.258	±	0.068	0.085	±	0.068
t_c	0.00-0.17	0.294	±	0.110	-0.062	±	0.164	0.247	±	0.152	-0.367	±	0.153
	0.17-0.30	0.011	±	0.093	0.191	±	0.137	0.220	±	0.129	0.335	±	0.131
	0.30-0.50	0.119	±	0.096	-0.756	±	0.153	0.581	±	0.135	-0.283	±	0.128
	0.50-1.50	-0.036	±	0.099	0.106	±	0.141	0.119	±	0.135	0.294	±	0.136
x_B	0.00-0.07	0.307	±	0.103	0.364	±	0.168	0.466	±	0.142	0.468	±	0.123
	0.07-0.10	0.073	±	0.090	0.128	±	0.145	0.609	±	0.126	0.061	±	0.122
	0.10-0.15	-0.100	±	0.121	-0.125	±	0.187	-0.140	±	0.180	-0.208	±	0.152
	0.15-0.35	1.199	±	0.694	-1.975	±	1.189	1.963	±	0.845	-1.255	±	0.490
Q^2	1.00-1.50	0.033	±	0.092	-0.021	±	0.147	0.543	±	0.127	0.271	±	0.123
	1.50-2.30	0.081	±	0.088	0.098	±	0.122	0.110	±	0.121	0.433	±	0.127
	2.30-3.50	0.145	±	0.096	-0.355	±	0.144	0.228	±	0.132	-0.602	±	0.126
	3.50-10.0	0.146	±	0.156	0.229	±	0.226	0.114	±	0.227	0.047	±	0.218

Table A.10.: Beam charge asymmetrie amplitudes for associated DVCS/BH ($ep \to e\gamma p\pi^0$).

$ep \to e\gamma n\pi^+$ (alternative)															
raw		$A_C^{\cos(0\phi)}$			$A_C^{\cos(\phi)}$			$A_C^{\cos(2\phi)}$			$A_C^{\cos(3\phi)}$		
overall		0.004	±	0.031	0.066	±	0.044	0.013	±	0.044	-0.007	±	0.044
t_c	0.00-0.17	0.073	±	0.064	0.040	±	0.084	-0.041	±	0.089	0.054	±	0.090
	0.17-0.30	0.090	±	0.064	-0.004	±	0.081	-0.201	±	0.089	-0.015	±	0.086
	0.30-0.50	0.003	±	0.064	0.145	±	0.093	0.007	±	0.093	-0.309	±	0.087
	0.50-1.50	-0.144	±	0.066	-0.127	±	0.095	-0.004	±	0.085	0.158	±	0.090
x_B	0.00-0.07	0.081	±	0.067	0.027	±	0.112	0.324	±	0.090	0.068	±	0.081
	0.07-0.10	-0.159	±	0.050	0.190	±	0.065	-0.119	±	0.070	0.124	±	0.073
	0.10-0.15	0.171	±	0.074	0.078	±	0.101	-0.359	±	0.109	-0.176	±	0.104
	0.15-0.35	0.065	±	0.096	-0.068	±	0.136	0.031	±	0.135	-0.245	±	0.126
Q^2	1.00-1.50	0.004	±	0.067	0.009	±	0.104	0.193	±	0.092	-0.043	±	0.091
	1.50-2.30	-0.106	±	0.052	0.001	±	0.076	0.116	±	0.072	0.106	±	0.073
	2.30-3.50	0.206	±	0.074	0.128	±	0.077	-0.673	±	0.098	-0.235	±	0.088
	3.50-10.0	0.097	±	0.076	-0.018	±	0.117	0.175	±	0.109	-0.125	±	0.105
corrected		$A_C^{\cos(0\phi)}$			$A_C^{\cos(\phi)}$			$A_C^{\cos(2\phi)}$			$A_C^{\cos(3\phi)}$		
overall		0.020	±	0.047	0.074	±	0.067	0.016	±	0.066	-0.010	±	0.066
t_c	0.00-0.17	0.131	±	0.096	0.029	±	0.128	-0.067	±	0.136	0.083	±	0.138
	0.17-0.30	0.157	±	0.099	-0.032	±	0.128	-0.319	±	0.140	-0.023	±	0.135
	0.30-0.50	0.015	±	0.091	0.187	±	0.133	0.008	±	0.132	-0.438	±	0.125
	0.50-1.50	-0.200	±	0.095	-0.194	±	0.137	-0.008	±	0.122	0.227	±	0.130
x_B	0.00-0.07	0.127	±	0.094	0.012	±	0.155	0.444	±	0.126	0.095	±	0.113
	0.07-0.10	-0.224	±	0.077	0.259	±	0.099	-0.184	±	0.107	0.190	±	0.111
	0.10-0.15	0.288	±	0.120	0.101	±	0.161	-0.577	±	0.178	-0.280	±	0.168
	0.15-0.35	0.122	±	0.163	-0.134	±	0.230	0.050	±	0.228	-0.413	±	0.215
Q^2	1.00-1.50	0.021	±	0.094	-0.012	±	0.148	0.270	±	0.131	-0.059	±	0.129
	1.50-2.30	-0.148	±	0.080	-0.024	±	0.117	0.174	±	0.112	0.165	±	0.112
	2.30-3.50	0.335	±	0.115	0.168	±	0.119	-1.041	±	0.159	-0.361	±	0.137
	3.50-10.0	0.160	±	0.117	-0.047	±	0.179	0.265	±	0.167	-0.190	±	0.161

Table A.11.: Beam charge asymmetrie amplitudes for associated DVCS/BH ($ep \to e\gamma n\pi^+$) extracted from the alternative selection sample.

$ep \to e\gamma n\pi^+$ (traditional)															
raw		$A_C^{\cos(0\phi)}$			$A_C^{\cos(\phi)}$			$A_C^{\cos(2\phi)}$			$A_C^{\cos(3\phi)}$		
overall		0.056	±	0.042	0.266	±	0.058	0.003	±	0.059	-0.072	±	0.059
t_c	0.00-0.17	0.246	±	0.091	0.207	±	0.141	0.243	±	0.134	-0.036	±	0.129
	0.17-0.30	-0.020	±	0.066	0.217	±	0.078	-0.203	±	0.087	-0.301	±	0.088
	0.30-0.50	0.021	±	0.096	0.019	±	0.134	0.040	±	0.135	-0.102	±	0.136
	0.50-1.50	-0.011	±	0.120	0.372	±	0.167	-0.031	±	0.168	0.075	±	0.164
x_B	0.00-0.07	-0.015	±	0.096	0.471	±	0.158	0.257	±	0.129	0.090	±	0.102
	0.07-0.10	0.279	±	0.104	0.193	±	0.128	-0.083	±	0.144	0.127	±	0.141
	0.10-0.15	0.145	±	0.093	-0.088	±	0.125	-0.088	±	0.131	-0.297	±	0.121
	0.15-0.35	0.135	±	0.139	0.212	±	0.218	-0.123	±	0.200	-0.405	±	0.168
Q^2	1.00-1.50	0.097	±	0.096	0.553	±	0.145	0.045	±	0.138	0.120	±	0.124
	1.50-2.30	-0.014	±	0.077	0.185	±	0.108	0.203	±	0.112	-0.067	±	0.107
	2.30-3.50	0.405	±	0.128	-0.074	±	0.153	0.124	±	0.146	-0.916	±	0.160
	3.50-10.0	0.081	±	0.090	0.103	±	0.110	-0.332	±	0.121	0.046	±	0.119
corrected		$A_C^{\cos(0\phi)}$			$A_C^{\cos(\phi)}$			$A_C^{\cos(2\phi)}$			$A_C^{\cos(3\phi)}$		
overall		0.150	±	0.083	0.453	±	0.114	-0.003	±	0.116	-0.139	±	0.116
t_c	0.00-0.17	0.495	±	0.172	0.319	±	0.262	0.441	±	0.250	-0.065	±	0.239
	0.17-0.30	0.007	±	0.139	0.374	±	0.165	-0.437	±	0.185	-0.628	±	0.189
	0.30-0.50	0.081	±	0.188	-0.029	±	0.261	0.070	±	0.263	-0.197	±	0.265
	0.50-1.50	0.013	±	0.230	0.657	±	0.322	-0.067	±	0.321	0.146	±	0.314
x_B	0.00-0.07	0.014	±	0.178	0.804	±	0.295	0.468	±	0.240	0.170	±	0.189
	0.07-0.10	0.597	±	0.211	0.317	±	0.256	-0.175	±	0.288	0.255	±	0.282
	0.10-0.15	0.330	±	0.186	-0.242	±	0.251	-0.184	±	0.262	-0.589	±	0.244
	0.15-0.35	0.314	±	0.289	0.382	±	0.451	-0.263	±	0.414	-0.835	±	0.354
Q^2	1.00-1.50	0.224	±	0.181	0.972	±	0.280	0.076	±	0.261	0.228	±	0.234
	1.50-2.30	0.012	±	0.153	0.301	±	0.217	0.396	±	0.226	-0.131	±	0.214
	2.30-3.50	0.838	±	0.256	-0.215	±	0.301	0.235	±	0.288	-1.801	±	0.331
	3.50-10.0	0.196	±	0.176	0.138	±	0.216	-0.660	±	0.240	0.093	±	0.234

Table A.12.: Beam charge asymmetrie amplitudes for associated DVCS/BH ($ep \to e\gamma n\pi^+$) extracted from the traditional selection sample.

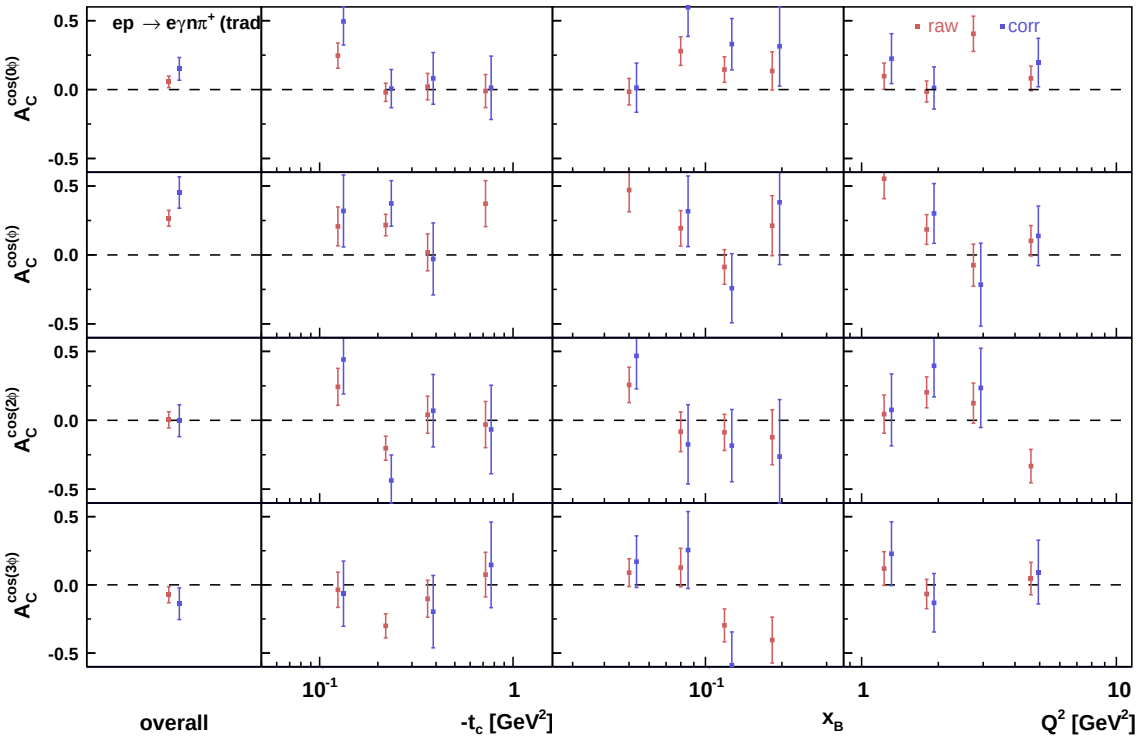

Figure A.10.: Beam charge asymmetrie amplitudes for associated DVCS/BH ($ep \to e\gamma n\pi^+$).

Acknowledgements

Last but not least I would like to thank a number of people for their support and advice during the preparation and writing of this thesis.
I shall start by thanking Michael Düren who always supported my work whether it was by granting the participations in schools and conferences or by providing me with a supportive and pleasant work environment. I really appreciate his guidance and advice for the last three years, since I started my Bachelor thesis.
Thanks to Avetik Hayrapetyan and Irina Brodski for their help, especially for introducing me to the underlying topic and answering numerous questions about the HERMES experiment.
I have to express my greatest gratitude to Sergey Yaschenko who has been sort of my electronic pen pal over the past 15 months. Without his patient supervision this thesis would not have been possible. I'm glad that we met a couple of times during my stays at DESY to have conversations beyond physics as well. I'm much obliged to all the other members of the HERMES Collaboration for their support, especially I'd like to thank Aram Movsisyan, Caroline Riedl and Eduard Avetisyan.
For their great colleagueship I'd like to thank all the members of our working group in Gießen, who gave me a great time whenever I turned my office chair around and were always very supportive. I'm also happy that I was able to share a lot of time and good memories with my friends Daniel, Julian and Marian.
Special thanks goes to my family, especially my parents Klaus and Christina and my girlfriend Anke for their continuing support throughout my university studies and that they understood if I was not able to devote them the time they deserve.
Thank you all!

Erklärung

Ich versichere, dass ich die vorliegende Arbeit selbständig geschrieben und deren Inhalte wissenschaftlich erarbeitet habe. Außer der angegebenen Literatur habe ich keine weiteren Hilfsmittel verwendet.

Gießen, den 13.Mai 2013 Erik Etzelmüller